Relationship between locked modes and disruptions in the DIII-D tokamak

Ryan Sweeney

Submitted in partial fulfillment of the
requirements for the degree of
Doctor of Philosophy
in the Graduate School of Arts and Sciences

Columbia University
2017

ABSTRACT

Relationship between locked modes and disruptions in the DIII-D tokamak

Ryan Sweeney

This thesis is organized into three body chapters: (1) the first use of naturally rotating tearing modes to diagnose intrinsic error fields is presented with experimental results from the EXTRAP T2R reversed field pinch, (2) a large scale study of locked modes (LMs) with rotating precursors in the DIII-D tokamak is reported, and (3) an in depth study of LM induced thermal collapses on a few DIII-D discharges is presented.

The amplitude of naturally rotating tearing modes (TMs) in EXTRAP T2R is modulated in the presence of a resonant field (given by the superposition of the resonant intrinsic error field, and, possibly, an applied, resonant magnetic perturbation (RMP)). By scanning the amplitude and phase of the RMP and observing the phase-dependent amplitude modulation of the resonant, naturally rotating TM, the corresponding resonant error field is diagnosed.

A rotating TM can decelerate and lock in the laboratory frame, under the effect of an electromagnetic torque due to eddy currents induced in the wall. These locked modes often lead to a disruption, where energy and particles are lost from the equilibrium configuration on a timescale of a few to tens of milliseconds in the DIII-D tokamak. In fusion reactors, disruptions pose a problem for the longevity of the reactor. Thus, learning to predict and avoid them is important. A database was developed consisting of $\sim$ 2000 DIII-D discharges exhibiting TMs that lock. The database was used to study the evolution, the nonlinear effects on equilibria, and the disruptivity of locked and quasi-stationary modes with poloidal and toroidal mode numbers $m = 2$ and $n = 1$ at DIII-D. The analysis of 22,500 discharges shows that more than 18% of disruptions present signs of locked or quasi-stationary modes with

rotating precursors. A parameter formulated by the plasma internal inductance l_i divided by the safety factor at 95% of the toroidal flux, q_{95}, is found to exhibit predictive capability over whether a locked mode will cause a disruption or not, and does so up to hundreds of milliseconds before the disruption. Within 20 ms of the disruption, the shortest distance between the island separatrix and the unperturbed last closed flux surface, referred to as d_{edge}, performs comparably to l_i/q_{95} in its ability to discriminate disruptive locked modes, and it also correlates well with the duration of the locked mode. On average, and within errors, the n=1 perturbed field grows exponentially in the final 50 ms before a disruption, however, the island width cannot discern whether a LM will disrupt or not up to 20 ms before the disruption.

A few discharges are selected to analyze the evolution of the electron temperature profile in the presence of multiple coexisting locked modes during partial and full thermal quenches. Partial thermal quenches are often an initial, distinct stage in the full thermal quench caused by radiation, conduction, or convection losses. Here we explore the fundamental mechanism that causes the partial quench. Near the onset of partial thermal quenches, locked islands are observed to align in a unique way, or island widths are observed to grow above a threshold. Energy analysis on one discharge suggests that about half of the energy is lost in the divertor region. In discharges with minimum values of the safety factor above ~ 1.2, and with current profiles expected to be classically stable, locked modes are observed to self-stabilize by inducing a full thermal quench, possibly by double tearing modes that remove the pressure gradient across the island, thus removing the neoclassical drive.

Contents

List of Figures

List of Tables

Acknowledgments

I would like to acknowledge my advisor, Francesco Volpe, for believing in me, especially during the difficult start to my PhD. He was consistently generous with his time, and his mentoring allowed me to get started on the research quickly. I have learned a lot about plasma physics from him, and together, we have made some exciting discoveries. With respect to this project, I would like to thank him for conceiving of the locked mode database, and sharing the project with me. Separately, I would like to thank him for the opportunity to travel to Bad Honnef, Germany, for the *Carolus Magnus Summer School*, and to the KTH Royal Institute of Technology in Sweden for experiments on EXTRAP T2R.

I would like to thank Ken Hammond for providing 24/7 company during the first year at Columbia, and for being part of the "traveling trio" on our European city-hop prior to the summer school.

During my trip to Stockhom, Sweden, Lorenzo, Per, and Richard welcomed me, and allowed me to monopolize the EXTRAP T2R reverse field pinch for two weeks. I thank them for their professional assistance, and their company.

Throughout my time in San Diego, I spent hours in Rob La Haye's office, seeking his wisdom on tearing modes, as well as Sci-Fi classics of the 60's and 70's. I thank Rob for his tutelage on both of these topics.

I want to recognize the faithful members of the Thursday GA Volleyball League for helping to invent an alternate form of the game, where teams are rewarded for recovering stray balls that rebound off the bushes, and where winning serves are required to be of the jumping type.

I would like to thank all the "500 level" graduate students for the entertaining lunchtime conversations, and for insisting that we deserve better than Folger's.

I want to thank Wilkie Choi for his assistance in the organization and development of the locked mode database. I also want to thank Sean Flanagan and David Miller for their computer expertise, particularly for ensuring that populating our database would not crash the DIII-D servers.

I would like to thank Ted Strait for his very thoughtful and detailed reviews of my work that led to new findings, and to better ways of approaching problems.

I want to thank my parents for encouraging and supporting me in this research, even when it meant moving to the furthest city from New Hampshire in the continental U.S. They have always trusted my career decisions, and been there to celebrate the small victories along the way. I would not have pursued this degree without them.

Last, but certainly not least, I want to thank my fiancée, Rachel, for picking up and moving to NYC with me when I started at Columbia, and then agreeing to pick up and move to San Diego just two years later so I could pursue a research opportunity at DIII-D. She has been understanding of the commitment this work has required, and has helped me through all of the ups and downs. The complete list of thank yous to her would be too long to include here, so instead...

This thesis is dedicated to my fiancée Rachel.

Chapter 1

Introduction

1.1 The promises of fusion energy

Fusion energy, like fission energy, is a result of reorganizing the nucleons (protons and neutrons) into a lower energy state, and thus, by conservation of energy, releasing energy in the process. Fusion generally produces a net positive energy when two elements combine to form an element with a number of nucleons (also known as mass number) less than or equal to that of iron. This is supported by the diagram of the binding energy per nucleon plotted as a function of the total number of nucleons. The diagram is shown in figure 1-1 and peaks at 56 (i.e. iron or isotopes of neighboring elements on the periodic table).

Releasing nuclear energy through fusion does not produce greenhouse gases, and if so-called aneutronic reactions are used (i.e. reactions that do not emit neutrons), no radioactive waste would be produced [16]. In the present approaches to fusion energy that use deuterium and tritium fuels, the vessel will become radioactive due to neutron bombardment. The most prominent approaches to fusion energy to date are not capable of a runaway scenario analogous to the fission melt-down. Another concern associated with fission reactors is the production of nuclear weapons materials, but this is not a concern for fusion reactors as they will not readily produce these materials. Finally, assuming that within tens of thousands of years (the expected supply of first generation fusion fuels [16]) the conditions necessary for deuterium-deuterium fusion

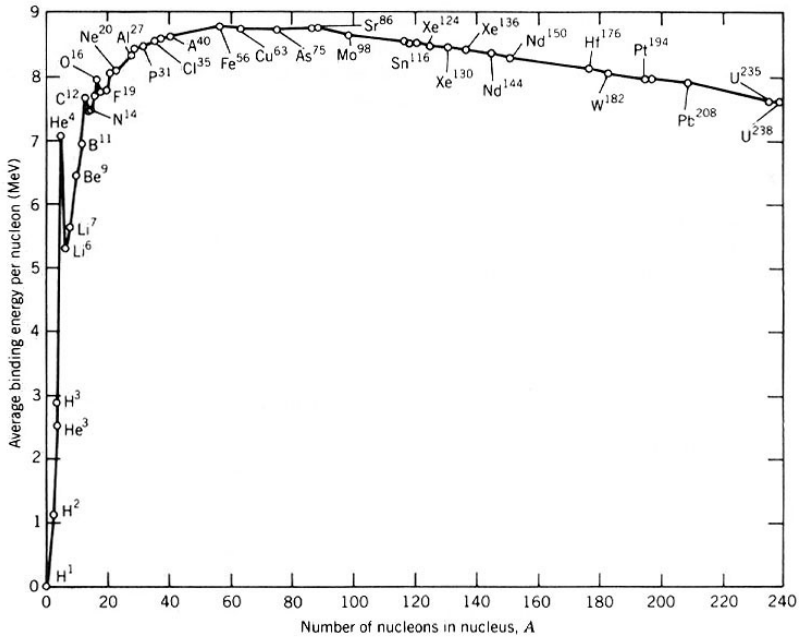

Figure 1-1: The average binding energy per nucleon as a function of number of nucleons is a peaked function, with the maximum at iron (Fe^{56}). In general, to release energy, one can either combine elements on the left hand side of the peak, or split elements on the right hand side into other elements also on the right hand side. Figure taken from [1].

are met in a reactor, the ocean holds enough fuel to sustain year 2007 consumption levels for 2 billion years [16].

The "tokamak" approach has come very close to demonstrating the ability to produce more energy from fusion reactions than the energy required to run the reactor. A ratio of fusion power to input power of $Q = 0.64 \pm 0.05$ was achieved at the Joint European Torus (JET) [17]. The International Thermonuclear Experimental Reactor (ITER) [18] is a large tokamak designed to reach $Q = 10$, and is now under construction in France.

Despite the successes of the tokamak fusion approach, current scaled versions of these reactors suffer from disruptive events, where the fusion energy source is lost. These events will cause damage resulting in significant costs associated with the repairs and the downtime. The primary focus of this thesis is to better understand one of the common causes of this disruptive event, with the goal of providing the knowledge base necessary to avoid this type of disruption all together.

The reaction rate per unit volume sufficient for a reactor requires temperatures of about 20 keV [19], or 200 million degrees Celsius, which is around 14 times the estimated core temperature of the Sun [20]. In heating to these temperatures, matter undergoes a phase transition from a gas to a plasma. A plasma is an ionized gas where collective behavior (simultaneous many-body interactions, leading to small-angle deflections) dominates over binary collisions and large scattering angles [21]. The fusion plasmas discussed herein have relatively high temperatures and low densities relative to, for instance, the ionized gas in a wood fire. In a hot, diffuse fusion plasma, the length over which an electric potential decays, referred to as the Debye length λ_D (see reference [22] for a derivation), is significantly larger than the average distance between charged particles. Equivalently, the plasma parameter $\Lambda = n\lambda_D^3$ in such plasma is much greater than unity, where n is the plasma number density. Finally, one might also interpret the condition $\Lambda \gg 1$ as an indication that the kinetic energy of the charged particles is much greater than the Coulomb potential, except in the rare case of a binary collision. Although rare, it is during the binary collision of two fuel ions in a plasma with high kinetic energy that quantum tunneling may result in a fusion event. Plasmas respond to both the electromagnetic fields produced by its constituent particles, as well as to externally applied fields which are often dominant in fusion plasmas.

1.2 The Lawson Criterion and D-T fusion

The criterion for the energy produced by fusion to exceed the energy lost by Bremsstrahlung radiation, ignoring the conduction and convection losses of energy, is known as the Lawson criterion [23]. The radiation loss term used by Lawson is often replaced with the total thermal energy divided by an energy confinement time τ_E, thus accounting for all channels of energy loss (radiation, conduction, and convection). The power produced by fusion reactions per unit volume is given by $P_F = n_1 n_2 \langle \sigma v \rangle \mathcal{E}$ where n_1 and n_2 are the number densities of the reacting fuels, $\langle \sigma v \rangle$ is the reaction cross-section multiplied by the relative fuel ion velocity v averaged over a Maxwellian distribution

at temperature T, and $\mathcal{E}$ is the energy released per reaction. First generation fusion reactors will use deuterium and tritium (D-T) fuels, which produce an alpha particle and a neutron with energies $\mathcal{E}_\alpha = 3.5$ MeV and $\mathcal{E}_{neutron} = 14.1$ MeV respectively. The mean free path of neutrons in fusion plasmas is much larger than any feasible reactor dimension, and hence fusion neutrons do not heat the plasma[1]. Assuming a 50/50 fuel mix (i.e. $n_1 = n_2 = n/2$), and equating the fusion power available for plasma heating with the energy loss rate, we have,

$$\frac{1}{4}n^2\langle\sigma v\rangle\mathcal{E}_\alpha \geq \frac{3nk_BT}{\tau_E} \tag{1.1}$$

where k_B is Boltzmann's constant and T is the temperature of the plasma in thermodynamic equilibrium. Solving for $n\tau_E$ we find,

$$n\tau_e \geq \frac{12k_BT}{\langle\sigma v\rangle\mathcal{E}_\alpha} \tag{1.2}$$

This criterion provides the minimum product of the number density of fuel ions with the confinement time, $n\tau_E$, in order for the plasma to self-heat at a given temperature. This inequality is often cast into a pressure p times a confinement time, which we arrive at by multiplying by $2k_BT$. Using the experimentally measured D-T cross section averaged over a 15 keV Maxwellian distribution $\sigma(15\text{ keV}) = 3 \times 10^{-22}$ m^3/s, the product of pressure and confinement time evaluates to 8 atm·s [16]. The choice of $k_BT = 15$ keV here was not random, as it corresponds to the plasma temperature at which $p\tau_E$ is minimized. A fusion reactor need not be completely self-heated, but rather must generate more electrical power than is required to run the reactor.

[1]Some neutrons will be caught in a "lithium blanket" where they deposit heat and breed tritium. The neutrons that reach the metal structure of the vacuum vessel will "activate" the metal, rendering it radioactive. Nuclear engineering knowledge from fission reactors informs the structural metals to use which will result in relatively short half-lives on the order of 100 years [16].

1.3 Magnetic confinement

As implied by the Lawson Criterion, the particle constituents of the plasma, storing the thermal energy, must remain confined for a minimum timescale τ_E (note that the energy confinement time τ_E and the particle confinement time τ_P need not be the same, though are often similar in practice). A magnetic field can confine a plasma by making use of the Lorentz force which causes charged particles to gyrate around field lines. The radius of this gyration, referred to as the Larmor radius r_L, for a deuterium ion at 5 keV in a 2 Tesla magnetic field is $r_L = \sqrt{mk_BT}/eB \approx 0.5$ cm; thus, charged particles are confined to within ~ 0.5 cm of a given field line. Additionally, field lines need to be "closed", in the sense of not intercepting obstacles. If a fusion reactor were designed using magnetic field lines that pass through solid materials, the material would act like a heat sink to the hot plasma. A fusion plasma needs to be suspended in a vacuum, making no direct contact with any other material. The tokamak design accomplishes this by means of a toroidal field, although a poloidal component is also needed for confinement, as it will be discussed later.

An example of a tokamak where the vacuum vessel has been removed is shown in figure 1-2. A tokamak is a torus-shaped vacuum device that confines a torus-shaped plasma. It consists of many toroidal field coils that circle the short way around the torus (blue, and "D" shaped in the figure), referred to as the poloidal direction, producing magnetic field lines that travel the long way around the inside of the torus, referred to as the toroidal direction. A plasma generated on this torus of magnetic field lines is unstable to a radial expansion, so vertical field coils (labeled as "outer poloidal field coils" in the figure) and a plasma current (green arrow with the conical head) are added to prevent this.

A tokamak requires one more key element. Due to the gradient in the toroidal field, the ions drift downward while the electrons drift upwards, and then due to the resultant electric field E, the whole plasma drifts towards the outer wall, under the $\mathbf{E} \times \mathbf{B}/B^2$ drift that affects ions and electrons the same [24]. This undesired drift is fixed by driving a current through the plasma in the toroidal direction, producing

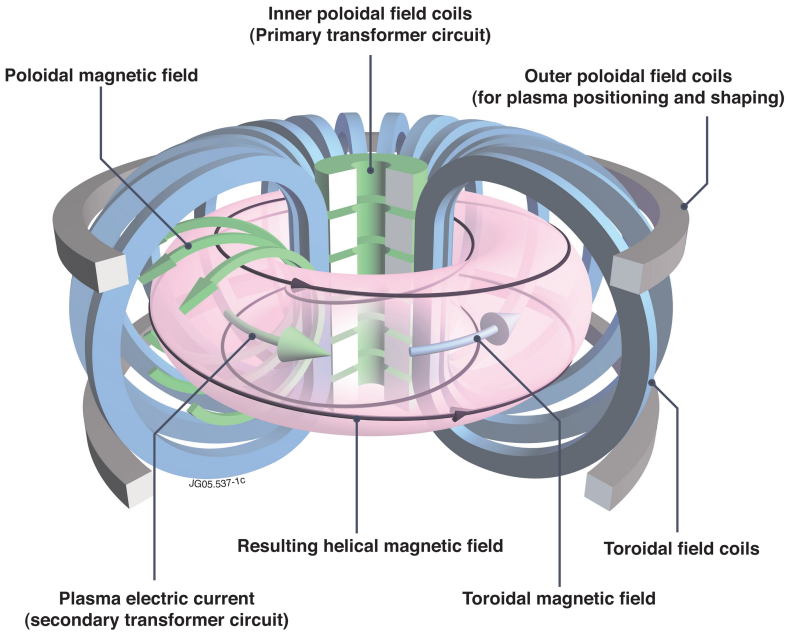

Figure 1-2: Schematic of the principal components of a tokamak, excluding the vacuum vessel. Figure from [2].

a magnetic field in the poloidal direction (poloidal field shown by the three green arrows in Fig. 1-2). The resultant magnetic field lines travel both in the toroidal and poloidal directions, following helical paths (black curves on the plasma surface in Fig. 1-2). A particle traveling along these field lines still drifts vertically, but over one full poloidal transit, the drift is away from the core half of the time, and towards the core during the other half, ultimately averaging to zero. Thus, there is no charge separation and the radial drift no longer occurs. However, three forces remain in the major radial direction owing to the so-called "tire tube force" resulting from the plasma pressure, the $1/R$ force due to plasma diamagnetism, and to an imbalance of poloidal field pressure between the inside and outside of the toroidal plasma current hoop [16]. All three of these outward major radial forces are balanced by applying a vertical field, which crossed with the plasma current, produces a balancing inward major radial force. Plasma confinement is now achieved.

The plasma current in the first tokamaks was driven in a way analogous to how currents are driven in an electrical transformer. Modern tokamaks are equipped to drive currents inductively in this way, using a central solenoid, but also use non-

inductive current drive techniques [25, 26, 27], or organize the plasma in such a way to produce a self-generated current referred to as the "bootstrap current".

1.3.1 Ideal MHD and the screw pinch

Magnetohydrodynamics (MHD) is a model that describes the dynamics of a plasma in thermodynamic equilibrium interacting with electric and magnetic fields. MHD is useful for establishing the conditions necessary for a stable plasma equilibrium, and thus we will focus on the timescales at which changes in the equilibrium occur. Tokamak fusion plasmas have a strong equilibrium field, where the magnetic pressure $B^2/2\mu_0$ is greater than the thermal pressure p (this ordering is actually a result of MHD stability). Perturbations of the thermal pressure with length scale a, where a is the plasma minor radius, along the field line equilibrate on the ion thermal transit time given by $a/v_{t,i}$ where $v_{t,i} \propto \sqrt{k_B T_i/m_i}$ is the ion thermal velocity and T_i and m_i are the ion temperature and mass respectively. Perturbations perpendicular to the field equilibrate on a timescale determined by the magnetic field pressure given by a/v_A, where $v_A = B/\sqrt{\mu_0 \rho}$ is the Alfvén velocity, and μ_0 and ρ are the permeability of free space and the fluid mass density respectively. As a result of $p < B^2/2\mu_0$, the ion thermal velocity is always slower than the Alfvén velocity in tokamaks. We therefore choose the timescale $a/v_{t,i}$ as the upper limit on the time required to establish an equilibrium, which is the timescale of interest for equilibrium MHD studies. The timescale for resistive diffusion of the magnetic field through the plasma is $\tau_R = \mu_0 a^2/\eta$, where η is the plasma resistivity. In fusion relevant plasmas τ_R is much longer than the $a/v_{t,i}$ MHD timescale, and therefore resistivity can often be neglected. The resulting model is referred to as Ideal MHD.

The MHD equations are rigorously derived from the kinetic equations in Ref. [28], and in the restricted realm of Ideal MHD in Ref. [29]. The first three moments of the kinetic equations provide the fluid conservation of mass, momentum, and energy for electrons and ions separately. To form a single fluid model, the ion mass density ρ and velocity $\mathbf{v}$ are used, the electron inertia is neglected, electron and ion velocities are used to define a current density $\mathbf{J}$, and the pressure p and temperature T are

taken to be the sum of the two fluid quantities. Two additional assumptions are needed to arrive at Ideal MHD: (1) the ions and electrons must be in thermodynamic equilibrium, requiring both ion-ion and electron-electron collision times that are short compared with timescales of interest, and (2) the ion Larmor radius $r_{L,i} = v_{t,i}/\omega_{c,i}$ must be much smaller than a ($\omega_{c,i} = q_i B/m_i$ is the ion gyrofrequency where q_i is the charge of the ion). Condition (2) is easily met in fusion experiments, while condition (1) is rarely met. Despite this discrepancy, Ideal MHD is observed to describe macroscopic fusion plasma behavior remarkably well. A detailed explanation of why this discrepancy does not affect the phenomena of interest is explained by Freidberg in [29].

The equations of Ideal MHD are as follows [29]:

$$\frac{\partial \rho}{\partial t} + \nabla \cdot \rho \mathbf{v} = 0 \tag{1.3}$$

$$\rho \left(\frac{\partial \mathbf{v}}{\partial t} + \mathbf{v} \cdot \nabla \mathbf{v} \right) = \mathbf{J} \times \mathbf{B} - \nabla p \tag{1.4}$$

$$\frac{d}{dt} \left(\frac{p}{\rho^\gamma} \right) = 0 \tag{1.5}$$

$$\mathbf{E} + \mathbf{v} \times \mathbf{B} = 0 \tag{1.6}$$

$$\nabla \times \mathbf{E} = -\frac{\partial \mathbf{B}}{\partial t} \tag{1.7}$$

$$\nabla \times \mathbf{B} = \mu_0 \mathbf{J} \tag{1.8}$$

$$\nabla \cdot \mathbf{B} = 0 \tag{1.9}$$

where $\gamma = 5/3$ is the ratio of specific heats, and the displacement current in Ampere's law is neglected since the Alfvén velocity is much less than the speed of light.

The cylindrical equilibrium configuration with an axial field only is referred to as the "Z-pinch". The strong axial field stabilizes ideal MHD modes. Although ideal MHD stable, the toroidal analog of the Z-pinch suffers from a major radial drift of the plasma, and from unbalanced major radial forces (the drift and the forces were discussed in section 1.3).

Alternatively, driving a plasma current in a toroidal geometry produces a poloidal field that eliminates the major radial drift, and force balance in the major radial direction can be controlled using a vertical field. The cylindrical configuration with only azimuthal fields produced by the plasma current is called the "Θ-pinch". Although offering a solution to the major radial drift and major radial force balance in the toroidal analog, the Θ-pinch is unstable to ideal MHD modes.

The "screw pinch" consists of a strong axial field produced primarily by external coils and a smaller azimuthal field produced by a plasma current. The screw pinch superimposes the Z-pinch and Θ-pinch solutions to simultaneously solve the ideal MHD problem, and the radial drift and radial force balance problems that arise in toroidal geometry. The screw pinch is the motivation for the toroidal equilibrium used in tokamak experiments.

The ideal stability of an equilibrium is well described by the Energy Principle, which determines if a displacement exists that reduces the potential energy of the plasma. As this work is focused on a resistive instability, which requires a non-ideal model, a thorough investigation of the ideal stability of the screw pinch is beyond the scope of this work, but may be found in reference [29].

1.3.2 The DIII-D tokamak

The DIII-D tokamak [30] is operated by General Atomics in La Jolla, California for the U.S. Department of Energy. DIII-D is capable of producing fusion relevant plasmas (see table 1.3.2) to conduct research in support of the worldwide fusion effort, including the ITER tokamak (ITER means "the way" in Latin) currently under construction at Cadarache in France.

The picture in figure 1-3 shows the inside of the DIII-D tokamak. The plasma

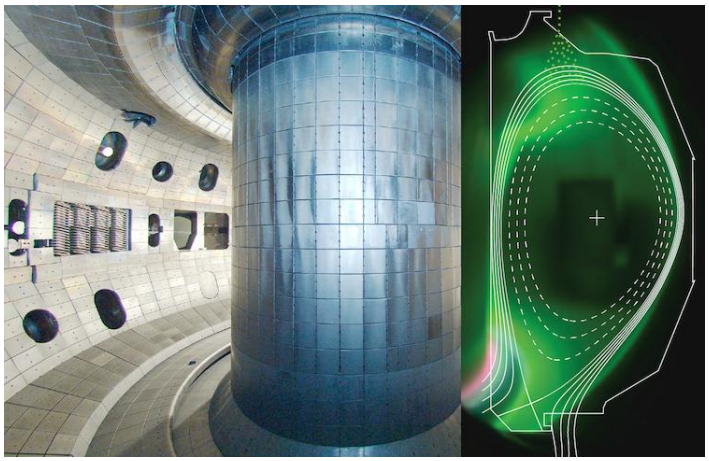

Figure 1-3: The inside of the DIII-D tokamak is shown on the left. A cross-section of the torus in the r and θ plane has a height of 2.3 m, and major radius of $R \approx 1.7$ m, and a minor radius $r \approx 0.7$ m. The image on the right shows the plasma during a lithium granule experiment. The colder lithium ions near the plasma edge produce green light as they recombine with electrons. The hottest region of the plasma does not radiate in the visible spectrum. The curved white contours are reconstructed cross-sections of the "flux surfaces" in the plasma, while the segmented contour outlines the wall. Image courtesy of General Atomics (left) and Steve Allen, Lawrence Livermore National Laboratory (right).

facing wall is made of graphite tiles, to handle high heat fluxes. Ports in the first wall are for input of heating, particles, and electromagnetic waves for probing purposes, as well as for output for diagnostic purposes.

Paramater	**Value**
R	1.7 m
r	0.6 m
I_p	1.2 MA
B_T	1.9 T
n	4×10^{19} m^{-3}
T_e	1-10 keV
T_i	1-10 keV

Table 1.1: Typical parameters for DIII-D plasmas. Shown are the major radius R, minor radius r, plasma current I_p, toroidal field B_T, particle number density n (typically deuterium plasmas, where $n_e \approx n_i = n$), electron temperature T_e, and ion temperature T_i.

The magnetic diagnostics on DIII-D will be used extensively in this work. Although the magnetic diagnostics vary greatly in size and shape [31, 32, 33], the fundamentals of the measurement are all identical. The magnetic diagnostics are

coils of wire, where the axis of the coil points in the direction of the measured field. Integrating Faraday's Law around a given sensor coil, we find $V_{sensor} = d\Phi/dt$ [31]. This voltage induced across the leads of the coil is integrated in time, resulting in a measurement of magnetic flux $\int V_{sensor} dt = \Phi$. Finally, assuming the field $\mathbf{B}$ to be locally uniform, the flux can be related to the field by $\Phi = N(\mathbf{B} \cdot \mathbf{A})$, where N is the number of loops of the coil, and $\mathbf{A}$ is the area of a single loop, with vector components pointing normal to the surface. The "magnetic probes" (Fig. 1-4) used to measure the poloidal and toroidal fields have a cross-sectional area of 7 cm^2, and vary in length from 2.8 to 14 cm [31]. Accounting for the number of turns in a given coil, the active area ranges from $NA = 120$ to 600 cm^2 [31].

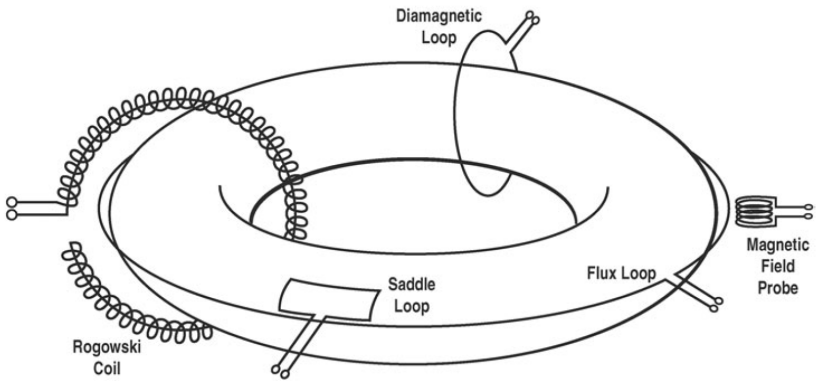

Figure 1-4: Schematic figure [3] of principal magnetic diagnostics used to monitor the tokamak plasma. The "magnetic field probe" and the "saddle loop" will be used extensively in this work. Copyright 2006 by the American Nuclear Society, LaGrange Park, Illinois.

The "saddle loop" magnetic diagnostics (Fig. 1-4) measure the radial field. The saddle loops used in this work are mounted on the outside of the vessel and span 60° each in the toroidal direction, and 1.2 m (74°) in the poloidal direction [31]. Due to their large span in the toroidal and poloidal directions, the assumption that $\mathbf{B}$ does not vary over the coil is not accurate. This spatial averaging effect will be accounted for in the analysis that follows. Further, the presence of the conducting vessel obscures measurements of fields that vary on a timescale comparable to, or shorter than the resistive diffusion time of the wall. When dealing with time-varying fields, the effect of resistive diffusion in the wall will also be accounted for.

In addition to magnetics measurements external to the plasma, the Motional Stark Effect diagnostic [34] will be used to determine the pitch of the magnetic field across the minor radius of the plasma. The MSE diagnostic measures the Stark splitting of lines emitted from injected neutral deuterium. The two components of the split line emission are polarized parallel and perpendicular to the magnetic field in the plasma. Frequency separation permits to isolate the component polarized perpendicularly to the magnetic field. Hence, measuring the polarization angle of such component in the laboratory frame translates in a measure of magnetic field pitch. The radial profile of the magnetic pitch is related to the profile of the safety factor q, which is in turn related to the current profile. The "peakedness" of the current profile is quantified by the scalar internal inductance l_i, which will be an important parameter in this work, used to describe plasma stability.

In a circular cylinder plasma configuration, Ampere's Law shows that measuring the azimuthally invariant field (analogous to the poloidal equilibrium field in toroidal geometry) outside the plasma provides no information on the radial distribution of current. In a circular cross-section toroidal geometry, the sum of the poloidal beta and half of the internal inductance $\beta_p + l_i/2$ can be constrained by external magnetics, but these quantities cannot be separated [35], and again, the distribution of the current profile is unknown. Finally, adding ellipticity to the plasma cross-section does allow determining β_p and l_i separately, but the value of the safety factor on axis is not well constrained [35]. Properties of the q and current profiles are central to this work, making the MSE diagnostic an indispensable tool in the following studies. The MSE and magnetics diagnostics are used to constrain equilibrium reconstructions [12], like the ones shown by the curved contours in figure 1-3.

In addition to magnetics measurements, the electron temperature profile will be studied. Two diagnostics are used to measure the electron temperature profile: the electron cyclotron emission (ECE) radiometer [36] and the Thomson Scattering (TS) diagnostic [37]. The ECE diagnostic measures the intensity of electron cyclotron radiation, which is linearly proportional to the electron temperature when the plasma is optically thick [38]. As per the name, emission occurs at the electron cyclotron

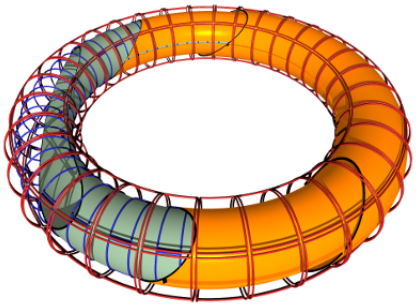

Figure 1-5: Rendering of the EXTRAP T2R vacuum vessel (gray), radial field sensors (blue), copper shells (copper color), and radial field actuator coils (red). Figure taken from reference [4].

frequency, therefore emission at a specific frequency originates in a specific radial location, due to the magnetic field being non-uniform and decaying approximately as $1/R$, where R is the major radius. The TS diagnostic measures the Doppler broadening of a probe laser that is scattered by electrons, and from this Doppler broadening, an electron temperature is inferred. The localization of the measurement results from the intersection of the optical view chord with the laser path [38].

Non-axisymmetric control coils are mounted both inside the DIII-D vessel, referred to as I-coils, and outside the vessel, referred to as C-coils (see red and orange coil sets in figure 1-7). The control coils are used both to correct for existing non-axisymmetric fields, and to apply additional fields used to manipulate magnetohydrodynamic (MHD) instabilities.

1.3.3 The EXTRAP T2R reversed field pinch

The EXTRAP T2R reversed field pinch (RFP) [14] is located at the KTH Royal Institute of Technology in Stockholm, Sweden. An RFP is similar in design to a tokamak, except the toroidal field is largely produced by currents in the plasma, and the average toroidal field is on the same order as the average poloidal field. As the name suggests, the magnitude of the toroidal field passes through zero and "reverses" near the edge of the plasma.

A rendering of principal components of EXTRAP T2R is shown in figure 1-5. The RFP is unstable to several magnetohydrodynamic modes. In the case of EXTRAP T2R, this motivated the installation of conductive copper shells surrounding the vessel (Fig. 1-5, copper colored), and an advanced feedback system to control

these instabilities [39, 40]. In the analysis that follows, a non-ideal MHD instability referred to as a tearing mode (see next section) will be used to diagnose imperfections in the equilibrium fields in EXTRAP T2R. Typical plasma parameters for EXTRAP T2R are shown in table 1.3.3.

Paramater	**Value**
R	1.24 m
r	18.3 cm
I_p	70-100 kA
n	$0.5 - 1.5 \times 10^{19}$ m^{-3}
T_e	200-400 eV

Table 1.2: Typical parameters for EXTRAP T2R plasmas [14, 15].

1.4 The tearing mode

A tearing mode (TM) is a non-ideal MHD plasma instability. The "classical" TM [41] occurs when free energy in the current profile overcomes the stabilizing pressure effects [42]. The current then becomes filamented on a surface where field lines, after m toroidal transits, return to the same point, referred to as a "rational surface". The "neoclassical" TM [43, 44] occurs when significant bootstrap current exists, but a local deficit of such current develops, at a rational surface. Such deficit is equivalent to a current filamentation, and is due to a large enough initial island seeded for example by a resonant field. Such island reduces the pressure profile, further reducing the bootstrap current and reinforcing the initial perturbation. The pitch of these fields lines relative to horizontal is related to the inverse of the safety factor $q = m/n$, where m is the previously mentioned poloidal harmonic, and n is the toroidal harmonic. It has been observed that plasma with higher values of q at the plasma edge tend to be more MHD stable [45, 46, 47, 48], hereby the name safety factor. This is supported by MHD stability analysis [49]. The amplitude of the current on this surface has m peaks in the poloidal direction, and n peaks in the toroidal direction (see figure 1-6). These m/n currents produce a perturbed field, much smaller than the equilibrium field, that also shares this m/n structure. These fields are sufficient to "tear" and

reconnect the equilibrium magnetic field, forming secondary regions isolated from the surrounding plasma called "magnetic islands". This tearing or reconnection process is analogous to the reconnection that occurs when a solar flare is ejected from Sun. A flux tube from the interior of a $m/n = 2/1$ island is shown by the pink helical structure in figure 1-7.

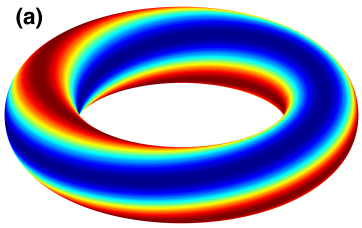

Figure 1-6: A model of a tearing mode showing the perturbed current distribution. This tearing mode has poloidal and toroidal harmonics m/n=2/1.

A magnetic island can be illustrated by tracing the trajectories of field lines near the resonant surface. To illustrate the three-dimensional helical structure in two dimensions, we define the helical angle $\chi = \theta - \frac{n}{m}\phi$, whose gradient is perpendicular to the magnetic field at the given m/n resonant surface. We will work in cylindrical geometry and take $\phi = z/R$. We then define the field component B^* in this perpendicular direction as [50],

$$B^*(r) = B_\theta \left(1 - \frac{n}{m} q(r)\right) \hat{\chi} \tag{1.10}$$

where the $\hat{\chi}$ direction is given by

$$\hat{\chi} = \frac{\hat{\theta} - (r_s/R)(n/m)\hat{z}}{\sqrt{1 + (r_s/R)^2 (n/m)^2}} \tag{1.11}$$

and where r_s is the resonant surface where the island forms. By construction, the B^* field goes to zero at the resonant surface where $q(r) = m/n$. Taylor expanding B^* to first order at the resonant surface we find [50],

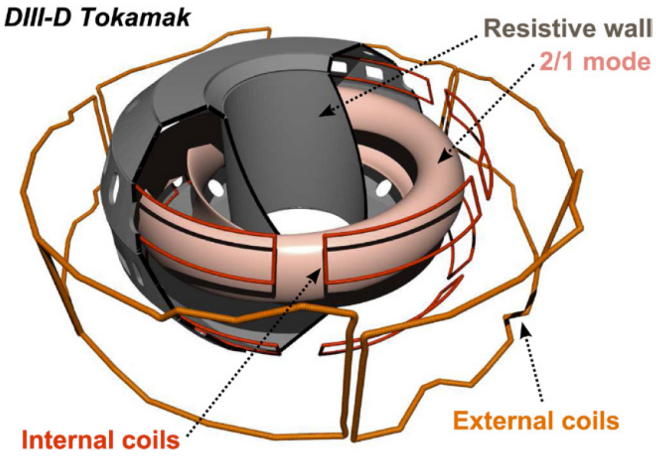

Figure 1-7: A tearing mode (tan) is shown in a cutaway of the DIII-D vacuum vessel (gray) [5]. This tearing mode (TM) circles toroidally twice before returning to the same point, and is therefore referred to as a $m/n = 2/1$ TM, where m is the poloidal harmonic, and n is the toroidal harmonic. The external and internal coils are magnets used to interact with the TM. Figure taken from [5].

$$B^*(r) \approx -\left(B_\theta \frac{dq/dr}{q}\right)_s (r - r_s) \tag{1.12}$$

where the first term inside parenthesis is evaluated at the radius of the resonant surface r_s. The B^* field about a given resonant surface is shown in figure 1-8a, where the resonant surface is shown by the dashed line. Applying a perturbed radial field at the resonant surface with a distribution given by $e^{im\chi}$, the magnetic topology is changed, resulting in the island structure shown in figure 1-8b. The center of the island is referred to as the O-point, and the point of connection between two islands is referred to as the X-point. The outer boundary of the island region is referred to as the separatrix.

Magnetic islands cause many problems that will be discussed in detail in this thesis, but we introduce the zeroth order effect on transport now. Transport of particles and heat in magnetically confined plasmas is fast in the direction parallel to the field, relative to the direction perpendicular to the field. When islands form and change the magnetic topology, the field lines at the separatrix connect across the radial region spanned by the island, allowing fast parallel transport in the radial direction.

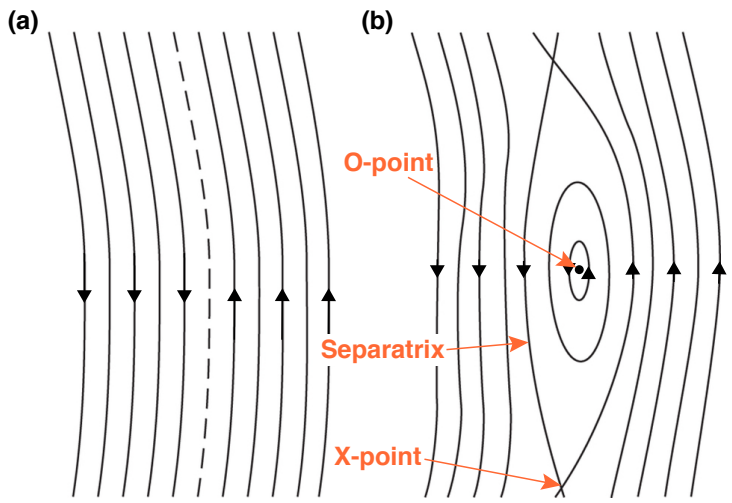

Figure 1-8: (a) Equilibrium field lines (solid) in the direction orthogonal to the helical field line on a resonant surface (dashed line). (b) Magnetic island resulting from a resonant radial field perturbation. Figure modified from [6]. Reprinted with permission from Nature Publishing group (https://www.nature.com/). Adapted by permission from Macmillan Publishers Ltd: Nature Physics [6], copyright (2016)

As a result, the density and temperature become uniform or nearly uniform ("flatten out") across the radial extent of the island. The degradation of the plasma thermal energy can be approximated in the case of a constant plasma density by assuming the temperature gradient is flattened within a "belt", or ring, in the poloidal plane centered about the rational surface where the island exists, and equal in width to the island. The temperature gradient in the plasma regions on the core-side and vacuum-side of the belt are assumed to be unaffected. This model is know as the "belt model" [51].

TMs rotate at a comparatively small velocity offset from the local plasma velocity. This offset is of the order of the ion or electron diamagnetic velocity, in NBI-heated or Ohmic plasmas, respectively, and depends on local gradients in temperature or pressure [52, 53]. In present tokamaks with strong torque injection, TM rotation frequencies often amount to several kHz. TMs can also steadily rotate at frequencies comparable to the inverse resistive-wall time (tens of Hz, typically), if a stable torque balance can be established at that frequency. In this case, they are called Quasi Stationary Modes (QSMs) [54]. Finally, if they are not rotating at all, or are evolving very slowly (compared with the inverse wall time) they are called Locked Modes (LMs, discussed further in section 1.6). In ITER, the rotation frequency at the location of

the $m/n = 2/1$ island is predicted to be ~ 300 Hz [55], which is significantly lower than present day devices, though the wall time is relatively long at 188 ms [56].

Modern tokamak plasma equilibria tend to be classically stable and neoclassically unstable [57]. However, saturated tearing modes significantly alter the plasma equilibrium, and might lead to classically marginal, or unstable conditions. Therefore, classical stability is of great interest in this work.

1.4.1 Reduced MHD

To better understand the structure of the perturbed field produced by TMs, what types of plasma current profiles are unstable, and the physics governing the evolution of macroscopic islands, we need an MHD model that retains resistive terms and thus allows magnetic reconnection. The equations we will derive with this model are the tearing flux eigenfunction equation, the classical stability index Δ', and the Rutherford equation.

Solutions were found for equilibria that are ideal MHD stable on the timescale $a/v_{t,i}$, but now we now wish to focus on resistive instabilities that occur on longer timescales. The reduced MHD model retains the resistive term in Ohm's law which relaxes the "frozen-in" [22] condition and allows the field to diffuse through the plasma. The tearing mode dynamics that we will study evolve on the resistive timescale, which is much longer than the ideal MHD timescale. We will impose a strong guide field in the $\hat{z}$ direction, and a weaker field in the plane perpendicular to the guide field, such that $|\mathbf{B}_\perp|/B_z \sim \epsilon$, where ϵ is a small parameter that we will use for ordering. It can be shown that the field direction $\hat{b} = \mathbf{B}/|\mathbf{B}|$ coincides with $\hat{z}$ up to second order in ϵ [58]. The tearing modes of interest will have parallel wave-numbers $k_\parallel = 1/Rq$ with $q \geq 1$ and perpendicular wave-numbers $k_\perp = 1/a$, such that $k_\parallel/k_\perp \sim \epsilon$. This implies an ordering of the gradients in the parallel and perpendicular directions of $\nabla_\parallel/\nabla_\perp \sim \epsilon$. Equipartition among kinetic, thermal and potential energy in the perpendicular plane gives [59, 60, 61],

$$\frac{\rho v_\perp^2}{2} \sim p \sim \frac{B_\perp^2}{2\mu_0} \tag{1.13}$$

where ρ is the mass density. This implies that $p \sim \epsilon^2$ (i.e. low β) and $v_\perp \sim \epsilon$. Given this ordering, on the resistive timescale, it may be assumed that the plasma is in equilibrium in the parallel direction. This can be seen by investigating the parallel component of the equation of motion,

$$\rho\left(\frac{\partial v_z}{\partial t} + \mathbf{v}\cdot\nabla v_z\right) = -\nabla_\parallel\left(p + \frac{B^2}{2\mu_0}\right) + \left[\frac{\mathbf{B}\cdot\nabla\mathbf{B}}{\mu_0}\right]\cdot\hat{z} \tag{1.14}$$

Writing $\mathbf{B} = B\hat{b}$, the magnetic tension term on right hand side may be rewritten as follows,

$$\frac{\mathbf{B}\cdot\nabla\mathbf{B}}{\mu_0} = \frac{B\hat{b}\cdot\nabla\hat{b}B}{\mu_0} = \frac{B^2(\nabla_\parallel\hat{b})}{\mu_0} + \frac{\hat{b}(\nabla_\parallel B^2)}{2\mu_0} \tag{1.15}$$

Note that the first term on the far right hand side, being the gradient of a unit vector, is in the perpendicular direction. Thus, we replace the magnetic tension term in equation 1.14 with the parallel term in equation 1.15 and find,

$$\rho\left(\frac{\partial v_z}{\partial t} + \mathbf{v}\cdot\nabla v_z\right) = -\nabla_\parallel\left(p + \frac{B^2}{2\mu_0}\right) + \frac{\nabla_\parallel B^2}{2\mu_0} = -\nabla_\parallel p \sim \epsilon^3 \tag{1.16}$$

We therefore have that $Dv_z/Dt \approx 0$, where $D/Dt = \partial_t + \mathbf{v}\cdot\nabla$, which implies that v_z =constant. In particular, we adopt a frame of reference in which $v_z = 0$.

Since the dynamics all occurs in the plane perpendicular to the guide field, we break the field into components as follows:

$$\mathbf{B} = B_{0z}\hat{z} + \nabla\times\psi\hat{z} \tag{1.17}$$

where B_{0z} is a constant, and all spatial dependence of the field is captured by $\nabla\times\psi\hat{z}$. Using the low frequency Ampere's law and equation 1.17, we have,

$$\mu_0 J_z = -\nabla^2\psi\hat{z} \tag{1.18}$$

Note that a term going like $\nabla(\nabla \cdot \psi\hat{z}) \leq \epsilon^2$ resulting from perpendicular currents $J_\perp$ was dropped here. This implies that $J_\perp \sim \epsilon^2$, which with the low frequency Ampere's law, shows that variations in $B_z \sim \epsilon^2$. We know that $\mathbf{B}_\perp \sim \epsilon$, and since the curl of $\psi\hat{z}$ in Ampere's law involves perpendicular derivatives of order 1, we have that $J_z \sim \epsilon$. Note that the ordering of $J_\perp \sim \epsilon^2$ is consistent with $\nabla \cdot \mathbf{J} = 0$ and the $J_z \sim \epsilon$ ordering we just found. It will be advantageous to use properties of the vector potential $\mathbf{A}$ from electrodynamics, so we choose $\nabla \times \mathbf{A} = \nabla \times \psi\hat{z}$ [58]. To equate $\mathbf{A}$ and $\psi\hat{z}$, we must also equate their divergences, according to the Helmholtz decomposition. We take $\nabla \cdot \psi\hat{z} \sim \epsilon^2 \approx 0 = \nabla \cdot \mathbf{A}$, and can now write $\mathbf{A} = \psi\hat{z}$. From electrodynamics, we can write $\mathbf{E} = -\partial_t \mathbf{A} + \nabla\chi$ where χ is the electric potential, and with the resistive Ohm's law $\mathbf{E} + \mathbf{v} \times \mathbf{B} = \eta\mathbf{J}$ and equation 1.18 we have [58],

$$-\frac{\partial\psi}{\partial t}\hat{z} + \mathbf{v} \times \mathbf{B} = -\eta\nabla^2\psi\hat{z} + \nabla\chi \tag{1.19}$$

Investigating the perpendicular component of this equation, one finds that the $(\mathbf{v} \times \mathbf{B})_\perp$ drift in the perpendicular plane is driven by the gradient of the electric potential $\nabla_\perp\chi$. The perpendicular velocity may be defined with a "stream function" ϕ where $\phi = \chi/B_{z0}$ as follows,

$$\mathbf{v}_\perp = \hat{z} \times \nabla\phi \tag{1.20}$$

This form for $\mathbf{v}_\perp$ implies that this model is incompressible in the perpendicular plane (i.e. $\nabla_\perp \cdot \mathbf{v}_\perp = 0$). Finally, after some vector algebra, the reduced MHD induction equation may be written as follows,

$$\frac{\partial\psi}{\partial t} = [\phi, \psi] - \eta\nabla^2\psi + B_{z0}\frac{\partial\phi}{\partial z} \tag{1.21}$$

where the brackets $[\phi, \psi] = \partial_x\phi\partial_y\psi - \partial_x\psi\partial_y\phi$ are the Poisson brackets [58]. This equation describes the advective and resistive evolution of the magnetic field in reduced MHD.

To complete the reduced MHD model, we investigate the fluid equation of motion in the plane perpendicular to the guide field. Specifically, we will look at the $\hat{z}$

component of the curl of the fluid equation of motion. We start by taking the $\hat{z}$ component of the curl of the fluid equation of motion,

$$\hat{z} \cdot \nabla \times \left[\rho \left(\frac{\partial \mathbf{v}}{\partial t} + \mathbf{v} \cdot \nabla \mathbf{v} \right) = \mathbf{J} \times \mathbf{B} - \nabla p \right] \tag{1.22}$$

Notice that this operation will annihilate the pressure gradient, and thus pressure effects will not be captured in the resulting equations. We will define the curl of the velocity to be the vorticity,

$$\bar{\omega} = \nabla \times \mathbf{v}_{\perp} = \nabla \times \nabla \times \phi \hat{z} \approx -\nabla_{\perp}^2 \phi \hat{z} \tag{1.23}$$

It can be shown using basic vector identities, and the properties $\nabla \cdot \bar{\omega} = \nabla \cdot v = 0$ that the $\hat{z}$ component of the curl of the convective derivative simplifies to $\mathbf{v} \cdot \nabla \bar{\omega}$ [58]. The $\hat{z}$ component of the curl of $\mathbf{J} \times \mathbf{B}$ reduces to $(\mathbf{B} \cdot \nabla) J_z$, where $\nabla \cdot \mathbf{B} = \nabla \cdot \mathbf{J} = 0$ was used, and the term $(\mathbf{J} \cdot \nabla) B_z \sim \epsilon^4$ was dropped. Finally, since the plasma is incompressible in the perpendicular direction, and sound waves quickly smooth out variations in the parallel direction, it is reasonable to take $\rho = \rho_0$ to be constant. We now have the following equation of motion,

$$\rho_0 \left(\frac{\partial \omega}{\partial t} + \mathbf{v} \cdot \nabla \omega \right) = (\mathbf{B} \cdot \nabla) J_z \tag{1.24}$$

We can make the replacement $\mathbf{v} = \nabla \times \phi \hat{z}$, and using Poisson brackets we have [58],

$$\rho_0 \frac{\partial \omega}{\partial t} = \rho_0 \left[\phi, \omega \right] + (\mathbf{B} \cdot \nabla)(-\nabla^2 \psi) \tag{1.25}$$

The vorticity equation describes how flows in the perpendicular plane respond to current gradients along the field line.

1.4.2 Tearing flux eigenfunctions

Understanding the radial structure of the perturbed fields that generate islands will allow prediction of island sizes from magnetics measurements, and will provide the basis for evaluating classical stability. In this subsection, we derive the differential

equation describing the perturbed flux function of the tearing mode. The plasma outside of a small region about the rational surface obeys the equations of ideal MHD. In response to a field perturbation, the plasma can kink, ensuring that no normal field exists on a given flux surface. This can be shown by first taking the curl of the ideal Ohm's law,

$$\nabla \times \mathbf{E} = -\nabla \times (\mathbf{v} \times \mathbf{B}) \tag{1.26}$$

We use Faraday's law for the left hand side, and linearize the resulting equation. Assuming no equilibrium flows we find

$$\delta \mathbf{B}_1 = \nabla \times \xi \times \mathbf{B}, \tag{1.27}$$

where ξ is the plasma displacement resulting from the integrated perturbed velocity. The radial component of the above equation, and the relations $q = rB_{z0}/RB_\theta$, where r is the minor radius, and B_θ is the equilibrium poloidal field, and $\delta B_{r1} = im\Psi/r$ yields the following [62],

$$\xi_r = \frac{\Psi}{B_\theta(1 - nq/m)} = \frac{m\psi}{r(\mathbf{k} \cdot \mathbf{B})} \tag{1.28}$$

This radial displacement ξ_r is the response of the plasma to a perturbed field for which $\mathbf{k} \cdot \mathbf{B} \neq 0$, where the wavenumber of the perturbed field evaluates $\mathbf{k} = (\frac{m}{r}\hat{\theta} - \frac{n}{R}\hat{z})$. When $\mathbf{k} \cdot \mathbf{B}$ is zero, the wavefront is parallel to the equilibrium field, and the plasma cannot kink in such a way to cancel the applied field. Note that the radial displacement in equation 1.28 goes to infinity as $\mathbf{k} \cdot \mathbf{B} \to 0$, and changes direction on either side of the rational surface. In reality, the *ideal* limit of Ohm's law is not valid in a small region about the rational surface called the "linear layer" [63], and instead the resistive term $\eta\mathbf{J}$ must be included. This resistive term will allow the perturbed radial field to penetrate the rational surface, causing tearing and reconnection of field lines from either side of the surface, resulting in a magnetic island.

Although this resistive layer is central to the tearing instability, we can use ideal reduced MHD to derive the perturbed flux function associated with the tearing mode

in the region outside the linear layer. We expect the tearing instability to grow on a timescale determined by resistive diffusion in the linear layer (i.e. $\tau_r = \mu_0 r_s \delta_s / \eta$ where r_s is the minor radius of the rational surface, δ_s is the linear layer width, and η is the plasma resistivity). Although the linear layer is thin such that $\delta_s \ll a$, resistivity in fusion plasmas is low, making the resistive timescale $\tau_r \gg a/v_{ti}$ (recall that the latter timescale is that of ideal MHD). It follows from this ordering that plasma inertia, at least in the ideal region outside the linear layer, is negligible for the tearing instability.

The ideal response of the outer region determines the behavior of eddy currents induced in the linear layer. Depending on the gradient of the equilibrium current, the kink displacement given in equation 1.28 can either be reinforced, or suppressed. When the eddy currents in the linear layer reinforce the applied field, the tearing mode is unstable. Stability to tearing modes occurs when the induced eddy currents act to cancel the applied field. To determine whether the ideal plasma response is stable or unstable to tearing, we investigate the vorticity equation (equation 1.25) with inertia terms neglected:

$$\mathbf{B} \cdot \nabla J_z = 0 \tag{1.29}$$

Note that we have used the relation $-\nabla^2 \psi = \mu_0 J_z$. Recall that this term resulted from $[\nabla \times (\mathbf{J} \times \mathbf{B})] \cdot \hat{z}$, so this condition requires that the curl of the $\mathbf{J} \times \mathbf{B}$ force in the perpendicular plane is zero. Linearizing this equation we have,

$$(\mathbf{B} \cdot \nabla J_z)_1 = (B_z \partial_z + B_\theta \partial_\theta) J_{z1} + B_{r1} (\partial_r J_{z0}) = 0 \tag{1.30}$$

where we have made use of $B_r = 0$ and $\partial_\theta J_z = \partial_z J_z = 0$ in the equilibrium. Finally, all perturbed quantities J_1, B_1, and Ψ can be Fourier-expanded in components that depend on the poloidal and toroidal coordinate as $e^{i(m\theta - n\phi)}$. The superposition principle allows us to restrict to a single component: the problem has been linearized and solutions can be superimposed. Noting that $B_{r1} = im\Psi/r$, $\nabla^2 \Psi = -\mu_0 J_{z1}$, and $q = rB_{\phi 0}/RB_{\theta 0}$, equation 1.30 can be rewritten as follows:

$$\nabla^2\Psi + \frac{\mu_0 J'(r)}{B_\theta(nq/m-1)}\Psi = 0 \tag{1.31}$$

where $J'(r) = dJ/dr$ [50]. This equation describes the spatial distribution of the perturbed flux function throughout the ideal regions of the plasma. Note that pressure does not appear in this equation as we took the curl of the fluid equation of motion, annihilating ∇p. It has been shown by Glasser, Greene, and Johnson that pressure has a stabilizing effect on the classical TM [42], referred to as the GGJ term. However, the effect scales with the inverse aspect ratio a/R, and is only significant in low aspect ratio plasmas such as spherical tori [57]. In general, for arbitrary equilibrium current profiles, an analytic solution for Ψ is not guaranteed, and therefore the solutions are often found numerically.

Rewriting equation 1.31 using equation 1.28 provides more intuition regarding how the ideal plasma response affects the solution of Ψ:

$$\nabla^2\Psi = \mu_0 \frac{\partial J}{\partial r}\xi_r \tag{1.32}$$

In this form, it is clear that the curvature in the perturbed tearing flux Ψ is driven by radial kinking in the presence of a radial equilibrium current gradient. As current is a flux function in ideal MHD (i.e. $\mathbf{J}\cdot\nabla p = 0$), a non-axisymmetric kink of a flux surface implies a non-axisymmetric redistribution of equilibrium current. The resulting perturbed current in the ideal region of the plasma J_{z1} is given by $J_{z1} = J'(r)\xi_r$. This perturbed current in the ideal region should not be confused with the eddy currents in the linear layer J_s. The latter currents are responsible for the jump in the radial derivative of the tearing flux across the rational surface, though they are related to the perturbed currents in the ideal region, as we will see in the next section.

The eigenfunctions of equation 1.31 describe the perturbed poloidal and radial fields of a tearing mode on the core-side and vacuum-side of the $q = m/n$ rational surface, where the m/n magnetic island forms. When J is small (or zero) in the region outside of the rational surface, the radial derivative may be neglected. Outer

solutions where it is assumed that $J'(r) \approx 0$ are referred to as "vacuum" solutions, and will be used in this work to map fields measured at the vessel wall to the rational surface where they are sourced.

1.4.3 Classical stability index

The classical stability index can be readily derived from equation 1.31. If we multiply by $r\Psi$, integrate over all r except within a small distance δ of the rational surface, and divide by $r_s\Psi^2(r_s)$, we find [50],

$$\frac{\Psi'(r)}{\Psi(r_s)}\bigg|_{r_s-\delta}^{r_s+\delta} = \frac{1}{r_s\Psi^2(r_s)}\left[\int_0^{r_s-\delta}\frac{\mu_0 J'(r)}{B_\theta(nq/m-1)}\Psi^2 r dr + \int_{r_s+\delta}^{a}\frac{\mu_0 J'(r)}{B_\theta(nq/m-1)}\Psi^2 r dr\right] \tag{1.33}$$

where the stabilizing term $(B_{1\theta}^2 + B_{1r}^2)$ is not shown in the integrands as its contribution goes to zero when we take $\delta \to 0$, the outer integral is truncated at the plasma boundary. Note that, in integrating the left hand side, we have treated Ψ as approximately constant within the narrow "linear layer", of thickness 2δ ("constant Ψ approximation"). The second derivative $\nabla^2\Psi$, however, is discontinuous and cannot be factored out of the integral. . The term on the left hand side of equation 1.33 is called the classical stability index, and is denoted as Δ'. When $\Delta' > 0$, the ideal response of the plasma outside the island reinforces the perturbed field, driving tearing mode growth. The right hand side shows how Δ' fundamentally depends on the derivative of the equilibrium current. As this expression for Δ' was derived from equation 1.31, pressure effects do not appear here, though the GGJ term has been shown to be stabilizing as the plasma β increases [42]. Including this GGJ effect, the condition for instability of classical TMs becomes $\Delta' > \Delta_c$, where Δ_c quantifies this stabilizing effect [49].

In DIII-D plasmas, current profiles are typically monotonically decreasing with r, and q profiles are typically monotonically increasing with r. For a rational surface internal to the plasma (i.e. such that $q_{min} < m/n < q_a$, where q_{min} is the minimum value of the safety factor, and q_a is the value of the safety factor at the plasma

boundary), inspection of equation 1.33 shows that the first integral is destabilizing, while the second integral is stabilizing. The width of the linear layer [64] evaluated at the $q = 2$ surface for typical DIII-D parameters is ~ 0.5 cm, which defines the length scale 2δ.

1.4.4 Modified Rutherford Equation

When a magnetic island has grown larger than the linear layer, its width evolution is described by the Modified Rutherford Equation (MRE) [64]. The classical form of the Rutherford equation, describing the evolution of a macroscopic island in response to the classical stability index Δ', can be derived from equation 1.21. First, we substitute equation 1.31 into the Laplacian, and note that the Poisson bracket and the term involving $\partial\phi/\partial z$ are small in the Rutherford regime [65]. Multiplying the resulting equation by $r\psi$ and integrating in r as we did in the derivation of the classical stability index, we find the evolution of ψ on the left hand side (or the evolution of the island width as $\psi \propto w^2$), and the classical stability index on the right hand side. In the more general form, additional current terms appear in equation 1.31 and result in modifications to the classical Δ'. The MRE takes many forms, but the following form includes all effects that will be studied in this work [57, 66]:

$$\frac{\tau_R}{r}\frac{dw}{dt} = \Delta'(w)r + \alpha\epsilon^{1/2}(L_q/L_p)\beta_p(r/w)\left[\frac{w^2}{w^2+w_d^2} - \frac{w_{pol}^2}{w^2}\right] + \Gamma\frac{w_v^2}{w}\cos(\Delta\phi) \quad (1.34)$$

Here τ_R is the resistive diffusion time, w is the island width, α is an ad hoc parameter accounting for the GGJ stabilizing effect [42] due to field curvature ($\alpha \approx 0.75$ for typical DIII-D parameters), $\epsilon = r/R$ is the local inverse aspect ratio, $L_q = q/(dq/dr)$ and $L_p = -p/(dp/dr)$ are the length scales of the q and pressure profiles, β_p is the ratio of the plasma pressure to the poloidal magnetic pressure, w_d is the island width below which perpendicular diffusion across the island is faster than parallel diffusion around the island, w_{pol} is the island width below which polarization currents are strongly stabilizing, Γ is a function depending on field geometry and boundary conditions,

w_v is the vacuum island width generated by a resonant field source external to the resonant surface, and $\Delta\phi$ is the toroidal phase difference between O-points of the TM and vacuum island. The first term on the right hand side shows how classical stability, derived in the previous subsection, affects the island evolution. The second term on the right hand side describes the effect of the perturbed bootstrap current, including small island stabilization effects captured by w_d and w_{pol}. The third term describes how a resonant field, not generated by currents at the resonant surface, affects the width evolution of the TM [66]. Similar forms of the MRE to equation 1.34 have been used to describe the evolution of NTMs in various experiments [67, 68, 69, 70].

1.5 Torques on tearing modes

1.5.1 The wall torque

In the previous section, we saw that tearing modes produce a perturbed magnetic field. This field is the result of the perturbation in the Ohmic current, or in the current that results from friction between magnetically trapped and passing electrons in the presence of a pressure gradient, referred to as the bootstrap current. The perturbed current and field associated with the tearing mode can interact electromagnetically with conducting structures and other sources of perturbed fields, such as those resulting from coil misalignments, referred to as error fields. These interactions result in torques on the tearing mode. An important torque that causes rotating tearing modes to lose their angular momentum, making them subject to locking in the lab frame to error fields, results from the interaction with the resistive vessel wall. We will derive this "wall torque" now, and then investigate the equation of motion to observe the locking bifurcation.

When a tearing mode rotates in the lab frame, the associated, non-axisymmetric field rotates as well, and induces eddy currents in the vessel wall. When the timescale for the resistive decay of such currents, τ_w, is comparable with the rotation period, a phase lag occurs between the TM field and the eddy current field, resulting in a

torque. As the eddy currents are driven by the field of the tearing mode, we start by deriving the tearing mode fields.

We will work in cylindrical geometry, which is a common approach for modeling large aspect ratio plasmas (i.e. where the major radius is much larger than the minor radius). As done in the previous section, we choose Fourier basis functions in the poloidal and z directions, and solve equation 1.31 for $\psi(r)$. The primary tearing mode of interest in this thesis will be the $m = 2$ and $n = 1$, where m and n are the poloidal and z (or toroidal) harmonics. This tearing mode occurs on the $q = m/n = 2$ surface that is typically relatively close to the edge of the plasma. Thus, it is a reasonable to assume the equilibrium current J_z to be zero outside of this surface. Making this assumption, we find what are referred to as "vacuum" solutions of equation 1.31, which are the solutions satisfying $\nabla^2 \Psi \hat{z} = 0$, where $\Psi = \psi(r) e^{i(m\theta - n\phi)}$ and $\phi = z/R_0$. In cylindrical coordinates, the equation writes $\Psi = \psi(r) e^{i(m\theta - nz/R_0)}$. In the large aspect ratio ordering, the z-derivate is order ϵ smaller than the poloidal and radial derivatives, and therefore the second derivative in z is neglected in the Laplacian. Polynomials in r are found to solve this reduced Laplacian in cylindrical coordinates, giving the solutions $\psi(r) \propto r^m$ and $\psi(r) \propto r^{-m}$. We will use these solutions to construct the flux function perturbation associated with the tearing mode $\psi_{mode}(r)$ and with the eddy currents $\psi_{wall}(r)$.

Following the derivation in section 3.2 of [64], we assume the ideal MHD response of the plasma to an externally applied resonant field. An external field described by a single Fourier basis function with poloidal and toroidal harmonics m and n is resonant on the surface where $q = m/n$. At this resonant surface, currents are induced in the plasma that "shield" the external field from penetrating the surface. In this wall torque derivation, the field produced by eddy currents in the wall will induce currents at the resonant surface that we refer to as δJ_{zswall}.

Under the assumption that $J_z(r > r_s) = 0$, the tearing perturbed flux takes the form [64]

$$\psi_{mode}(r) = |\Psi| \left(\frac{r}{r_{s+}} \right)^{-m} \qquad r > r_{s+} \tag{1.35}$$

where $|\Psi|$ is the reconnected magnetic flux at the rational surface, and $r_{s+} = r_s + w/2$ where r_s is the minor radius of the rational surface, and w is the full island width. The change in time of this flux at the vessel wall r_w produces an electric field that drives eddy currents, which produce their own magnetic flux. This flux is given by [64]

$$\psi_{wall}(r) \approx |\Psi| \left[\left(\frac{r}{r_{s+}} \right)^m - \left(\frac{r}{r_{s+}} \right)^{-m} \right] \frac{i(\omega\tau_w)(r_{s+}/r_w)^{2m}}{1 - i(\omega\tau_w)\left[1 - (r_{s+}/r_w)^{2m}\right]} \tag{1.36}$$

for $r_{s+} < r < r_w$ and where ω is the angular frequency of the TM. The flux outside the wall (i.e. where $r > r_w$) produced by eddy currents is given by [64]

$$\psi_{wall}(r) \approx |\Psi| \left(\frac{r}{r_{s+}} \right)^{-m} \frac{i(\omega\tau_w)\left[1 - (r_{s+}/r_w)^{2m}\right]}{1 - i(\omega\tau_w)\left[1 - (r_{s+}/r_w)^{2m}\right]} \tag{1.37}$$

where the finite width of the wall has been neglected.

Assuming the ideal MHD response of the plasma to the flux produced by eddy currents in the wall, a current δJ_{zswall} exists at the rational surface. "...(T)he 'toroidal' component of the 'sheet' current flowing in the island region owing to the presence of the conducting wall (i.e. the helical current at r_s due to ψ_{wall}) is given by"[64]

$$\delta J_{zswall} \approx 4\pi^2 R_0 \frac{m}{\mu_0} \left[\frac{(\omega\tau_w)^2 (r_{s+}/r_w)^{2m}\left[1 - (r_{s+}/r_w)^{2m}\right] - i(\omega\tau_w)(r_{s+}/r_w)^{2m}}{1 + (\omega\tau_w)^2\left[1 - (r_{s+}/r_w)^{2m}\right]^2} |\Psi| \right]. \tag{1.38}$$

This current is important as "...the part of δJ_{zswall} that is in phase with the island (i.e. in phase with $|\Psi|$...) modifies the island stability, whereas the part that is in phase quadrature gives rise to a $\mathbf{J} \times \mathbf{B}$ torque acting on the island"[64]. Solving for the poloidal component of this $\mathbf{J} \times \mathbf{B}$ torque, we find [64]:

$$\mathbf{T}_{wall} = -4\pi^2 R_0 \frac{m^2}{\mu_0} \frac{\omega\tau_w (r_s/r_w)^{2m}}{1 + (\omega\tau_w)^2\left[1 - (r_s/r_w)^{2m}\right]^2} |\Psi|^2 \hat{z}. \tag{1.39}$$

This poloidal torque can be converted to an axial torque by noting that $T_z =$

$-(n/m)T_\theta$ (see equation 7b in [64]). The wall torque decelerates the tearing mode, and the magnitude of this drag depends on the rotation frequency of the tearing mode, as shown in figure 1-9.

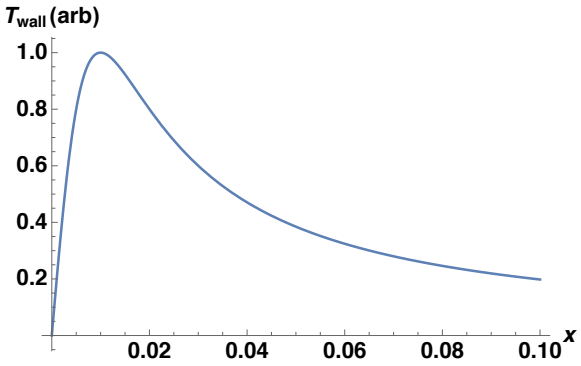

Figure 1-9: The drag torque resulting from resistive eddy currents in the vessel wall as a function of the normalized tearing mode rotation frequency $x = \omega/\omega_0$. Values of $\omega_0/2\pi = 5$ kHz and $(2\pi\tau_w)^{-1} = 50$ Hz were used to generate this curve.

The frequency $x = \omega/\omega_0$ of the tearing mode in figure 1-9 is normalized to the "natural" frequency, which is the frequency the mode rotates at when the island width is small and the wall torque is negligible. Both the inverse wall time $(2\pi\tau_w)^{-1} = 50$ Hz and the frequency $\omega_0/2\pi = 5$ kHz used in figure 1-9 are common values for DIII-D. The wall torque peaks at the inverse wall time ($x = 0.01$ in the figure) and vanishes at much higher or lower frequencies.

1.5.2 The error field torque

The error field torque results from the interaction of a tearing mode with poloidal/toroidal harmonics m/n with an external field with the same m/n. These external fields are often the result of coil misalignments, imperfections in their shapes, coil feed-throughs and other constructive details. External fields might also be intentionally applied by an operator using active coils. In general, the m/n tearing mode will respond to the superposition of all fields with the same m/n, including intrinsic error fields and operator applied fields. In toroidal geometry, modes with the same n but different m can interact, but this effect does not appear in the cylindrical model here.

We choose an error field produced by an external coil Ψ_{coil}. Following reference

[64], we will work in the frame of the tearing mode at the radial location of the rational surface r_s, where the error field, fixed in the lab frame, will appear to rotate with frequency $\omega(t)$. We allow for a time changing rotation frequency as the mode is expected to accelerate and decelerate once per rotation period in the presence of a resonant error, and thus in the mode reference frame, the error field will exhibit this behavior. The flux of the error field can be written as follows [64]

$$\Psi_{coil}(r,t) \approx |\Psi_{vac}| \exp\left(i \int^t \omega(t')dt'\right) \times \left[\left(\frac{r}{r_{s+}}\right)^m - \left(\frac{r}{r_{s+}}\right)^{-m}\right]. \tag{1.40}$$

where $r_{s+} = r_s + w/2$ and where w is the island width, and $|\Psi_{vac}|$ is the flux from the coil at the location of the rational surface in vacuum (i.e. without the response of the plasma).

"The 'toroidal' component of the 'sheet' current flowing in the island region due to the presence of the external perturbation (i.e. the helical current at r_s due to Ψ_{coil}) is given by"[64]

$$\delta J_{zscoil} = 4\pi^2 R_0 \frac{m}{\mu_0} \Psi_{vac} \exp\left(i \int^t \omega(t')dt'\right). \tag{1.41}$$

Note the ideal MHD response of the plasma has been assumed here (equations 61a, b of reference [64]). "... (T)he part of δJ_{zscoil} that is in phase with the reconnected flux Ψ at the rational surface modifies the island stability, whereas the part that is in phase quadrature gives rise to a $\mathbf{j} \times \mathbf{B}$ torque acting on the island"[64]. This $\mathbf{j} \times \mathbf{B}$ torque on the TM in the poloidal direction is given by [64]:

$$\mathbf{T}_{error} = -4\pi^2 R_0 \frac{m^2}{\mu_0} |\Psi_{vac}||\Psi_{mode}| \sin(\Delta\phi)\hat{z} \tag{1.42}$$

where $\Delta\phi$ is the phase difference between the O-points of the plasma and the vacuum islands, where the latter is the island resulting from superimposing Ψ_{coil} on the vacuum equilibrium fields. This poloidal torque can be converted to an axial torque by noting that $T_z = -(n/m)T_\theta$ (see equation 7b in [64]). In chapter 2 we will use

both the torque in equation 1.42 as well as the effect of the error field on the mode stability. For the tearing stability, we use the part of δJ_{zscoil} that is in phase with the reconnected flux Ψ. The tearing stability index is given by [64]:

$$\Delta'_{error} r_s = -2m \left(\frac{w_{vac}}{w} \right)^2 \cos(\Delta\phi) \tag{1.43}$$

where $w_{vac} \propto \sqrt{|\Psi_{vac}|}$. This term describes the stabilizing and destabilizing effect of an error field on a tearing mode, where stability depends on the relative angle between the error field and the tearing mode. We will use this term to explain the high frequency amplitude modulation of the tearing modes in chapter 2.

1.6 What is a locked mode?

A locked mode (LM) is a tearing mode that is not rotating in the lab frame. LMs can begin as rotating tearing modes that in response to electromagnetic torques applied by eddy currents in the vessel wall and by error fields [64], decelerate and lock. LMs may also be "born" locked, as a result of error field penetration [66]. Born locked modes will not be studied in this thesis.

LMs are known to degrade confinement [51] and cause disruptions in ITER relevant plasma conditions, and thus represent a concern for ITER [19]. LMs are observed in many tokamaks including JET [71, 7], NSTX [47], DIII-D [72, 73, 13], JT-60U [74], and KSTAR [75].

The locking of a rotating TM is a bifurcation of the TM, resistive wall, and error field system across a domain of rotation frequencies where a torque balance does not exist [64, 66, 76, 77, 5].

The dynamics of locked modes can be described by the following equation of motion [78],

$$I \frac{d^2\phi}{dt^2} = T_{wall} + T_{EF} + T_{RMP} + T_{TM} + T_{Visc} + T_{NBI} \tag{1.44}$$

where I is the inertia associated with the LM, ϕ is the toroidal position of the LM,

T_{wall} is the drag torque applied by the resistive wall, T_{EF} is applied a resonant error field (EF), T_{RMP} captures the torque from applied resonant magnetic perturbations (RMPs), T_{Visc} is the torque imparted by sheared flow, and T_{NBI} is the injected neutral beam torque. Note that the last two torques are imparted to the plasma layer in which the island is partially "frozen". A numerical model was developed [5] to study the inertial, wall, EF, and RMP torques, with the ability to model viscous and neutral beam torques as a constant, background torque.

1.6.1 The locking bifurcation

The drag imposed by the resistive wall on a tearing mode can become large enough that the viscous restoring torque is unable to maintain a "high frequency solution", resulting in a bifurcation of the torque balance to a "low frequency solution", where low and high frequency are relative to the inverse wall time. In the presence of an error field, and provided the zero frequency viscous torque is not larger than the peak error field torque, the tearing mode will lock to the error field, and thus attain a zero frequency solution. To demonstrate this downward bifurcation, we start with a simple equation of motion including the decelerating wall torque and the restoring viscous torque,

$$I\frac{d\omega}{dt} = \mathbf{T}_{wall} + \mathbf{T}_{visc} \tag{1.45}$$

where I is the moment of inertia associated with the tearing mode. The viscous torque is a result of momentum exchange between nearby flux surfaces in the plasma resulting from collisions. Part of this torque is indirectly imparted to the island, which is partly "frozen in" a plasma layer. When the wall torque decelerates the TM, the nearby plasma which is not directly affected by the wall torque delivers some momentum to the TM through collisions, thus acting as an accelerating torque. The wall torque is derived in the previous subsection (equation 1.39), and we use a simple model for the viscous torque where the force is proportional to the difference of the rotation frequency from the natural frequency $\Delta\Omega = \omega_0 - \omega$,

$$I\frac{d\omega}{dt} = -4\pi^2 R_0 \frac{m^2}{\mu_0} \frac{\omega\tau_w (r_s/r_w)^{2m}}{1+(\omega\tau_w)^2\left[1-(r_s/r_w)^{2m}\right]^2} |\Psi_{mode}|^2 + r_s \alpha\mu\Delta\Omega \tag{1.46}$$

where μ is a kinetic perpendicular viscosity and α is a scaling factor. We now search for steady state solutions of this equation by setting the time-derivative equal to zero:

$$0 = \frac{\omega\tau_w}{1+(\omega\tau_w)^2} - \frac{(\alpha r_s \mu\omega_0)}{4\pi^2 m^2 R_0 (r_s/r_w)^{2m} |\Psi_{mode}|^2/\mu_0} \left(1-\frac{\omega}{\omega_0}\right) \tag{1.47}$$

The approximation $\left[1-(r_s/r_w)^{2m}\right]^2 \approx 1$ was made, and is applicable to all tearing modes of interest here. We define a normalized rotation frequency $x = \omega/\omega_0$, and a parameter, $z = \omega_0\tau_w$, which is large when the natural rotation frequency is larger than the inverse wall time. The ratio f is defined as the ratio between the peak-values of wall torque and viscous torque (note that these peaks occur at different frequencies, $\omega\tau_w = 1$ and $\omega = 0$). Using these definitions, the equation simplifies to the following:

$$0 = \frac{xz}{1+(xz)^2} - \frac{1}{2f}(1-x) \tag{1.48}$$

The roots of this equation are torque balance solutions. For values $z < 5$, there are no bifurcations, but rather a smooth transition from a high-frequency to a low-frequency. For typical tearing modes in both DIII-D and EXTRAP T2R plasmas, $z \gg 5$, and therefore this low z region is not of interest for this work.

Equation 1.48 can be solved for $f(x; z = 100)$ which describes the wall-viscous torque ratio f necessary for torque balance to be established at a given rotation frequency x in typical DIII-D plasmas (where modes initially rotate at or above 5 kHz, i.e. 100 times faster than the inverse wall time).

The blue curve in figure 1-10 is the function $f(x; z = 100)$. With good approximation it is a parabola, as it follows from Eq. 1.48 for $x \ll z$=100. Note however how $f \to \infty$ for $x \to 0$. The orange and green horizontal lines in figure 1-10 mark the transitions between solution regions. For $0 < f < 1$ (below the orange line, when the viscous torque dominates), one torque balance solution exists at high frequency. At

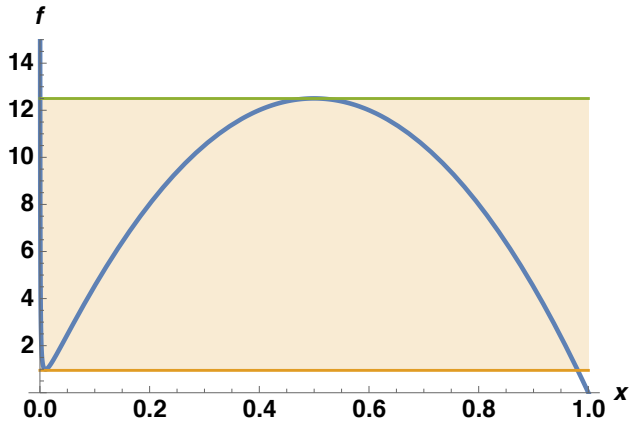

Figure 1-10: The ratio of the wall torque to the viscous torque f which preserves torque balance as a function of the normalized rotation frequency $x = \omega/\omega_0$. The horizontal orange line at $f = 12.5$ shows the approximate torque ratio that leads to mode locking. For higher values of f, the mode remains locked. To unlock, f must decrease below 1.

$f \approx 1$, two solutions exist, where the low frequency solution is a double root. This double root is referred to as a "half-stable" root [79], as a zero frequency tearing mode will accelerate towards this root, and if it "overshoots" due to inertia, the mode bypasses this solution and continues to accelerate to the high frequency stable root. In the shaded region between the orange and green lines, three torque balance solutions exist. The high and low frequency solutions are stable, while the intermediate solution is unstable. At $f \approx 12.5$, the intermediate and high frequency solutions become degenerate, and we again have a half stable root. This root behaves opposite to the $f \approx 1$ half stable root: if a high frequency tearing mode decelerating towards this solution "overshoots", it continues to decelerate to the low frequency stable solution. Finally, for $f > 12.5$ (above the green line, when the wall torque dominates), only a low frequency solution exists.

For an equivalent discussion of how many roots exist for torque balance, and whether they are stable, let us consider figure 1-11. This shows five wall torque curves (for five different island widths w) and one viscous torque curve (denoted by the thick brown line) as functions of the normalized frequency, to be precise, the negative of the wall torque T_{wall} is plotted; its intersections with the T_{visc} curve represent torque balance. From equations 1.47 and 1.48, we see that $f \propto |\Psi_{mode}|^2$, which implies that

$f \propto w^4$. When the island is small, so is T_{wall}, and balance with T_{visc} can only be established at high x (blue case). For increasing w, a second, degenerate root appears at low frequency (orange), which then splits (green). Above a critical island width (red), the high-frequency solution disappears (purple).

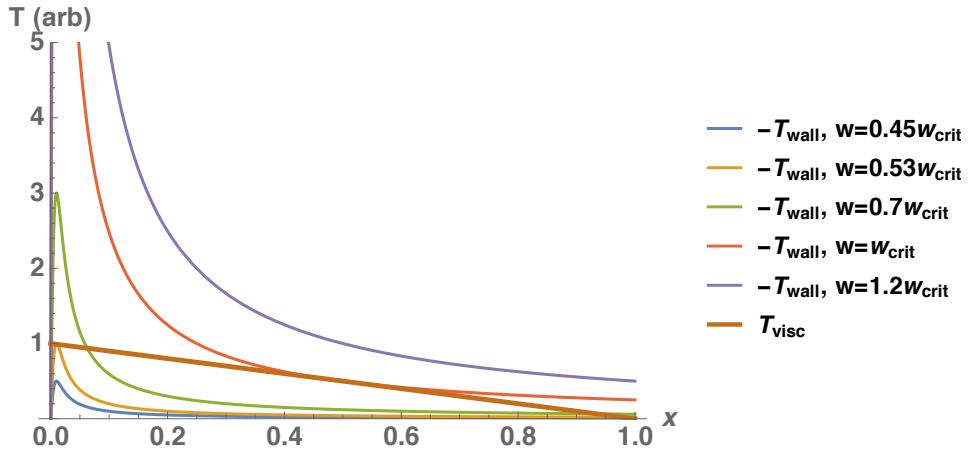

Figure 1-11: Curves of wall torque compared with the viscous torque. As the island width w increases, the wall torque scales like w^4. The blue and orange curves exhibit three intersections with the viscous torque (red), representing three torque balance solutions. The green curve shows the critical island width w_{crit} (corresponding to $f = 12.5$ in figure 1-10) above which, only a low frequency solution exists.

The wall torque curves in figure 1-11 demonstrate how a high frequency tearing mode locks. When tearing modes are seeded or driven unstable, they start rotating at normalized frequency $x = 1$. As the tearing mode grows, T_{visc} grows like the island width w and T_{wall} grows more dramatically, like w^4. This results in mode deceleration. For every new (greater) w, torque balance is established at a new (lower) frequency x. Note that this is still the "high-frequency" solution in figures 1-10 and 1-11. At a critical island width w_{crit}, corresponding to $f = 12.5$ in figure 1-10 and the red curve in figure 1-11, the high frequency solution becomes degenerate, and half stable. In this simplified treatment, restricted to the wall and viscous torques, this half stable solution occurs at approximately half of the natural frequency (i.e. at $x \approx 0.5$). At this half stable root, a small increase of the island width causes the system to bifurcate to the low frequency solution. This low-frequency solution does, indeed rotate at low frequency, lower than the inverse wall time (tens of Hz at DIII-D). It is called Quasi Stationary Mode [54]. However, low frequency implies low wall and viscous torques.

Consequently, if error fields are present and sufficiently strong, the error field torque dominates over the other torques, and causes the mode to lock.

Figure 1-10 also shows that the locking and unlocking thresholds in f, or equivalently in the island width w, are different. For $z = 100$, a locked or quasi-stationary island width must reduce by at least 50% to unlock, as shown by the orange curve in figure 1-11, corresponding to an island width of $w = 0.53 w_{crit}$. To unlock an island in this way, the width can be reduced by driving current with microwave injection [80], or it might be reduced passively by a minor disruption.

1.7 What is a disruption?

A disruption is a fast loss of energy and particles from the plasma, where fast is relative to the typical timescales for heat and particle transport, and resistive diffusion ($\tau_E \approx 100$ ms and $\tau_R \approx 0.5 - 2$ s in DIII-D). The thermal energy in DIII-D is lost in a few milliseconds, while the energy in the poloidal magnetic field is lost in tens of milliseconds. The toroidal magnetic field is not greatly affected during a disruption, as the majority of this field is produced by coils external to the plasma which maintain the field throughout the disruption.

Disruptions are a concern as they release a vast amount of energy in a short amount of time, and can damage the machine. The thermal energy is deposited on the walls of the confining device. The loss of poloidal magnetic energy by the rapid decay of plasma current induces high currents in the surrounding conductors, which interact with the strong toroidal field, causing high electromagnetic stresses.

Many events can cause disruptions, as evidenced by the flowchart in figure 1-12. The locked mode is a common element in many of the disruption chains, and is the terminating event in 20% of the 1654 disruptions presented in this chart [7]. Eventually, nearly all disruptions at JET exhibit signs of Mode Locking, as illustrated by the ML block on the right in figure 1-12.

The plasma contains a large amount of energy stored in the kinetic energy of its particle constituents, and separately in the magnetic field produced by currents in the

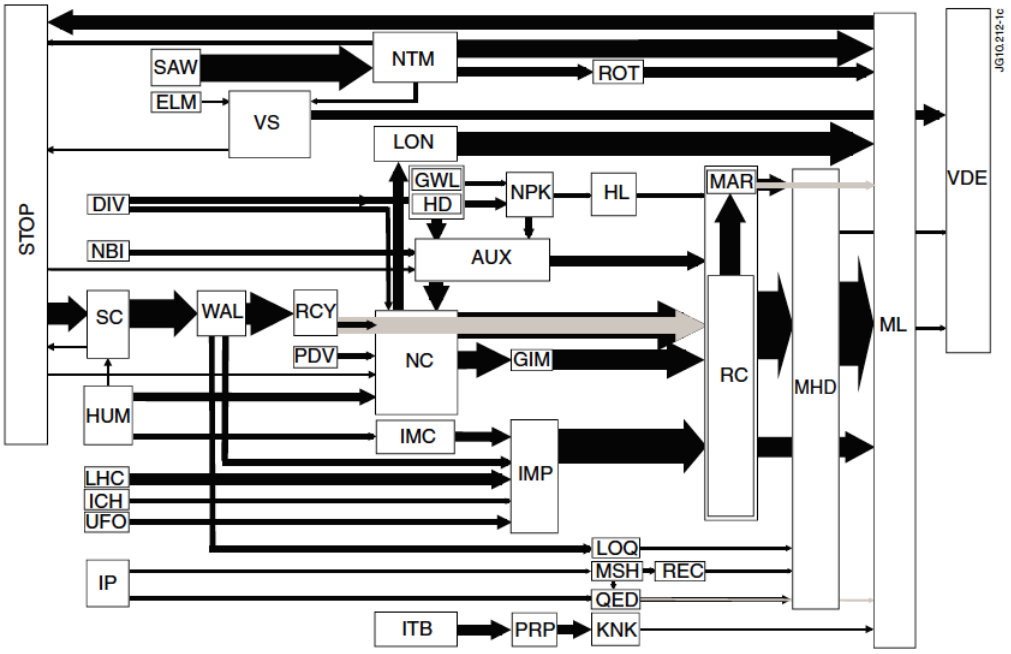

Figure 1-12: Flowchart showing the various causes of 1654 unintentional disruptions in JET [7]. The size of the arrow represents the number of events that follow the given path. Locked modes are responsible for 20% of the disruptions here [7], though they appear as part of the evolution in many more, virtually all disruptions, as exemplified by the large "ML" block on the right, for "mode locking". Other notable acronyms are emergency stop (STOP), neoclassical tearing mode (NTM), magnetohydrodynamic instabilities (MHD), and vertical displacement events (VDE). For a full list, see [7]. Reprinted with permission from Nuclear Fusion.

plasma. A typical DIII-D plasma contains 1-2 MJ (mega-joules) of thermal energy, and 0.5-1.5 MJ of magnetic energy in the plasma current (note that the toroidal field, produced by magnets outside the plasma, typically stores 25-50 MJ).

In ITER, the stored energy will be considerably larger. The plasma pressure will be ~ 7 times that of DIII-D, and the volume is roughly 70 times larger [18]. Therefore, the stored thermal energy in ITER is roughly 500-1000 MJ. The poloidal field energy scales roughly as the plasma current squared (15 MA in ITER [18]) times the inductance, which gives approximately 250-750 MJ in the poloidal field. Disruptions in ITER must be nearly completely avoided, as the sudden release of this very high energy could cause significant damage [19]. For comparison, the energy released is $\sim$500 times higher than at DIII-D, but is deposited in a comparable timescale over surfaces and volumes which are only about 16 and 64 times, respectively, greater than at DIII-D.

1.8 Overview of the following chapters

This thesis is organized into three body chapters. Chapter 2 presents work [81] on the detection of error fields using naturally rotating TMs in EXTRAP T2R. Although this work is conducted on a reversed field pinch, the fundamental physics underlying the technique is common to the tokamak. Error fields, when undetected, and thus uncorrected, apply braking torques to rotating TMs that can result in locking [64], and in addition, can produce born LMs. Chapter 3 presents a statistical survey of LMs at DIII-D [13], with a focus on what differentiates disruptive from non-disruptive LMs. This statistical work confirmed some expectations regarding how LMs cause disruptions, and challenged others, and provided insight for a detailed study on a small subset of discharges. The final body chapter, chapter 4, presents this small-scale study on the relationship between locked islands and thermal collapses in DIII-D. These results are suggestive of the fundamental mechanisms that cause the thermal collapse, which is often the first, distinct step in a full disruption.

Chapter 2

Local measurement of error field using naturally rotating tearing mode dynamics in EXTRAP T2R

Abstract.

An error field (EF) detection technique using the amplitude modulation of a naturally rotating tearing mode (TM) is developed and validated in the EXTRAP T2R reversed field pinch. The technique was used to identify intrinsic EFs of $m/n = 1/-12$, where m and n are the poloidal and toroidal mode numbers. The effect of the EF and of a resonant magnetic perturbation (RMP) on the TM, in particular on amplitude modulation, is modeled with a first-order solution of the Modified Rutherford Equation. In the experiment, the TM amplitude is measured as a function of the toroidal angle as the TM rotates rapidly in the presence of an unknown EF and a known, deliberately applied RMP. The RMP amplitude is fixed while the toroidal phase is varied from one discharge to the other, completing a full toroidal scan. Using three such scans with different RMP amplitudes, the EF amplitude and phase are inferred from the phases at which the TM amplitude maximizes. The estimated EF amplitude is consistent with other estimates (e.g. based on the best EF-cancelling RMP, resulting in the fastest TM rotation). A passive variant of this technique is also presented, where no RMPs are applied, and the EF phase is deduced.

Available at https://doi.org/10.1088/0741-3335/58/12/124001

Chapter 3

Statistical analysis of $m/n = 2/1$ locked and quasi-stationary modes with rotating precursors at DIII-D

Abstract.

A database has been developed to study the evolution, the nonlinear effects on equilibria, and the disruptivity of locked and quasi-stationary modes with poloidal and toroidal mode numbers $m = 2$ and $n = 1$ at DIII-D. The analysis of 22,500 discharges shows that more than 18% of disruptions are due to locked or quasi-stationary modes with rotating precursors (not including born locked modes). A parameter formulated by the plasma internal inductance l_i divided by the safety factor at 95% of the poloidal flux, q_{95}, is found to exhibit predictive capability over whether a locked mode will cause a disruption or not, and does so up to hundreds of milliseconds before the disruption. Within 20 ms of the disruption, the shortest distance between the island separatrix and the unperturbed last closed flux surface, referred to as d_{edge}, performs comparably to l_i/q_{95} in its ability to discriminate disruptive locked modes. Out of all parameters considered, d_{edge} also correlates best with the duration of the locked mode. Disruptivity following a $m/n = 2/1$ locked mode as a function of the normalized beta, β_N, is observed to peak at an intermediate value, and decrease for high values. The decrease is attributed to the correlation between β_N and q_{95} in the DIII-D operational space. Within 50 ms of a locked mode disruption, average behavior includes exponential growth of the $n = 1$ perturbed field, which might be due to the 2/1 locked mode. Surprisingly, even assuming the aforementioned 2/1 growth, disruptivity following a locked mode shows little dependence on island width up to 20 ms before the disruption. Separately, greater deceleration of the rotating precursor is observed when the wall torque is large. At locking, modes are often observed to align at a particular phase, which is likely related to a residual error field. Timescales associated with the mode evolution are also studied and dictate the response times necessary for disruption avoidance and mitigation. Observations of the evolution of β_N during a locked mode, the effects of poloidal beta on the saturated width, and the reduction in Shafranov shift during locking are also presented.

Available at https://doi.org/10.1088/0029-5515/57/1/016019

Chapter 4

Relationship between locked islands and thermal collapses in DIII-D

This chapter originated from the profile analysis of some locked mode discharges, following the locked mode database work of the previous chapter. While "automatically" I investigated hundreds of discharges from the locked mode database, interesting phenomena in the electron temperature profile were observed, prior to each thermal quench, which motivated the more detailed, "manual" analysis presented in this chapter. All sections in this chapter were written by the author. Experimental observations suggested the presence of stochastic fields, prompting the author to ask V. Izzo to investigate a single discharge using the NIMROD [128] 3D nonlinear MHD code. Initial conditions for these simulations were provided by the author with assistance from O. Meneghini. Figures 4-8 and 4-9 show the results of these simulations and were produced by V. Izzo. The section describing these results was written by the author. The divertor heat flux analysis shown in figure 4-6 was done by M. Knolker. The magnetics analysis technique in section 4.2.1, all temperature profile observations and magnetics analysis regarding the thermal collapse in section 4.3, and the observations of the major disruptions and the self-stabilizing locked modes in sections 4.5 and 4.6 were made by the author.

Disruptions pose a significant problem for reactor scale tokamaks. This chapter presents the first empirical measurements on DIII-D of multiple locked islands growing to a width at which they are expected to overlap and generate stochastic fields. Multiple locked islands are observed to exist prior to the disruption precursor referred to as the $T_{e,q2}$ collapse. Further, the O-points of the outermost $n = 1$ islands are observed to align at the outboard or inboard midplanes prior to the onset of the $T_{e,q2}$ collapses, which is an unexpected result. The observations here improve our understanding of disruptions, and might better inform disruption avoidance and mitigation techniques.

4.1 Introduction

Improving our physical understanding of the processes leading up to a disruption might lead to better disruption prediction and avoidance, which are considered a requirement for the success of ITER [19] and future reactor-scale tokamaks.

It is well known that locked modes [129], when not controlled (for instance by a combination of applied magnetic perturbations and Electron Cyclotron Current Drive [80, 130, 131]) are one of the main causes of disruptions. This was shown, among others, in statistical studies of disruptions at JET [46, 7] and NSTX [47] and in a statistical study of locked modes with rotating precursors at DIII-D [13]. Notably, nearly all disruptions at JET exhibit signs of mode locking, as illustrated by the "ML" block in Fig. 4 of Ref.[7].

The physics of locked mode disruptions and the role of locked modes in other types of disruptions are not well understood. Here "other types" include disruptions due to high density, low safety factor q or high normalized pressure, β [132, 104, 19, 108].

The coupling between MHD stability and transport during disruptions was simulated in the 1980's [119, 120]. Detailed observations of locked modes in density-limit disruptions were reported on JET discharges [71]. Locked modes have also been observed during massive gas injection at DIII-D [133, 92], and similar conditions have been simulated in Alcator C-Mod [107]. Recently, two- and three-dimensional elec-

tron temperature measurements of locked-mode-induced minor and major disruptions were made at KSTAR [75].

In this work we analyze the evolution of electron temperature profiles in the presence of multiple locked islands during a particular type of thermal collapse that affects the outer $\sim 60\%$ of the profile, with little effect on the core. This type of collapse is referred to as a $T_{e,q2}$ collapse, where the subscript refers to the $q = 2$ rational surface where the dominant locked island, of poloidal/toroidal mode number m/n=2/1, forms. The $T_{e,q2}$ collapse is observed to be the first stage in the full thermal collapse of most locked mode disruptions in DIII-D.

In this work, we draw a distinction between types of thermal collapses, which are the minor disruption, and the $T_{e,q2}$ collapse. The $T_{e,q2}$ collapse is usually the first stage of the minor disruption, where the outer $\sim 60\%$ of the electron temperature profile collapses, with little effect on the core. The distinction between a minor disruption and a $T_{e,q2}$ collapse is then the fast collapse of the core temperature in the former, or a full recovery of the temperature profile in the latter. Not all minor disruptions begin with a $T_{e,q2}$ collapse, as some exhibit a single global collapse of the entire temperature profile instead of the two staged outer and core collapses.

Similar to a $T_{e,q2}$ collapse often being a distinct stage in the minor disruption, a minor disruption may be thought of as a common distinct stage in the major disruption. A minor disruption is characterized by a complete loss of thermal energy. Following a minor disruption, the temperature profile might recover, or a current quench is initiated, turning the minor disruption into a major disruption. In all disruptions caused by locked modes, the minor disruption is the first stage of a major disruption. Disruptions do exist, for example those caused by vertical displacement events (VDEs), where the thermal and current quenches occur simultaneously. Note that although it is possible for a LM to cause loss of vertical stability, leading to a VDE disruption, from a physics standpoint, we do not consider this a LM disruption as the physics of the terminating event is different.

Using electron temperature diagnostics in different toroidal and poloidal locations, the $T_{e,q2}$ collapse is shown to be consistent with an axisymmetric collapse. In dis-

charges where 3D magnetics analysis is performed, the collapse appears coincident with the alignment of island O-points on the midplane, or with growth of the locked islands, or both. Energy conservation analysis conducted on one of these collapses shows that the primary channels for energy loss are radiation localized in the divertor and conduction or convection to the divertor. Nonlinear MHD simulations were conducted with the NIMROD code [128]. The simulations were initialized with a DIII-D equilibrium prior to a $T_{e,q2}$ collapse, and evidenced the formation of large regions of stochastic fields outside of the $q = 2$ surface. This is consistent with measurements of wide, closely spaced magnetic islands, which, if overlapping, cause stochastic fields [124].

The thermal quench prior to a major disruption is also analyzed. In most locked mode induced thermal quenches, after the $T_{e,q2}$ collapse, the temperature also collapses in the core, on a timescale much shorter than a diffusive timescale, suggesting destabilization of some core mode. Finally, a class of locked-mode-induced minor disruption in which the tearing mode is fully stabilized is presented and discussed. Minor disruptions are characterized by a thermal quench that affects the entire radial electron temperature profile, but are not followed by a current quench.

The chapter is organized as follows. In section 4.2, methods for mapping magnetics to rational surfaces and accounting for wall eddy currents are presented. Section 4.3 reports observations of $T_{e,q2}$ collapses. Section 4.4 presents resistive MHD simulations of a $T_{e,q2}$ collapse using the NIMROD code. Section 4.5 reports observations of a major disruption. In section 4.6, an example of a self-stabilizing locked mode is shown. Appendix F explains why one island, many non-overlapping islands, or any non-resonant perturbation are not probable explanations of the $T_{e,q2}$ collapse.

4.2 Methods

4.2.1 Mapping of measured fields to rational surfaces

The quantity of interest here is the strength of a given perturbed field *at the rational surface* where it is sourced, because the square-root of that field-strength is proportional to the island-width [50]. To infer this value from measurements taken *at the wall* (tens of centimeters away), the radial tearing eigenfunctions must be estimated.

In the circular cylinder, infinite aspect ratio, vacuum approximation, the tearing field falls off outside of the rational surface where it is sourced as follows:

$$\frac{B^{m,n}(r)}{B^{m,n}(r^{m,n})} = \left(\frac{r}{r_{m,n}}\right)^{-(m+1)}, \tag{4.1}$$

where $r_{m,n}$ is the minor radius where the safety factor q equals m/n, and $r \geq r_{m,n}$ is the minor radius where the field is evaluated. Note that this is the field produced by the TM only (a compensation for the wall eddy currents will be added in section 4.2.3).

Due to the different $r_{m,n}$ and m, the largest perturbed field at the wall might not be the largest field at the corresponding rational surface. Similarly, the largest resonant field at a rational surface does not necessarily correspond to the largest island. This is due to considerations on the q-profile and poloidal wavelength.

Herein, most magnetics data are presented in terms of island widths and island phases. In one figure, however (Fig. 4-3), the square-root of the perturbed field is plotted instead of the island width. This is because not necessarily islands exist for all the field harmonic shown, hence it is not always appropriate to speak of island width.

4.2.2 Assumption of vacuum eigenfunctions

The tearing eigenfunctions are modified by equilibrium current gradients [64], but vacuum eigenfunctions are assumed here for the field mapping just advocated in section 4.2.1.

Due to the LM, the plasma is in the low-confinement mode, or L-mode (thus there is no edge electron pressure pedestal) during all periods where this mapping is performed. The degraded edge confinement produces a ring of cold, resistive plasma, making current generation less efficient. In constant-current feedback, the plasma control system ramps the central solenoid faster. This produces a stronger current source at the edge, often resulting in a local maximum of the equilibrium current in the edge. Nevertheless, we assume for simplicity that vacuum eigenfunctions are valid for estimating the perturbed field at the 2/1, 3/1, and 4/1 rational surfaces.

The island widths of the 2/1, 3/1, and 4/1 are presented in this work, and are calibrated using the 2/1 width measured from the flattening in the T_e profile. This calibration is expected to partially correct for the vacuum assumption.

The 1/1 and 3/2 rational surfaces are located in regions of significant equilibrium current, and therefore vacuum eigenfunctions are likely not valid. In figures where the 1/1 and 3/2 amplitudes appear, they will be labeled with asterisks to remind the reader that the magnitudes of these harmonics should not be compared with others. Note that this mapping has no effect on their phases, and therefore their phases can, and will, be compared with other harmonics.

4.2.3 Compensation of wall eddy currents

In this work we use the poloidal field Mirnov probes to measure the amplitude and phase of both rotating and locked TMs. To understand the evolution of the mode-width from rotation to locking, it is crucial to properly compensate for the effect of eddy currents in the wall, as this can quite different when the mode rotates or is nearly locked in the laboratory frame.

The simple compensation technique presented here is valid at any TM rotation frequency. This includes the limit of zero rotation frequency, i.e. perfect locking, i.e. no eddy currents (provided that the island does not grow, decay or radially move), hence no compensation. Eddy currents also affect the measured phases, but phases will only be of interest during locking, when eddy currents are mostly negligible.

In the presence of rapidly rotating tearing modes, eddy currents in the wall double

the 3D *poloidal* fields at the inner surface of the wall, cancel them everywhere outside the wall, and cancel the 3D *radial* fields both on the inner surface of the wall and everywhere outside of it. For TMs rotating at frequencies similar to the inverse of the wall time $\tau_w \sim 5$ ms [10], the effect of the eddy currents is more complicated.

As mentioned, we adopt the infinite aspect ratio, circular cylinder approximation. In this approximation, the perturbed flux generated by eddy currents in a thin resistive wall, induced by a rotating TM, and evaluated at the wall is given by [64]

$$\psi_w(r_w) = \Psi \left(\frac{r_w}{r_{s+}}\right)^{-m} \frac{i(\omega\tau_w)\left[1-(r_{s+}/r_w)^{2m}\right]}{1-i(\omega\tau_w)\left[1-(r_{s+}/r_w)^{2m}\right]}. \tag{4.2}$$

Here r_w is the minor radius of the wall, $r_{s+} = r_s + w/2$ is the minor radius of the rational surface r_s plus the island half-width $w/2$, m and ω are the poloidal harmonic and poloidal angular frequency of the TM, and τ_w is the resistive diffusion timescale of the wall.

The reconnected flux at the rational surface is given by $\Psi = \psi(r)\exp[i(m\theta - nz/R)]$, where z is the coordinate parallel to the cylinder axis, and R is the major radius of the modeled toroidal plasma.

For rational surfaces located outside of the majority of the equilibrium plasma current, the perturbed flux function of a tearing mode mapped to the wall is given by [64]

$$\psi_{mode}(r_w) \approx \Psi \left(\frac{r_w}{r_{s+}}\right)^{-m}. \tag{4.3}$$

The total perturbed flux measured by a sensor fixed to the inner-wall-surface (not to be confused with the high-field-side wall) is the superposition of the flux ψ_{mode} generated by the TM, which is the quantity of interest in this chapter, and the flux ψ_w generated by the wall, which will have to be subtracted.

The radial and poloidal field at the inner-surface of the outboard-side wall are the components of $\tilde{\mathbf{B}} = \nabla \times \Psi \hat{z}$:

$$\begin{aligned}\delta B_r^{meas} &= \tfrac{im}{r_w}\left[\psi_{mode}(r_w) + \psi_w(r_w)\right] \\ \delta B_p^{meas} &= -\tfrac{m}{r_w}\left[\psi_{mode}(r_w) - \psi_w(r_w)\right]\end{aligned} \tag{4.4}$$

The magnitudes of these complex components can be evaluated using equations 4.2 and 4.3:

$$\begin{aligned}\|\delta B_r^{meas}\| &= \tfrac{m|\Psi|}{r_w}\left(\tfrac{r_w}{r_{s+}}\right)^{-m}\left[1-\Phi(\omega)\right]^{1/2}, \\ \|\delta B_p^{meas}\| &= \tfrac{m|\Psi|}{r_w}\left(\tfrac{r_w}{r_{s+}}\right)^{-m}\left[1+3\Phi(\omega)\right]^{1/2},\end{aligned} \tag{4.5}$$

where

$$\Phi(\omega) = \frac{(\omega\tau_w)^2[1-(r_{s+}/r_w)^{2m}]^2}{1+(\omega\tau_w)^2[1-(r_{s+}/r_w)^{2m}]^2}. \tag{4.6}$$

Equations 4.5 show the expected suppression of δB_r^{meas} and amplification of δB_p^{meas} (recall that the measured quantities here are evaluated on the *inner-side* of the wall).

Forming a linear combination of the squared magnitudes of the fields in equation 4.5, it is possible to remove $\Phi(\omega)$, and thereby the effect of the wall. The correct linear combination is:

$$\begin{aligned}3\left(\delta B_r^{meas}\right)^2 + \left(\delta B_p^{meas}\right)^2 &= 4\left(\tfrac{m\psi}{r_w}\right)\left(\tfrac{r_w}{r_{s+}}\right)^{-2m} \\ &= 4\left[\delta B_p^{mode}(r_w)\right]^2.\end{aligned} \tag{4.7}$$

where the latter equality follows from multiplying equation 4.3 by $\hat{z}$ and taking the curl. Finally, solving for the poloidal field of the mode, we conclude that

$$\|\delta B_p^{mode}(r_w)\| = \gamma\|\delta B_p^{meas}\|, \tag{4.8}$$

where the factor

$$\gamma = \frac{1}{2}\sqrt{1+3\left(\frac{\|\delta B_r^{meas}\|}{\|\delta B_p^{meas}\|}\right)^2} \tag{4.9}$$

accounts for the effect of the eddy currents at the wall. Note that the right hand side of equation 4.8 only contains measured quantities.

4.2.4 Compensating for saddle loop spatial averaging

A significant number of magnetic sensors were added during a recent "3D upgrade" at DIII-D [32]. This has enabled the multi-harmonic LM analysis presented here. The techniques used to extract the 3D fields of LMs on the order of 10^{-4} of the equilibrium field are reported in reference [33].

A toroidal array of six saddle-loops external to the vessel and located on the outboard midplane is used here to measure the radial fields. The saddle loop signals are differenced to remove equilibrium fields, and a combination of hardware and software compensation removes DC coupling of small non-axisymmetric fields produced by nominally axisymmetric and 3D control coils.

The external saddle loops span ~ 1.1 m in the poloidal direction, and ~ 2.6 m in the toroidal direction. In the large aspect ratio, circular cross-section approximation, taking the saddle loops to span $\sim 90^\circ$ in the poloidal direction (note the actual span is closer to 72°), the attenuation factor $\alpha^{m,n}$ of measured harmonic m/n due to spatial averaging can be approximated as follows:

$$\alpha^{m,n} = \left[1 - \frac{6}{\pi^2}\int_{-\pi/6}^{\pi/6}\int_{-\pi/4}^{\pi/4}\cos(m\theta - n\phi)d\theta d\phi\right]. \tag{4.10}$$

Quantifying the errors in this cylindrical model would require a comparison with synthetic diagnostics in a 3D MHD simulation, and is beyond the scope of this analysis. Instead, errors are assumed to be on the order of $\pm 10\%$. The poloidal spectrum of the measured $n = 1$ field is plotted in figure 4-1, for $m < 7$.

The poloidal fields are measured using Mirnov probes covering the outboard and inboard walls. These probes have a negligible poloidal extent relative to the $m \leq 5$ poloidal wavelengths of interest.

For the eddy current compensation technique presented in section 4.2.3, we assume that the poloidal spectrum of the $n = 1$ field measured by the saddle loops is

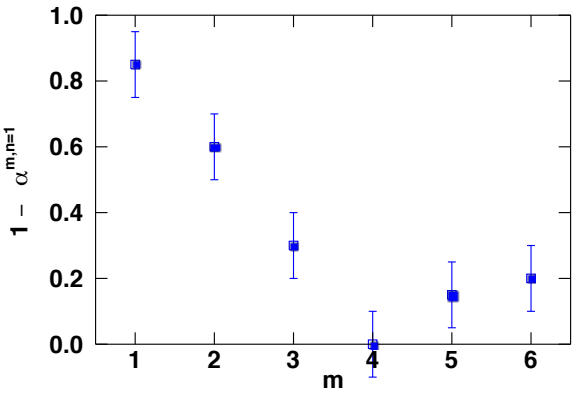

Figure 4-1: Poloidal spectrum of $n = 1$ field amplitude measured by the external saddle loops, normalized to the corresponding m,n peak-amplitude at the detector. Less than 0.15 ± 0.10 of each field with $m > 7$ is measured (not shown).

dominated by the $m = 2$ mode. Therefore, prior to taking the ratio of the $n = 1$ radial and poloidal fields to calculate γ (equation 4.9), the $n = 1$ Fourier amplitude measured by the saddle loops is multiplied by $1/(1 - \alpha^{2,1}) \approx 1.7$.

4.3 $T_{e,q2}$ collapse

The $T_{e,q2}$ collapse is characterized by a large region of reduced electron temperature gradient extending from the plasma separatrix to around the $q = 3/2$ surface. This is distinct from the *non-axisymmetric* T_e flattening due to the 2/1 island as it affects a region 2-3 times wider, and measurements are consistent with axisymmetry.

The Thomson Scattering (TS) and ECE diagnostics in DIII-D [36] are used together to measure the electron temperature radial profile along two different view chords; one vertical, one horizontal, and at different toroidal locations (Fig. 4-2). In particular, the sign of the field helicity and the radial location of the $q = 2$ surface in the discharges presented here are such that while one diagnostic views the 2/1 island O-point, the other views a region near the X-point (this will be confirmed by simulations in Fig. 4-7).

A $T_{e,q2}$ collapse begins without any change in core T_e where $q \sim 1$, and can heal without any response from the core. In other cases, the core T_e partially degrades, but on a much longer timescale than the edge collapse.

An example of $T_{e,q2}$ collapse will be shown in figures 4-3-4-4. The discharge (154576) was part of an experiment to measure the effects of collisionality on pedestal properties using neon seeding [134]. The discharge operated with a slightly elevated minimum safety factor $q_{min} \approx 1.1$, and an edge safety factor of $q_{95} \approx 4.1$. Immediately prior to the onset of a rotating $m/n = 2/1$ TM, the normalized plasma beta β_N transiently reached 3. This was achieved using a neutral beam power of ~ 7 MW, and with a neutral beam torque of ~ 6 Nm. The line-averaged electron density at the onset of the TM is $n_e \approx 8 \times 10^{19}$ m^3. After the 2/1 TM locks, the electron density and normalized beta continuously reduce over the 130 ms before the $T_{e,q2}$ collapse shown in figure 4-3 to $n_e = 3 \times 10^{19}$ m^3 and $\beta_N = 0.8$.

4.3.1 Profile measurements

Figure 4-3a presents TS and ECE measurements of the electron temperature profile before (blue), during (orange) and after (red) a $T_{e,q2}$ collapse. TS density data (not

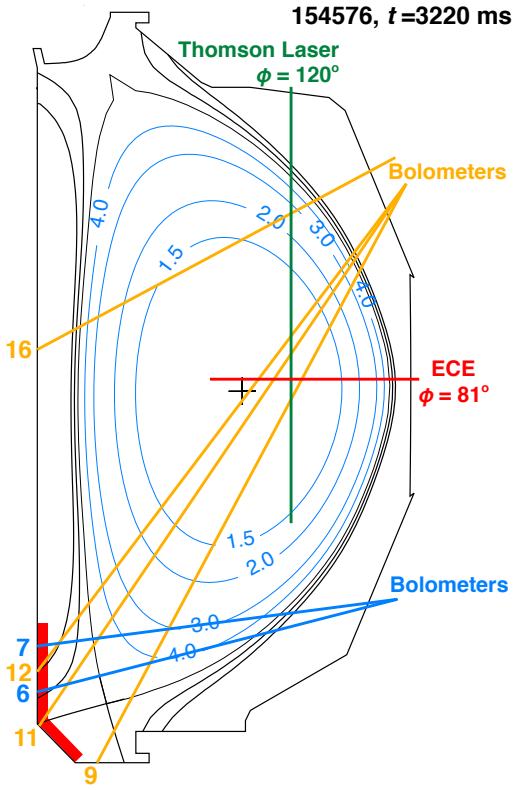

Figure 4-2: EFIT [12] equilibrium reconstruction for discharge 154576 at $t = 3220$ ms, constrained by magnetics and Motional Stark Effect data. Some rational flux surfaces are shown in light blue, and the + marks the magnetic axis. The plasma separatrix and two scrape off layer poloidal flux contours are shown in black. Also shown are the lines of sight for: selected channels of the upper (yellow) and lower (blue) bolometer (used in section 4.3.5), electron cyclotron emission (ECE, red) and Thomson Scattering laser (green). Note that the ECE and Thomson Scattering are located at different toroidal locations ϕ. The inner divertor region viewed by the IR camera (used in Fig. 4-6) is highlighted in red.

shown), and the fact that ECE temperatures are finite and in approximate agreement with TS, confirm that the plasma is not overdense (i.e., ECE is not cutoff) and that it is optically thick. Hence, the ECE temperature measurements are reliable.

According to ECE, which is more highly time-resolved than TS, the $T_{e,q2}$ collapse begins at ~ 3214 ms. However, for comparison, ECE profiles are only plotted at times at which the TS laser is fired and thus TS profiles are available. The time-interval interested by the $T_{e,q2}$ collapse is clearly marked in figures 4-3b-c, along with vertical solid lines marking the TS laser-pulses.

A flattening is noticeable in the TS profiles at the $q = 2$ location at all times

considered. This is indicative of a 2/1 island of finite amplitude (figure 4-3b, black) that we know, from magnetic measurements, to be locked (figure 4-3c, black). From magnetics we also know that the island is locked with such a toroidal phase (figure 4-3c, black) that the TS diagnostic is observing the island O-point, whereas the ECE is observing the X-point. This is due to the distinct locations and view-chords of these diagnostics (figure 4-2), and explains why there is no flattening in the ECE profiles in figure 4-3, before and after the collapse. There is however flattening during the collapse (orange), both in the TS and ECE profiles. Such flattening is not restricted to the $q = 2$ location. Rather, it extends to both outer radii (at least to the $q = 3$ or $q = 4$ locations, and possibly to the plasma separatrix S) and inner radii ($q = 3/2$ location). Also note that the same flattening is observed at the drastically different poloidal and toroidal locations of the TS and ECE diagnostics.

An axisymmetric collapse is the simplest and most likely explanation of this observation. It is argued in Appendix F that non-axisymmetric interpretations are either not consistent with the magnetics data, or require large parallel T_e gradients, and thus, are unlikely.

The cause of this axisymmetric collapse could be island overlap and consequent field stochastization. Note that a significant amount of overlap is required to fully stochastize the broad region under consideration. This interpretation is supported by theoretical arguments in [124] and by simulations to be presented later, in figure 4-8.

The expectation from figures 4-3b-c is that the 2/1 island is present throughout the collapse, and that its amplitude and phase remain approximately constant. The blue and red profiles in figure 4-3a are consistent with this expectation. The orange profile is also consistent, but a richer physics is taking place, besides the presence of the 2/1 island. Here by richer physics we mean complex MHD at various m and n (figure 4-3b-c) and a complex T_e evolution over a broad range of radii that encompasses the corresponding $q = m/n$ locations (figure 4-3a).

The single orange TS data point between the $q = 1.5$ and $q = 2$ locations is a slight outlier, within the error bar, relative to the orange ECE profile. In fact, it seems more consistent with the blue and red TS points (before and after the collapse)

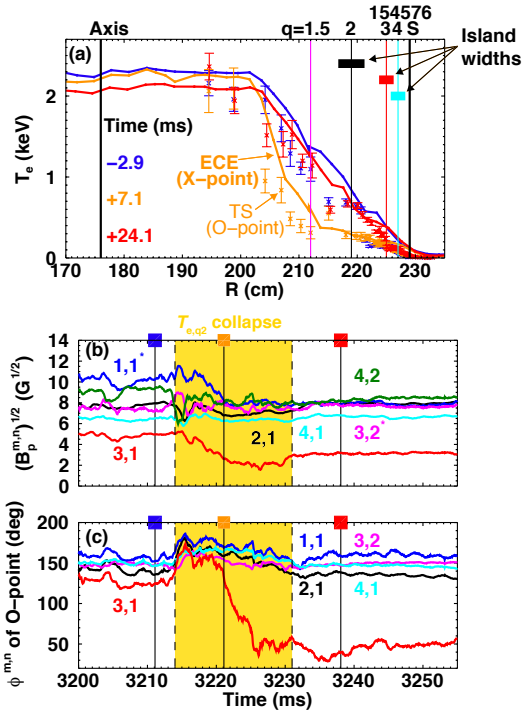

Figure 4-3: (a) Electron cyclotron emission (ECE, solid curves) and Thomson Scattering (TS, symbols with error-bars) electron temperature profiles shown at the beginning (blue), middle (orange), and recovery (red) of a "$T_{e,q2}$ collapse". Times are relative to $t_0 = 3214$ ms. Vertical lines show locations of rational surfaces, the magnetic axis, and the separatrix (S), and vary by only ± 1 cm during this time interval. The horizontal black bars centered about the $q = 2$, 3, and 4 surfaces are approximate island widths before the $T_{e,q2}$ collapse, measured magnetically and calibrated with the flattening in the TS T_e profile. (b) Square-root of the perturbed fields mapped to their respective rational surfaces as a function of time. Vertical lines with colored symbols mark the times of the profiles in (a). The asterisks on the 1/1 and 3/2 field labels remind that these fields should not be compared with others (see section 4.2.1).

at the same radial location. It is possible that temperature gradients across some fraction of the nested surfaces in the island are sustained during the collapse. In the simulations to be presented in figure 4-8, 3/1 and 4/1 islands are still present despite stochastization of their separatrices. This might explain why T_e is not perfectly flat during the $T_{e,q2}$ collapse in figure 4-3a. Similar observations were made during other $T_{e,q2}$ collapses.

As for T_e in the core, this is remarkably flat, within error, over a broad range of radii. Measurements are shown in Fig. 4-3a, and are reminiscent of earlier simulations of LM disruptions in Ohmically heated plasmas [119, 120]. In those simulations the

current-density profile was flat in the core, due to the requirement that $q_{min} \geq 1$ for stability of the internal kink. As a result, the simulated T_e profiles were also flat in the core. This is due to the T_e profile being related to the current profile, in Ohmic plasmas. It should be clarified that discharge 154576 was not Ohmic, but heated with neutral beams, hence it is not obvious that the T_e profile should resemble the current profile. Yet the experimental current density profile (not shown) resembles those in the simulations [119, 120]. Core confinement in the vicinity of the $q = 1$ surface is not studied here, and remains an interesting open question for future work.

The profile ~ 24 ms after the onset of the collapse shows a reduction in core T_e of 200-300 eV. This T_e decay progresses in a continuous manner (as will be shown in figure 4-4a), unlike the transient edge collapse. The relatively slow evolution of the core is not studied here.

This locked 2/1 mode does not spin up or decay, and is present during the final disruption ~ 30 ms after the last time-slice of figure 4-3a. By spin-up here we mean attainment of a rotation frequency well above the inverse wall time. Section 4.5 will examine the T_e profile evolution during a disruption, and will show that it begins with a $T_{e,q2}$ collapse similar to the one presented in this section, with the notable exception that the edge temperature does not recover.

As mentioned in the introduction, $T_{e,q2}$ collapses are also observed in non-disruptive discharges. The $T_{e,q2}$ collapse may be a common onset of LM disruptions, though it alone is not a sufficient condition for a disruption: the requisite thermal collapse in the core, and the requisite current quench, may or may not follow the $T_{e,q2}$ collapse.

4.3.2 Relationship between locked mode amplitudes

Figures 4-3b-c showed the coexistence of several fields of different m and n of finite amplitude (Fig. 4-3b) and approximately constant phase (Fig. 4-3c), i.e., locked. An examination of their time evolution in figures 4-3b-c suggests that some of these fields are correlated (coupled) with each other, whereas others evolve in an uncorrelated, independent manner. Table 4.1 summarizes the correlations in time of the various m/n components.

	2/1	**3/1**	**4/1**	**3/2**
1/1	0.1	**0.7**	0.0	0.1
2/1		-0.2	**0.9**	**0.6**
3/1			**-0.4**	-0.3
4/1				**0.7**

Table 4.1: Correlations of the time-dependent mode amplitudes for each harmonic pair. Correlations evaluated between 3100 and 3300 ms. The five highest correlations (i.e. largest absolute value) are bolded.

Flattened regions appear in the TS profiles at the $q = 2$, 3, and 4 surfaces, consistent with $m = 2$, 3, and 4 islands, before and during the collapse (Fig. 4-3a). Upon recovery of the temperature profile (red), a flattening is observed at the $q = 2$ and 4 surfaces in the TS profile, while a gradient appears across the $q = 3$ surface. The latter is consistent with the reduction in the 3/1 perturbed field (Fig. 4-3b), and the change in the 3/1 phase (Fig. 4-3c). The square-root of the 3/1 field upon recovery (red profile) is reduced by $\sim 40\%$ relative to its value prior to the collapse (blue profile), implying a 40% reduction in the island size. Further, the phase changes by $\sim 90°$. This brings the island O-point closer to the ECE view chord than the TS view chord. An inflection point appears in the recovered T_e profile as measured by ECE, though this is not sufficient to conclude the presence of a small 3/1 island.

The 2/1 and 4/1 amplitudes are highly correlated, as shown in table 4.1. The phases also appear nearly locked (Fig. 4-3c), though some independent variation can be observed. It is possible that their amplitudes are coupled through the 2/0 ellipticity [113], and their phases locked by electromagnetic torques.

4.3.3 Inter-island phase relationship as a $T_{e,q2}$ onset indicator (when combined with sufficient values of the Chirikov parameter)

The phase relationship of the locked islands shows unique behavior coincident with the onset of the $T_{e,q2}$ collapse in discharge 154576. For this study, the full time over which the $n = 1$ islands are locked is considered ($t = 3085$ ms to disruption, Fig. 4-4).

During this time interval, there are at least three $T_{e,q2}$ collapses, where the last one is followed by a core collapse and current quench. The ECE channels are cutoff due to high density during the first $\sim$ 50 ms after locking, which occurs at $\sim$ 3085 ms. For this reason, those $\sim$ 50 ms of data are omitted from figure 4-4a.

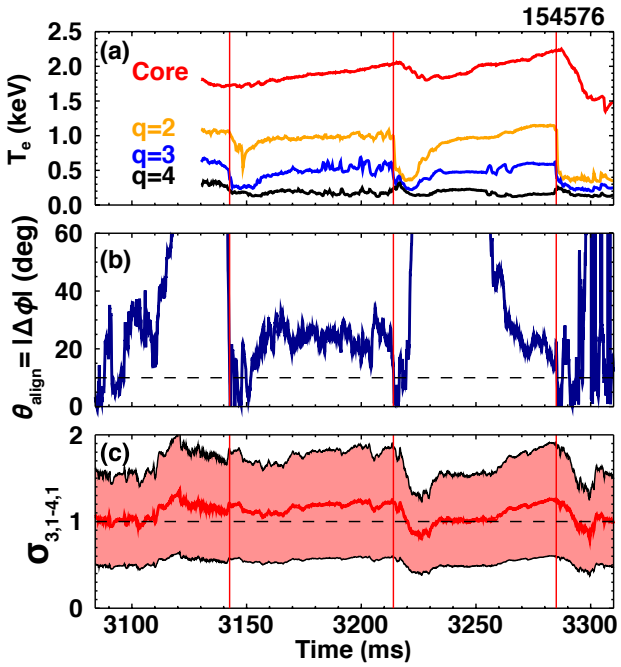

Figure 4-4: (a) Electron temperature at the core, and the 2/1, 3/1, and 4/1 island locations as measured by ECE. (b) Time trace of the toroidal phase difference between the 4/1 and 3/1 island O-points on the outboard midplane as measured by magnetics. Vertical lines indicate the approximate onset times of $T_{e,q2}$ collapses. The dashed horizontal line marks the approximate $T_{e,q2}$ collapse onset threshold of 10°. (c) The Chirikov parameter for the 3/1 and 4/1 islands (red), with error margin shown by the shaded region between the black curves. The dashed horizontal indicates where the sum of the island half-widths is equal to the distance between the $q = 3$ and 4 surfaces.

Let us consider the O-points of two $n = 1$ TMs whose poloidal mode numbers differ by $|\Delta m| = 1$ (e.g. $m = 3$ and $m = 4$). It can be shown that these O-points can only exist on the same radial chord in a single poloidal and toroidal location. We refer to this unique angular coordinates as Θ_{align} and Φ_{align}.

We define the toroidal position of a given tearing mode as the toroidal angle where its O-point reaches the outboard midplane. This location is also unique, for an $n = 1$ TM. We then introduce the difference $\Delta\phi$ between the toroidal positions (as just

defined) of two $n = 1$ TMs. It can be shown that

$$\theta_{align} = |\Delta\phi|. \tag{4.11}$$

where $\theta_{align} = |\Theta_{align}|$, and is defined on the domain $[0, \pi]$. This definition of θ_{align} cannot differentiate between alignment at some θ_{align} above the midplane and the corresponding $-\theta_{align}$ below the midplane. However, no observations have been made to suggest that the interaction between TMs above and below the midplane are different. Thus, this definition of θ_{align} is sufficient for the studies herein. This simple relationship will allow us to investigate θ_{align} by measuring $|\Delta\phi|$ for two $n = 1$ TMs with $|\Delta m| = 1$. Figure 4-4b shows θ_{align} for the 3/1 and 4/1 islands as a function of time. When this phase-difference vanishes, the two O-points are aligned on the outboard midplane, at some toroidal location.

In figure 4-4b, θ_{align} drops below 10° (dashed line) near the time of the three known $T_{e,q2}$ collapses (vertical lines). Said otherwise, the O-points align with each other at a particular poloidal position coincident or nearly coincident with the outboard midplane (within 10° from it). The first of such alignment events occurs at the same time as the $T_{e,q2}$ collapse. The second and third event occur ~ 1 ms *after* the corresponding collapses. At first sight this might suggest that island-alignment is an effect of the collapse, and not the cause. However, it should be noted that the $n = 1$ wall time in DIII-D is ~ 3 ms. Consequently, sudden phase-changes (faster than ~ 3 ms) are detected with some delay. On the other hand, ECE measurements do not suffer from any delay. Therefore, the data are consistent with the hypothesis that O-point alignment within 10° of the outboard midplane triggers the collapse.

Shown in figure 4-4a is T_e at various locations as a function of time. During the first marked $T_{e,q2}$ collapse, the T_e gradient collapses first between the $q = 3$ and $q = 4$ locations, followed by a transient collapse between $q = 2$ and $q = 3$. This suggests that the $T_{e,q2}$ collapse, at least in this case, begins in the region outside of the $q = 3$ surface and travels inward.

The Chirikov parameter for the 3/1 and 4/1 islands is formulated as follows:

$$\sigma_{3,1-4,1} = \frac{1}{2}\frac{w_{3,1} + w_{4,1}}{r_{q4} - r_{q3}}, \tag{4.12}$$

where r_{q4} and r_{q3} are the minor radii of the $q = 4$ and 3 surfaces. When this parameter exceeds 1, the island separatrices overlap, which is known to generate stochastic fields [124]. Indeed this parameter, plotted in figure 4-4c, often equals or exceeds 1, suggesting island overlap. However, the electron temperature at the $q = 3$ surface is observed to collapse only transiently, and recovering to temperatures of ~ 500 eV, even at times when $\sigma_{3,1-4,1} > 1$. Note however the large uncertainty on the Chirikov parameter (shown by the red shaded region in figure 4-4c. This large error is the result of propagating errors in the island widths and island locations according to equation 4.12.

The apparent onset when the 3/1 and 4/1 O-points align at the outboard midplane (Fig. 4-4b) might suggest that in toroidal, shaped plasmas, the critical condition for loss of confinement between two islands depends on the poloidal angle at which O-points align. If the onset is due, for instance, to the distance between island separatrices in real space, perhaps as a result of the finite ion Larmor radius, then for fixed island widths, the distance is minimized when the O-points are on the inboard or outboard midplanes, due to flux compression resulting from ellipticity. On the outboard midplane, the Shafranov shift and ion banana orbits might also play a role in setting the critical distance between O-points, above which confinement is lost in the region between two islands.

In conclusion, all the rest being equal (island widths and radial locations), it is plausible that different poloidal phasings cause more or less stochastization. In particular, flux compression on the outer midplane can favor field stochastization, even in cases in which the Chirikov parameter is marginal ($\sigma \approx 1$ instead of $\sigma > 1$),

Cylindrical simulations found that O-point alignment at some toroidal angle is a consistent feature of disruptions caused by multiple magnetic islands [135]. Experiments on the TFR tokamak [136] revealed that the $m/n = 2/1$ O-point aligns with another O-point at the outboard midplane. The latter had $m = 1$ and unspecified n,

and was located near the $q = 1$ surface.

4.3.4 $T_{e,q2}$ collapse coincident with critical island widths

In a different discharge, the Chirikov parameter, formulated now for the 2/1 and 3/1 islands, approaches and often exceeds 1 (figure 4-5d) about 5 ms before each $T_{e,q2}$ collapse (figure 4-5b). This happens in four out of the five collapses. At about the same times, the O-points approach alignment, but at the *inboard* midplane ($\theta_{align} \approx 180°$ in figure 4-5c, as opposed to $\theta_{align} \approx 0°$ in figure 4-4b). Few milliseconds afterwards, however, $\theta_{align} \to 0°$ in figure 4-5c, implying O-point alignment on the outboard side. The causes for the different behaviors of θ_{align} in figures 4-4b and 4-5c are not well understood. Differences in the evolution of θ_{align} are also noticeable in the first three collapses in 4-5c (marked by thin vertical lines), compared with the last two (marked by thick lines). The causes are unknown, but they might be related to the fact that, unlike the first three collapses, the last two extend as far in as to the $q = 3/2$ location (as implied by the time-trace for T_e at the $q = 3/2$ location, in green in figure 4-5b). This is suggestive of a large 3/2 island overlapping with a neighbouring island. The presence of a large 3/2 island might affect how the phases of the other modes (mostly of $n = 1$) evolve.

Prior to the collapse, the temperature between the $q = 2$ and $q = 3$ locations is degraded. This is visible both in the black time-trace in figure 4-5b and in the blue profile in figure 4-5a. About 2 ms later, the collapsed T_e gradient extends as far in as to the $q = 3/2$ surface (orange profile), and is observed by both TS and ECE. This discharge has the same helicity sign and similar $q = 2$ radius to the discharge discussed before, where the 2/1 O- and X-point roughly align with the TS view and ECE view, respectively (Fig. 4-7). Therefore, a similar diagnostic spacing relative to the 2/1 island is expected here.

The 2/1 and 3/1 island half-widths are comparable with the distance between the $q = 2$ and $q = 3$ surfaces immediately before the last $T_{e,q2}$ collapse, shown by the horizontal bars in figure 4-5a. Island asymmetries are not considered here, and might affect the distance between these island separatrices. Within 17 ms of the onset of

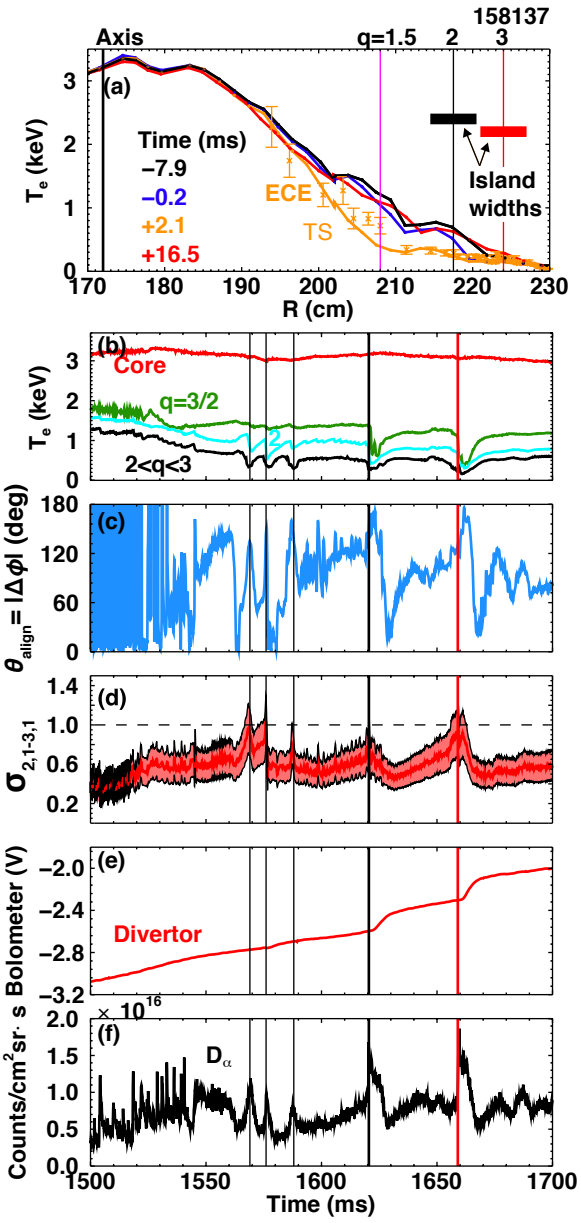

Figure 4-5: (a) T_e as a function of the major radius at times relative to the $T_{e,q2}$ collapse at $t = 1659$ ms. Vertical lines show rational surfaces and the magnetic axis. Horizontal bars show the 2/1 and 3/1 island widths prior to the collapse. (b) T_e measured by ECE as a function of time. Different types of $T_{e,q2}$ collapses that extend or not to the $q = 3/2$ location are marked by thin and thick vertical lines respectively. The profiles in (a) are measured shortly before, during and after the collapse marked in thick red. (c) Absolute value of the toroidal phase difference between the 3/1 and 2/1 O-points on the outboard midplane. (d) Half-widths of the 2/1 and 3/1 islands, and their sum. The estimated distance between the $q = 2$ and 3 surfaces is shown by the solid line, with lower error shown by the dashed line. (e) Bolometer signal from channel 6 which intersects the inner divertor leg. (f) Filterscope measurement of lower divertor D_α light intensity.

the $T_{e,q2}$ collapse, the edge T_e recovers, as shown by the red profile. Note that the core region between the axis and $R \approx 190$ cm is not affected by this $T_{e,q2}$ collapse. An axisymmetric collapse that occurs at a critical value of $(w^{3,1} + w^{2,1})/2$ and starts with a perturbation in T_e between the $q = 2$ and $q = 3$ surfaces is consistent with stochastic transport due to overlap of the 3/1 and 2/1 islands.

4.3.5 Energy losses during the $T_{e,q2}$ collapse

The primary goal of this section is to determine if the energy lost during a $T_{e,q2}$ collapse is consistent with a transport of heat and particles to the scrape off layer, or with a radiation imbalance. We investigate the last $T_{e,q2}$ collapse in figure 4-5. At the time of the collapse, the plasma electron density is $n_e \approx 2 \times 10^{19}$ m^{-3}, well below the Greenwald density limit [122] of $n_G = 1.3 \times 10^{20}$ m^{-3}. Therefore, a global radiation imbalance would not be expected. However, a sufficient influx of impurities could increase the radiated power in the edge and cause the collapse. Therefore a radiation imbalance, possibly combined with other mechanisms, is not ruled out.

The peak heat-flux to the inner-divertor leg during the $T_{e,q2}$ collapse increases transiently as shown in figure 4-6a. Figure 4-6b shows that the spatial distribution of this transient heat-flux is peaked.

After integrating over this spatial distribution and integrating in time throughout the duration of the collapse, we find that 20 ± 5 kJ have been deposited on the inner-divertor leg. The outer-divertor leg is not imaged by the infrared camera, and therefore the energy deposited in that region cannot be estimated.

The lower poloidal array of bolometers [137] measures the power radiated along the chords illustrated in Fig. 4-2. During and after a collapse, the only significant changes in radiated power are measured by channel 6 and 7. These channels view the inner divertor region. In fact, their view chords intersect the region of increased divertor heat flux (see blue shaded rectangles in figure 4-6b), and collect $\sim 95\%$ of the energy radiated during this time interval.

The raw voltage signal from channel 6 is plotted in figure 4-5e. It exhibits a latent response over ~ 15 ms following the two major $T_{e,q2}$ collapses. This is consistent with

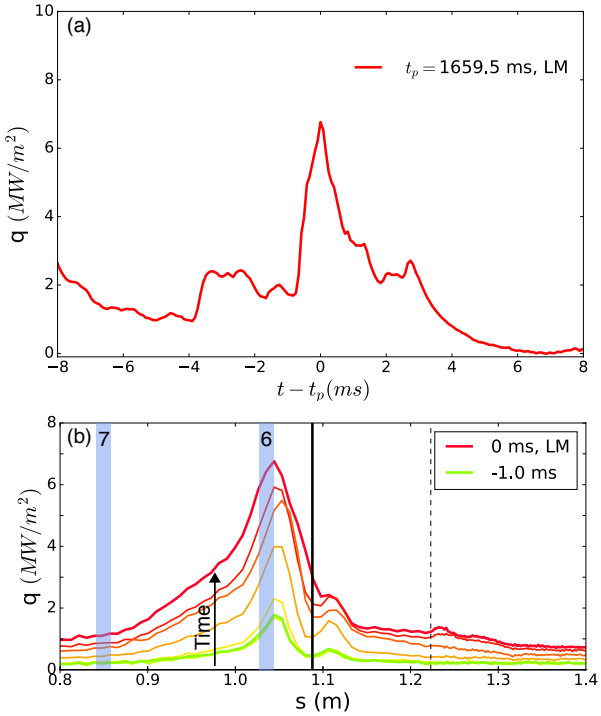

Figure 4-6: (a) Peak heat flux on the inner-divertor leg as a function of time as measured by an infrared camera during a $T_{e,q2}$ collapse. The time is relative to the time t_p at which the heat flux peaks, reported in the legend, and is approximately equal to the onset time of the last collapse in Fig. 4-5. (b) Spatial distribution of heat flux on the inner-divertor leg, measured by the infrared camera, at times preceding and including the peak shown in (a). Profiles are taken at different times with 0.17 ms time-step. Blue shaded regions show the locations of lower array bolometer channels 6 and 7. The solid vertical line shows the location of the strike point, as estimated by equilibrium reconstructions.

the response to short-lived radiation events, shorter or much shorter than $\sim$ 15 ms, and thus effectively similar to delta-functions of time.

Integrating the change in radiated power in channels 6-8 from the onset of the last $T_{e,q2}$ collapse to 15 ms post-collapse, and assuming toroidal invariance of the radiation source, we find 24 ± 5 kJ of radiated energy. Channels 11 and 12 of the upper fan array view the same region of the inner wall (Fig. 4-2), and provide a redundant measurement of the radiated energy from this area. Using the upper array, the radiated energy is estimated at 22 ± 5 kJ, in agreement with the lower array.

A full energy accounting would also require considering energy sources such as the injected neutral beam power and Ohmic heating. The missing heat flux measurements

on the outer-divertor preclude a full energy accounting. In total, 44 ± 7 kJ of energy are conducted and convected to the divertor and radiated. The energy incident on the outer-divertor leg was not measured, and is expected to increase this total. Some double-counting of radiated energy is expected due to radiant heating of the inner-divertor leg. We conclude that the majority of the lost energy appears in the divertor region, in the form of heat on the inner-divertor surface and in the form of radiation from a source located near the inner-divertor; the magnitude of the heat flux on the outer-divertor is unknown.

The increased heat flux to the inner-divertor, the transient increases in D_α line radiation in figure 4-5f, and the localized radiation in the divertor region are all consistent with a transport of particles and energy to the divertor. Stochastic transport resulting from overlap of edge island chains is a candidate explanation. Radiation localized at inboard side of the plasma, referred to as a MARFE [138], has been observed during the early stages of density limit disruptions. However, MARFE radiation becomes isotropic once the T_e profile starts to contract [71]. Instead, here we observe the radiation to be localized on the inner divertor throughout the collapse, and to peak at a specific location (figure 4-6).

The present results neither validate nor invalidate recent theoretical work [121] attributing density-limit disruptions to an excess of radiative losses by the island relative to the Ohmic heating of the island, leading to exponential growth. First, the plasma densities in the discharges presented here are all below the Greenwald limit [122]. Moreover, we have made no observations pertaining to the source of the island growth, but rather to the critical amplitude and phase conditions resulting from the presence of *multiple* macroscopic islands. Specifically, we have not estimated the Ohmic power deposited in the islands, which is left as future work.

4.4 Simulations of a $T_{e,q2}$ collapse

The NIMROD [128] code is a three dimensional, nonlinear resistive MHD solver used for initial value problems. Here we use the single fluid model to time evolve a plasma equilibrium reconstructed by EFIT [12] 4 ms prior to a $T_{e,q2}$ collapse. In particular, this is the second collapse in figure 4-3.

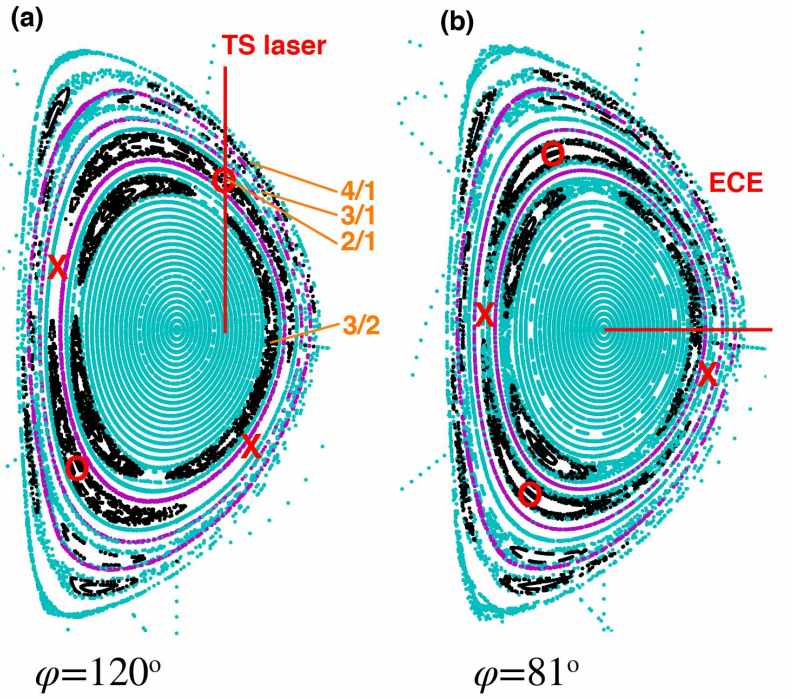

Figure 4-7: Poincaré plots showing initialization of NIMROD simulation of discharge 154576 at $t = 3210$ ms at the toroidal locations of the ECE and TS diagnostics. Island alignment is chosen to match $t = 3215$ ms from the experiment when X-points of $n = 1$ islands are aligned with each other at the outboard midplane. (a) The TS laser (vertical red) is shown intersecting the 2/1 island O-point, marked by the red "O". (b) The ECE view chord (red) is shown viewing the 2/1 island X-point, marked by the red "X". The mutual alignment of $n = 1$ X-points and a 3/2 O-point in this poloidal cross-section implies that all $n = 1$, and a second 3/2 O-point are mutually aligned at the outboard midplane in the poloidal cross-section 180° away toroidally.

Macroscopic 3/2, 2/1, 3/1, and 4/1 islands are initialized (Fig. 4-7 and 4-8a), approximately matching the experimental islands sizes. Close matching was deemed unnecessary, as the nonlinear solver is expected to relax the island-widths to self-consistent saturated values anyway. The phase-relationship of the initialized islands

matches measurements at the onset time of the collapse, $\sim$ 3214 ms, when O-points are aligned on the outboard midplane.

In all three simulations, the perpendicular and parallel diffusion coefficients are set to $\chi_\perp = 0.1$ m/s and $\chi_\parallel = 10^8$ m/s. The $\chi_\perp$ value is chosen to match expected experimental conditions, and $\chi_\parallel$ is set as large as is numerically tractable, although realistic $\chi_\parallel$ values can be even higher.

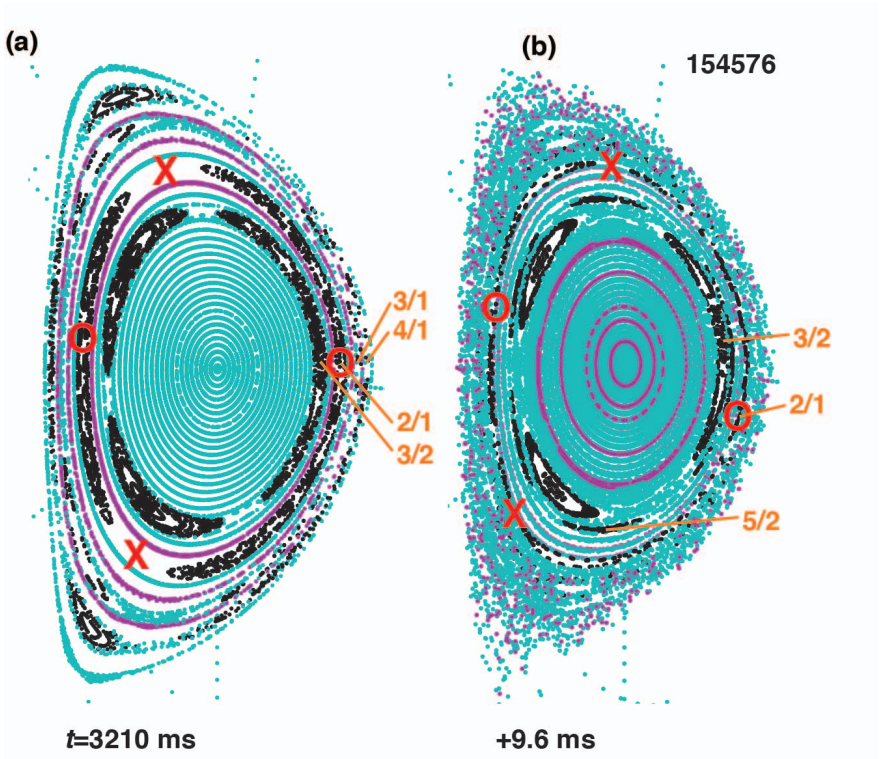

Figure 4-8: Poincaré plots showing NIMROD simulations of the equilibrium and locked mode (LM) conditions in discharge 154576. Islands are traced with black field lines, and other surfaces are traced with turquoise field lines. Magenta field lines are initialized at selected surfaces, and clearly show stochastic fields when they are not confined to a surface. (a) Initial conditions showing 3/2, 2/1, 3/1, and 4/1 O-point alignment on the outboard midplane. This cross-section is separated by 180° toroidally from the initialization shown in Fig. 4-7b. (b) Poincaré plot after evolving both the equilibrium and the MHD modes by 9.6 ms, when an approximate steady state is reached. The fields in the region between the 2/1 island and the plasma separatrix are stochastic, as shown by the random distribution of magenta points.

Figure 4-8 shows Poincaré plots from the highest resistivity case at initialization, and 9.6 ms into the simulation. A significant region of stochastic fields develops. The region of stochasticity appears to extend from the plasma edge inward, reaching the

outer separatrix of the 2/1 island, which is likely the result of the 3/1 and 4/1 islands overlapping. The resilience of the 2/1 island to stochastization is also observed in two other completed simulations with lower resistivities, not shown.

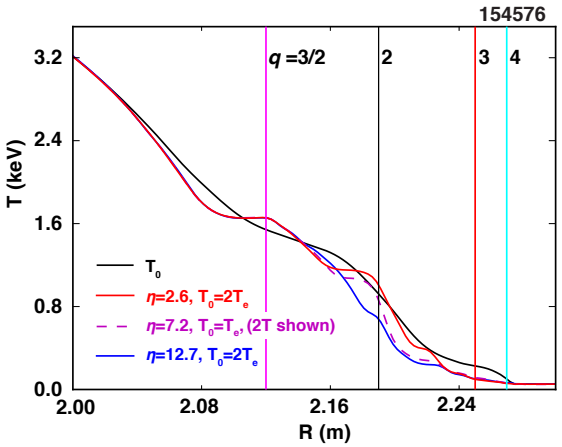

Figure 4-9: Axisymmetric ($n = 0$) temperature profiles for three simulations, for different levels of resistivity, taken at the time where an approximately steady state is reached. The initial fluid temperature T_0 for all simulations is shown in black. This initial temperature is the experimental ion temperature, which is roughly twice the experimental electron temperature for the red and blue traces. The initial density was doubled relative to the experimental value in one case (dashed magenta) in order to reduce the fluid temperature to match the experimental electron temperature profile. Resistivity scales like $\eta \propto T^{-3/2}$. The magnitude of the resistivity differs in each curve. At the point where all curves intersect, the resistivity of each curve is reported in the legend in units of ($\mu_0 10^{-2}$ Ωm).

Across the stochastic region shown in figure 4-8b, the temperature gradient is weak, as seen in figure 4-9 (blue) starting $\sim$ 2 cm outside of the $q = 2$ surface and extending through to the plasma edge. The simulated axisymmetric degradation of T_e is consistent with experiments, in the outer region. However, it does not extend as far inwards as to the $q = 3/2$ location (see Fig. 4-3a for comparison).

The 2/1 island is observed to decay significantly between $t = 0$ and $t = 9.6$ ms (the time-origin here is at the onset of the $T_{e,q2}$ collapse). This is not consistent with $(B_p^{2,1})^{1/2}$ undergoing a 25% oscillation in figure 4-3b, but not decaying significantly. The 3/2 island width does not change considerably in the Poincaré plots, in agreement with the roughly constant $(B_p^{3,2})^{1/2}$. A small 5/3 island also appears in the simulation between the 2/1 and 3/2 locations.

Increasing resistivity appears to degrade the profile more and more, as seen in figure 4-9. The resistivities used correspond to Spitzer resistivities with $Z_{eff} = 4.9$ (blue), $Z_{eff} = 2.8$ (magenta), and $Z_{eff} = 1$ (red). This scan shows that the degradation in T_e increases with increasing resistivity (Fig. 4-9), though the experimentally observed degradation (Fig. 4-3) is even more severe than the most severe simulated degradation, for the highest assumed resistivity.

Note that the profiles in figure 4-9 are axisymmetric ($n = 0$). That is, they are evaluated on the midplane ($\theta = 0$), but not at a specific ϕ. Rather, they are averaged over all ϕ. The flattening of the profiles at the $q = 3$ and $q = 4$ locations is a consequence of the 3/1 and 4/1 island overlap and consequent stochastization reported in figure 4-8b. The finite gradient at the $q = 2$ location is compatible with the 2/1 island not being stochastized in figure 4-8b. The reduction of the 2/1 island size in the simulation might prevent it from becoming stochastic. The larger region over which the collapse is observed in experiment suggests that the 2/1 island might also become stochastic, like the 3/1 and the 4/1 in the simulation.

In the single fluid initialization, NIMROD uses the pressure profile and the electron density to infer the fluid temperature. In the experiment, the ion temperature is approximately twice the electron temperature across the whole radial profile. In one simulated case, the initialized density is doubled in order to reduce the fluid temperature by a factor of 2 (dashed magenta), and thus match the experimental T_e profile. No significant difference in the dynamics was observed.

Physical processes that might be important to the $T_{e,q2}$ collapse that are not included in these NIMROD simulations are radiation losses, two fluid effects, and kinetic effects such as finite Larmor radii and banana orbits. It is not obvious how the results would change if two fluid effects were included. Radiation losses and kinetic effects are both expected to increase perpendicular thermal and particle transport, which would likely further degrade the simulated T_e profiles, and possibly lead to stochastization of the 2/1 island. We conclude that single fluid resistive MHD is a sufficient physics basis to describe the onset of chaotic fields in the vicinity of the 3/1 and 4/1 islands, but other physics is needed to describe the inward propagation of

the collapse to the $q = 3/2$ surface.

4.5 Major disruptions

In this section, we show how the $T_{e,q2}$ collapse can lead to a major disruption. The physics that differentiates a $T_{e,q2}$ collapse from a major disruption, namely the mechanisms responsible for the collapse of the core, and separately for the current quench, are not studied in this work. Most major disruptions caused by LMs in DIII-D, particularly those at a high l_i/q_{95}, begin with a $T_{e,q2}$ collapse, followed by a collapse of the core thermal energy some time later. Here, we revisit discharge 154576 which was discussed in section 4.3, but at a later time when a major disruption occurs. Unlike the $T_{e,q2}$ collapse shown in section 4.3, here the edge temperature profile never recovers.

The $T_{e,q2}$ collapse occurs in ~ 5 ms with only a small change in the core temperature of about 100 eV, as shown in figure 4-10b. Like the previous $T_{e,q2}$ collapses in this discharge, this collapse begins when the phase-difference between the 4/1 and 3/1 O-points at the outboard midplane goes to zero (see the third vertical line marker in figure 4-4b). Further, note the similarity in the collapsed T_e profiles at 4.8 ms in 4-10b (the disruptive case) and at 10 ms in figure 4-3a (the benign $T_{e,q2}$ collapse case). The difference between the two cases is that the initial $T_{e,q2}$ collapse is followed or not by a complete thermal quench (including the core) and current quench.

As shown in figure 4-10c, the fast collapse of the core occurs ~ 23 ms after the $T_{e,q2}$ collapse, which lasts ~ 5 ms. This temporal separation of the $T_{e,q2}$ and core collapses suggests that they are triggered under different conditions. The collapse of the core is a necessary step in a major disruption, and therefore core MHD stability (e.g. 1/1 stability) likely differentiates a full thermal quench from a $T_{e,q2}$ collapse. Core stability was not investigated in this work.

The large growth of the perturbed fields in this disruption occurs after the majority of the thermal energy is quenched. When the T_e profile becomes hollow (at 27.6 ms in figures 4-10c-d), the 1/1, 2/1, 4/1, and 3/2 fields start growing rapidly, as shown in figure 4-11. So does the 3/1 mode as well, about 1 ms later. All harmonics continue this growth until the current quench begins, about 2 ms later (vertical dashed line).

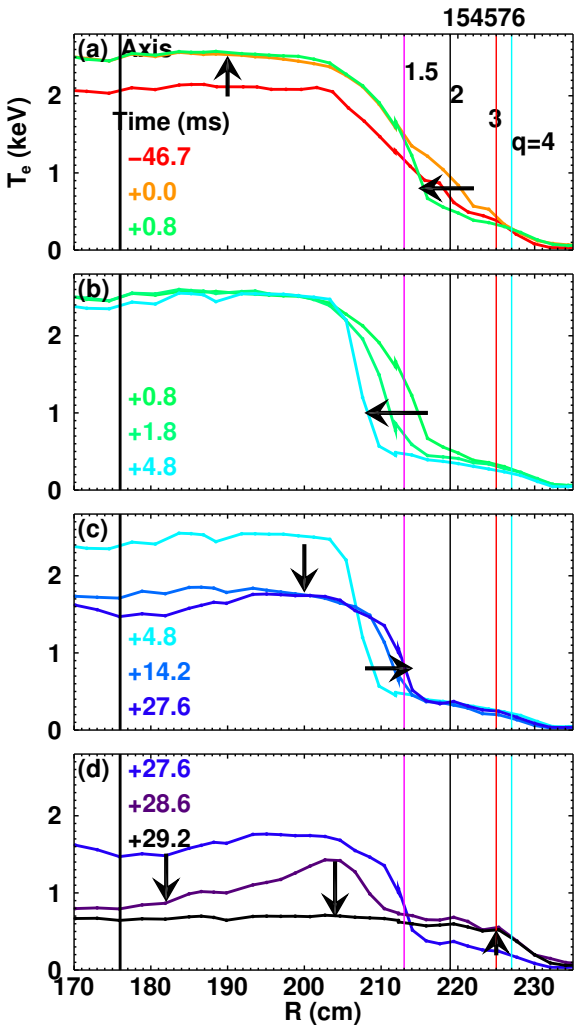

Figure 4-10: ECE profiles during a major disruption at various times relative to the disruption onset at $t = 3284.8$ ms. Vertical lines show locations of rational surfaces and the magnetic axis. Equilibrium reconstructions constrained by magnetics and the Motional Stark Effect diagnostic produce variations in the rational surface positions of ± 1 cm during this time interval. (a) The recovered profile following the $T_{e,q2}$ collapse in fig. 4-3 is shown in red. The temperature immediately before the final $T_{e,q2}$ collapse, ending in disruption, is shown in orange. The start of the $T_{e,q2}$ gradient degradation is observed by the time of the green profile. (b) Collapse of edge temperature in ~ 5 ms with only modest change in the core. (c) Relatively slow drop in core T_e and outward movement of steep T_e gradient. The profile at 27.6 ms shows a hollowing of the temperature profile, and marks the start of the core collapse. (d) Fast collapse of the core T_e and formation of off-axis peak (purple) followed by near complete gradient flattening at radii inside of $q = 4$ surface.

The growth might be caused by the destabilizing redistribution of equilibrium current observed in locked mode disruption simulations [135], or by the radiative tearing drive [124].

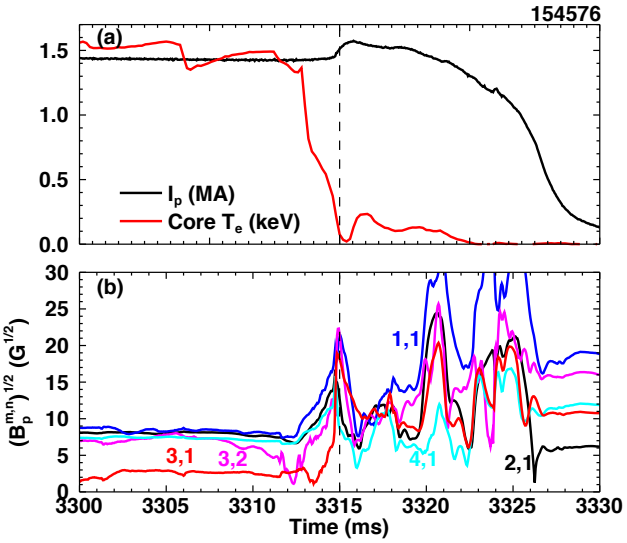

Figure 4-11: (a) Plasma current and electron temperature in the core during the thermal and current quenches. The vertical dashed line marks the beginning of the current quench. (b) The square-root of the perturbed field of various harmonics during the thermal and current quenches. For harmonics for which an island exists, this quantity is proportional to the island width. Note, however, that large islands might overlap and stochastize.

4.6 Self-stabilizing locked modes

An interesting, distinct class of locked modes that self-stabilize has been found. Self-stabilizing LMs induce a minor disruption, significantly reducing the pressure gradient and thereby removing the neoclassical tearing drive, leading to self-suppression. Note that, as discussed in the introduction, we distinguish $T_{e,q2}$ collapses from minor disruptions: in the former T_e only drops at outer radii, usually restricted to the region outside of the $q = 3/2$ surface, whereas in the latter the profile keeps evolving, and T_e also drops in the core. A minor disruption differentiates from a major one in that the plasma recovers from this T_e drop, without ever reaching the current quench.

These self-stabilizing LMs tend to occur in plasmas with a minimum q well above 1 (i.e. $q_{min} > 1.2$). Besides its fundamental relevance, a self-stabilizing LM is obviously preferable over a disruptive LM. Yet, self-stabilizing LMs can still damage reactor-scale tokamaks by way of excessive heat flux in the divertor region.

An example of a self-stabilizing LM is shown in figure 4-12. A small $n = 1$ rotating precursor grows until locking at $\sim$ 1920 ms (Figs. 4-12b-c). During locking, the plasma normalized beta β_N decreases (Fig. 4-12e). In an effort to maintain the requested β_N, the feedback-controlled neutral beam power is increased to $\sim$ 14 MW (Fig. 4-12f), also increasing the injected torque from 2.5 Nm to 4 Nm (not shown). The LM grows to $\sim$ 100 G (Fig. 4-12a), causing a minor disruption at 1965 ms. Prior to that, $q_0 > 2$ and $q_{min} < 1.5$ (Fig. 4-12d), producing *double* $q = 2$ and $q = 3/2$ surfaces. The T_e profile prior to the collapse shows large flattened regions around the outer $q = 2$ surface and inner $q = 3/2$ surface (figure 4-13, black).

At the onset of the thermal collapse, when the $n = 1$ field is maximum, the ECE data become chaotic outside of the inner $q = 3/2$ surface. This is illustrated by the red crosses in Fig. 4-13, suggesting that the electron-velocity distribution is non-Maxwellian at this time. A possible interpretation is island overlap might redistribute flux on a fast timescale, producing an electric field through $\partial\mathbf{B}/\partial t$, which could modify the electron velocity distribution. Within 1 ms of this event, the plasma appears to be Maxwellian again, but significantly colder ($T_e < 300$ eV, in green in Fig. 4-13).

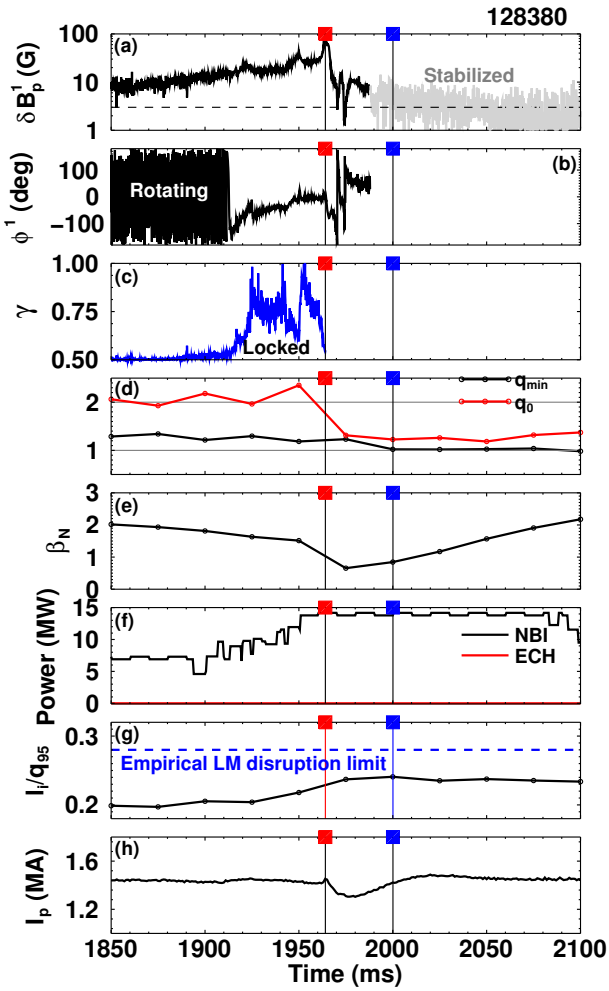

Figure 4-12: Example of a "self-stabilizing" LM. Vertical lines mark the times and their markers match the colors of the ECE profiles in figure 4-13. (a) Time trace of the $n = 1$ Fourier amplitude of the poloidal field (compensated for wall eddy currents using the method of section 4.2.3). The mode is suppressed by $\sim$ 1985 ms. (b) Phase of $n = 1$ poloidal field. (c) The γ function (equations 4.8-4.9) quantifies the correction for eddy currents applied in figure (a). (d) Time trace of q on axis, q_0, and minimum q, q_{min}, from 2D equilibrium reconstructions constrained by magnetics and the Motional Stark Effect measurements. (e) Plasma normalized beta β_N. (f) Neutral beam injection (NBI) power and electron cyclotron heating (ECH) power. (g) The ratio of internal inductance and safety factor l_i/q_{95} remains below the empirical DIII-D locked mode disruption limit [13]. (h) Plasma current shows a small dip and recovery following the minor disruption.

Following the minor disruption, q_0 and q_{min} decrease (Fig. 4-12d) and l_i increases, indicating transport of toroidal current towards the core. Despite the increase in l_i, the ratio l_i/q_{95} remains below the disruption threshold for LMs with rotating precursors to cause disruptions [13]. In agreement with that limit, the plasma does not undergo a major disruption. Following the near complete thermal quench (green profile in figure 4-13), the plasma current undergoes only a small oscillation and does not quench (Fig. 4-12h). The T_e profile largely recovers by 2000 ms (blue profile in figure 4-13), and the $n = 1$ mode is no longer present (Fig. 4-12a-b).

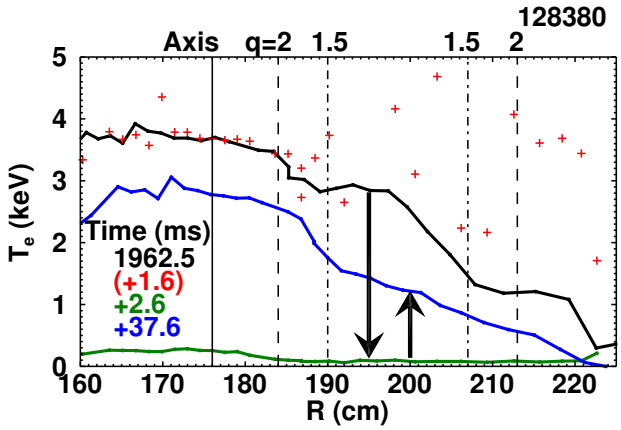

Figure 4-13: Electron temperature profiles measured by ECE during a minor disruption that leads to LM self-stabilization. Red crosses show the ECE data during the onset of the collapse; the erratic behavior for $R > 190$ cm might indicate a non-Maxwellian velocity distribution. If so, the quantity plotted should not be interpreted as T_e, at that particular time, but as the radiative temperature T_{rad}. The vertical dashed and dash-dotted lines show the existence of double $q = 2$ and $q = 3/2$ surfaces at the time of the first profile.

At the time of the thermal quench, the pressure gradient at the $q = 2$ surface is approximately zero, and therefore the bootstrap drive is negligible. The decay of the 2/1 mode at this time implies that the island-width-dependent classical stability index $\Delta'(w)$ is negative (i.e. stabilizing). The 2/1 mode stabilizes before the bootstrap term is re-introduced by the recovering T_e profile. Decay of the LM is rarely observed in discharges with high values of l_i/q_{95}, suggesting a connection between l_i/q_{95} and $\Delta'(w)$, which is investigated numerically in [117]. Later in the discharge, another 2/1 mode also self-stabilizes after causing a minor disruption, though this time $l_i/q_{95} =$

0.33 is above the empirical disruption limit of 0.28, where a disruption is otherwise expected. Although a strong correlation between the likelihood of LM disruptions and l_i/q_{95} is presented in [13], it is clear that additional factors exist that are not captured by this parameter. The discharge ends without LMs with a pre-programmed ramp-down (i.e. safely and without any disruption avoidance actuators).

Most self-stabilizing LMs are observed to cause a sudden "global" thermal collapse, like the one presented in figure 4-13, unlike LM induced non-self-stabilizing minor disruptions or major disruptions which typically occur in two phases: (1) a $T_{e,q2}$ collapse at outer radii, followed by (2) a collapse in the core. This suggests that the underlying physical mechanism responsible for the thermal collapse in the self-stabilizing case might be different from that of the non-self-stabilizing minor disruption (not shown) or the major disruption (Fig. 4-10). The thermal collapse in the self-stabilizing case might be related to the presence of multiple $q = 3/2$ or $q = 2$ surfaces, and the overlap of double 3/2 or double 2/1 TMs. The lack of a current quench might be related to the relatively low value of l_i/q_{95}.

4.7 Summary and conclusions of the relationships between locked islands and thermal collapses

In this chapter we analyzed the effect of locked modes on temperature profiles in the DIII-D tokamak in order to better understand when and how locked modes cause thermal quenches and, eventually, major disruptions. It was found that locked modes of poloidal/toroidal mode number m/n=2/1 often cause the electron temperature T_e to transiently collapse in a region extending from the island to the plasma edge. Such collapses should not be confused with the local non-axisymmetric flattening of T_e which occurs at the island location -whether locked or rotating. Instead, these collapses appear *axisymmetric*, they span a broader radial range crossing several low-order rational surfaces, and appear to be due to the mutual interaction of several n=1 islands, of m=2, 3 and 4, and possibly others. The measured island widths are comparable with the island mutual distances, as confirmed by the calculated Chirikov parameters, and thus consistent with field stochastization. In turn, this is compatible with enhanced transport and a decrease of the T_e profile. Nonlinear MHD simulations performed with the NIMROD code support the interpretation that the field becomes stochastic in the plasma region on the vacuum side of the 2/1 island, though the 2/1 island itself does not become stochastic. The lack of stochasticity at the $q = 2$ surface might be attributed to the significant decay of the 2/1 island in the simulation, which is not consistent with experimental magnetics data. Additional mechanisms of plasma-edge cooling by the locked mode are not excluded. However, initial evidence suggests heat to be predominantly lost in the divertor region, through radiation and conduction or convection.

Experimentally, the relative phase between the islands also plays a role. In particular, their O-points tend to toroidally align with each other on the midplane at the time of the T_e collapse. The conditions for island-overlap might depend on poloidal angle, and might become critical when O-points align at the outboard or inboard midplanes.

These T_e collapses are common but not sufficient conditions for thermal quenches.

The main difference is that in the former, the temperature only collapses at outer radii, whereas in the latter, it also decreases in the core, at a later time that distinctly separates it from the $T_{e,q2}$ collapse. The decrease in the core is not fully understood, but it might be due to an instability associated with the 1/1 mode.

In turn, the thermal quench may or may not initiate a current quench. When it does, a major disruption occurs. When it does not, the disruption is minor, the locked mode tends to decay -at least *partially*- or unlock and spin-up, and confinement is recovered. Previous work [13] helps discriminating between major and minor disruptions: at DIII-D, locked modes tend to cause major disruptions when l_i/q_{95} >0.28. Here l_i is the internal inductance, q_{95} the edge safety factor, and l_i/q_{95} is believed to be a proxy for the classical stability parameter Δ' [117]. Finally, as a special case of minor disruptions, locked modes were observed to "self-heal" or *completely* stabilize themselves. The behavior was ascribed to the reduction of pressure, hence of pressure-gradient and consequent removal of the neoclassical drive of the island in discharges which are believed to be classically stable due to the low value of l_i/q_{95}.

In the future, an extensive statistical survey of many $T_{e,q2}$ collapses might be necessary to assess the universality, or lack thereof, of the results obtained in the selected discharges presented herein. Analysis of core 1/1 stability might provide the insight necessary to differentiate between a relatively benign $T_{e,q2}$ collapse that recovers, from a minor or major disruption. Physical understanding of this instability and of its causes might improve disruption avoidance techniques. More generally, techniques to prevent the $T_{e,q2}$ collapse might significantly reduce the occurrence of locked mode disruptions.

Chapter 5

Conclusions and future work

5.1 Conclusions

This thesis studies the resistive magnetohydrodynamics instability referred to as the tearing mode (TM). TMs can rotate with the plasma (kHz frequencies in the devices studied herein) or they can come to rest ("lock") in the laboratory frame. The deceleration of the initially rotating mode is due to an electromagnetic drag imposed by the resistive vessel wall, and the final locking is typically due to a torque resulting from imperfections in the externally applied fields known as error fields (EFs). Following the locking of a TM, the plasma often loses all thermal energy on a timescale much shorter than typical energy confinement times. Subsequently, the cold, resistive plasma loses all the stored magnetic field energy; the event where all thermal and magnetic energy are lost in an uncontrolled manner is referred to as a disruption. Experimental results from two toroidal plasma configurations called the reversed field pinch and the tokamak are used in this work. The reversed field pinch studied herein is located in Stockholm, Sweden and is called EXTRAP T2R. The tokamak studied herein is located in San Diego, California and is called DIII-D.

Here, the first use of TMs to diagnose resonant error fields is demonstrated, results of a locked mode (LM) database on DIII-D pertaining to nonlinear plasma and mode properties and LM disruptivity are presented, and experimental observations of the onset mechanism of LM induced partial and full thermal quenches are shown. The

error field and database works are published in references [81] and [13] respectively. Here we summarize the primary findings of each of these studies.

It is demonstrated for the first time that naturally rotating TMs can be used to diagnose EFs in the plasma conditions of EXTRAP T2R. The tearing mode (TM) amplitude is observed to modulate in the presence of a resonant field, resulting from the superposition of an intrinsic error field (EF) and a known, applied resonant magnetic perturbation (RMP). By scanning the amplitude and phase of the RMP, the amplitude and phase of the intrinsic EF are estimated. The fastest TM rotation, and a decoupling of the modulations in the TM amplitude from its phase are observed when the predicted intrinsic EF is approximately canceled.

The statistical study of $m/n = 2/1$ (where m and n are the poloidal and toroidal harmonics) LMs with rotating precursors, also referred to as initially rotating locked modes (IRLMs), in DIII-D confirmed some expectations, and challenged others. Among the confirmed expectations are the shorter slow-down times for tearing modes (TMs) when the wall torque is large, the significant effect of locked modes on the normalized beta β_N, and the common toroidal angle where locked modes (LMs) tend to align, probably as a result of residual error fields.

Results that were not expected include:

1. The maximum β_N achieved during the discharge does not strongly influence whether an IRLM will disrupt or not. Note that β_N is significantly degraded during the locked phase, and thus the β_N prior to disruption is often much less than the maximum value in the discharge, and typically much less than the ideal wall and no-wall stability limits.

2. The following parameters, when considered alone, do not differentiate disruptive from non-disruptive IRLMs well:

   (a) The plasma internal inductance l_i

   (b) The safety factor q_{95}

   (c) The island width w

(d) The radial derivative of the q profile at the $q = 2$ location $dq/dr|_{q2}$

3. The following parameters do differentiate disruptive from non-disruptive IRLMs well:

   (a) The ratio of the internal inductance to the safety factor l_i/q_{95}

   (b) A linear combination of the island width and radial position, $d_{edge} = a - (r_{q2} + w/2)$, where a and r_{q2} are the minor radii of plasma and the $q = 2$ surface. The quantity d_{edge} can be interpreted as the minimal distance between the island outer separatrix and the unperturbed plasma edge.

The ratio l_i/q_{95} is believed to be related to the free energy in the current profile to drive TMs, commonly referred to as Δ'. A numerical work [117] found a similar connection between l_i/q_{95} and Δ'. This is the first empirical work to identify this parameter as a robust disruption limit for LMs with rotating precursors, independent of other plasma parameters. l_i/q_{95} has been identified as a disruption limit in both high density discharges in JET [71], and current ramp-down disruptions in JT-60U [74], attributed to tearing instabilities in both. It is possible that the density limit and current ramp-down are not causes of disruptions, but rather conditions under which locked modes often form, the l_i/q_{95} disruption threshold is exceeded, and disruptions occur.

Although by definition current quenches are not observed in discharges with *non-disruptive* IRLMs, thermal quenches often are observed. Discharges with non-disruptive IRLMs tend to have low values of l_i/q_{95} (less than ~ 0.28). We offer a hypothesis as to the role of l_i/q_{95} in distinguishing disruptive from non-disruptive LMs:

- It is possible that l_i/q_{95} determines the dynamics immediately following the thermal quench, allowing plasma recovery when l_i/q_{95} is low, or causing a current quench when it is high. For instance, l_i/q_{95} might determine whether LMs decay when the neoclassical drive becomes negligible following the thermal quench, or whether they continue to grow, somehow inducing the current quench.

The parameter d_{edge} might approximately indicate when neighboring island chains will overlap, resulting in stochastic magnetic fields and poor confinement. As d_{edge} is defined for a single island, d_{edge} is not sufficient to determine when two separate island chains overlap. Nevertheless, when d_{edge} is comparable to the $m/n = 2/1$ island half-width, it is likely that overlap would occur if other islands on the vacuum side of the 2/1 exist (e.g. if islands with $m > 2$ and $n = 1$ exist). It is likely that these other islands exist, as toroidal coupling implies that the $m/n = 3/1$ island will be driven by the $m/n = 2/1$. Poloidal spectra of locked modes confirm the existence of many island chains in these discharges, including the 3/1 and 4/1.

d_{edge} is found to correlate best with the time duration between locking and disruption, suggesting that it might be related to the disruption onset mechanism. It also performs comparably to the parameter l_i/q_{95} in its ability to distinguish disruptive from non-disruptive locked modes.

The database analysis revealed a fairly reproducible feature ("$T_{e,q2}$ collapse") in the evolution of the electron temperature profile during locked mode disruptions. This motivated a more detailed analysis that, however, due to its complexity, was not automated, but only conducted on a handful of discharges.

All observations of the $T_{e,q2}$ collapse are consistent with the overlap of $n = 1$ islands being the cause, though the statistics of this study are small. The following observations were made in two discharges with IRLMs:

1. The electron temperature T_e flattens in a region extending from the edge to locations where the safety factor evaluates $q = 3/2$

    (a) Both the Electron Cyclotron Emission and Thomson Scattering diagnostics -in different toroidal and poloidal locations-measure the collapse, suggesting an axisymmetric perturbation

2. All $T_{e,q2}$ collapses (often multiple per discharge) occur when the Chirikov parameter for the outermost $n = 1$ islands approaches or exceeds unity, and when the island O-points align with each other at the outboard or inboard midplanes

These observations are consistent with the outermost $n = 1$ islands overlapping or nearly overlapping with each other, resulting in stochastic fields, and an axisymmetric collapse of the edge electron temperature. Due to the Shafranov shift and the elliptical shaping, the O-points of separate island chains are closer in real space when aligned at the outboard midplane than when aligned at any other poloidal position. It is possible that this point of closest approach is related to the physics of the onset, as it is comparable with other transport length scales like the ion banana width and ion gyroradius.

The $T_{e,q2}$ collapse proceeds in a similar way to the onset of a density limit disruption, though their respective onset mechanisms appear to be different. In a density limit disruption, radiative losses overcome heating at the plasma edge resulting in an axisymmetric T_e collapse. Radiation accounts for 100% of the lost thermal energy, and TMs appear *as a result of the collapse* [71]. In the case of the $T_{e,q2}$ collapse, the density is often well below the density limit, and the collapse occurs *coincident with MHD activity*. Further, tracking the lost thermal energy during a single $T_{e,q2}$ collapse shows 50-60% radiated in the divertor region, with the remaining energy conducted or convected to the divertor. No increase in divertor heat flux is expected at the onset of the density limit disruption.

The NIMROD nonlinear, single fluid, resistive magnetohydrodynamics code corroborates the presence of stochastic magnetic fields under the conditions when the $T_{e,q2}$ collapse is triggered. The fields in the plasma region outside of the $q = 2$ surface become stochastic, and an axisymmetric collapse of the temperature profile is observed. However, the temperature decrease observed in the simulations is smaller than observed in experiments, suggesting that a larger region of stochastic fields might exist in the experiments.

5.2 Future work

The error field detection technique might be considered for use on other reversed field pinches and tokamaks. In ITER, simple scaling arguments presented in section

2.7.2 suggest that the modulation in the island rotation frequency is expected to be measurable, while the modulation in the island amplitude might not be.

The database and thermal quench work suggest that the first transient loss of thermal energy is caused by overlap of the outermost $n = 1$ islands, and that classical tearing stability determines whether a current quench follows the thermal quench or not. Future work might attempt to further solidify these findings by completing the following steps:

1. Extend the analysis of the $T_{e,q2}$ collapse to a larger set of randomly chosen locked mode discharges to confirm or deny the universality of the onset mechanism.

2. Test the dependence of stochastic field generation on the poloidal position at which the O-points of neighboring $n = 1$ island chains align, using NIMROD or an equivalent nonlinear resistive MHD code.

    - If no dependence is found using a resistive MHD fluid code like NIMROD, then the mechanism is likely not a fluid effect, and a kinetic explanation should be sought.

3. Calculate the classical stability index Δ' by solving for the perturbed flux function using $J_{\|}$ from Motional Stark Effect constrained equilibrium fit reconstructions during the existence of locked modes. Next, compare the calculated Δ' with l_i/q_{95} to confirm or deny the expected correlation.

Future work should also explore ways to avoid the $T_{e,q2}$ collapse, as this might lead to avoiding the subsequent thermal quench and current quench (that is, the disruption). Avoidance techniques might include:

1. Changing the global current profile during the existence of a locked mode to reduce l_i, and thus reduce Δ'.

2. Reduce the magnetic shear at the edge to prevent edge island overlap by increasing plasma current in the edge.

- Both techniques 1 and 2 could make use of electron cyclotron current drive (ECCD). They should not, however, be confused with ECCD stabilization of the LM. Note that the ECCD efficiency is expected to be low in the cold plasma edge.

3. Alternatively, the plasma current might be increased inductively at the highest allowable central solenoid ramp-rate so as to drive more edge-current than core-current. This is obviously only a transient solution, to be paired with an island suppression method. Note that this technique would reduce q_{95}, potentially with adverse effects on the classical stability of the LM, or possibly destabilize an ideal kink.

Appendices

Appendix A

The DIII-D initially rotating locked mode database

Details on the structure of the database and how to access it can be found at the following link:

https://docs.google.com/document/d/1wqhvH8c6Ue9smP6kmsc8LTy1tIHLO4MTLRjjBCq4bTA/edit

Appendices B-C

Available at https://doi.org/10.1088/0741-3335/58/12/124001

Appendices D-E

Available at https://doi.org/10.1088/0029-5515/57/1/016019

Appendix F

Discussion of non-axisymmetric interpretations of the $T_{e,q2}$ collapse

Here, we investigate *non-axisymmetric* interpretations that are consistent with the electron temperature profile observations. These interpretations are shown to be inconsistent with the magnetics data, or require parallel electron temperature gradients, making all non-axisymmetric interpretations unlikely. The *axisymmetric* collapse interpretation caused by overlapping islands is discussed in the main text.

By non-axisymmetric collapse, we mean that at a fixed toroidal angle, and on any flux surface in the region of the observed collapse, there ought to exist a poloidal angle where the temperature during the collapse is similar to the pre-collapse value. This property would be satisfied, for example, if a single, large island was responsible for the $T_{e,q2}$ collapse.

Single island interpretation

In this interpretation, we assume that the flattened T_e profiles in figure 4-3a are the result of a single, large island. The poloidal fields of the various m/n harmonics do not significantly decay as it might be expected if only one large island existed, as shown in figure 4-3b. The arguments below further challenge this interpretation.

For this single island interpretation, and the multi-island interpretation in section

F, we note that it is possible for a sudden change in island topologies to cause both the ECE and TS diagnostics to view only island O-points. In order for an island to align with both the ECE and TS diagnostic, they must satisfy the following helicity constraint:

$$\chi = n(q\Delta\theta + \Delta\phi) \approx n\pi\left(\frac{q}{3} + \frac{1}{5}\right) \approx 2N\pi \tag{F.1}$$

where χ is the helical angle on a flux surface that is perpendicular to the equilibrium field, n is the toroidal harmonic, q is the safety factor at the island location, $\Delta\theta \approx \pi/3$ and $\Delta\phi \approx \pi/5$ are the angular separations of the TS and ECE diagnostics, and N is any non-zero integer.

We consider only the harmonics for which the corresponding rational surface exists in the region of the collapse. The 4/2, 5/2, and 5/3 harmonics are the only ones for which the helical angle χ comes within 0.3π radians of the constraint in equation F.1, exist on a rational surface in the range $q = 1.5$ to 4, and have $m < 9$. We will now investigate the width of each of these islands.

For the observed profiles to be explained by a single island, the island width must be 10-15 cm. The cylindrical island width of the m/n island is given by [50],

$$w^{m,n} = c\sqrt{\frac{16RB_r^{m,n}q^2}{mB_T(dq/dr)}}, \tag{F.2}$$

where c is a toroidal correction factor, R is the major radius, $B_r^{m,n}$ and dq/dr are the radial field and the radial derivative of the safety factor at the $q = m/n$ rational surface, and B_T is the toroidal field at the magnetic axis.

We seek the required values of the 4/2, 5/2, and 5/3 perturbed fields to produce an island that is at least 50% larger than the 2/1 island width in figure 4-3a, and then compare these with the measured values.

Magnetic requirements for 4/2 island interpretation

Assuming c to be mode independent (here, and in the following subsections), in order for the 4/2 island width to be at least 50% larger than the 2/1 width, the following condition on the perturbed radial field must be true,

$$\sqrt{B_r^{4,2}} \geq 2.1\sqrt{B_r^{2,1}} \tag{F.3}$$

Taking the pre-collapse value of $\sqrt{B_r^{2,1}} \approx 8$ G$^{1/2}$ from figure 4-3b, we find the condition $\sqrt{B_r^{4,2}} \geq 17$ G$^{1/2}$. The measured value of $\sqrt{B_r^{4,2}}$ during the $T_{e,q2}$ collapse is 9 G$^{1/2}$, which is too small. In addition, it is observed to transiently decrease coincident with the onset of the $T_{e,q2}$ collapse, whereas an increase would be expected (Fig. 4-3b). We conclude that the interpretation of a single 4/2 island causing the collapse is not consistent with the magnetics data.

Magnetic requirements for 5/2 island interpretation

We can formulate a similar argument for the interpretation of a single 5/2 island causing the $T_{e,q2}$ collapse. Requiring that the 5/2 island be at least 50% larger than the 2/1 island, we find the following condition,

$$\sqrt{B_r^{5,2}} \geq 1.9\sqrt{\frac{(dq/dr)^{5,2}}{(dq/dr)^{2,1}}}\sqrt{B_r^{2,1}} \tag{F.4}$$

where $(dq/dr)^{5,2}$ and $(dq/dr)^{2,1}$ are the radial derivatives of the safety factor at the $q = 5/2$ and the 2/1 surfaces. For simplicity, we will set the ratio of the 5/2 and 2/1 radial derivatives of the safety factor to unity, though in reality, this ratio is greater than unity in discharge 154576 (as it is in most DIII-D discharges). Taking the pre-collapse value of $\sqrt{B_r^{2,1}} \approx 8$ G$^{1/2}$, equation F.4 requires $\sqrt{B_r^{5,2}} \geq 15.2$ G$^{1/2}$. A decomposition of the magnetics using basis functions with $0 < m \leq 5$ and $0 < n \leq 2$ finds $\sqrt{B_r^{5,2}} = 5.4$ G$^{1/2}$ at the onset of the $T_{e,q2}$ collapse. This signal is much too small to produce an island width of 10-15 cm, and therefore, the interpretation of a single 5/2 island causing the observed profiles in figure 4-3a is not consistent with the

magnetics data.

Magnetic requirements for 5/3 island interpretation

Finally, we consider the 5/3 island. Requiring this island to be 50% larger than the pre-collapse 2/1 width, we find,

$$\sqrt{B_r^{5,3}} \geq 1.6\sqrt{\frac{(dq/dr)^{5,3}}{(dq/dr)^{2,1}}}\sqrt{B_r^{2,1}} \tag{F.5}$$

With $(dq/dr)^{5,3} = 6.5$ m^{-1} and $(dq/dr)^{2,1} = 10.5$ m^{-1}, the condition in equation F.5 evaluates to $\sqrt{B_r^{5,2}} \geq 10$ G$^{1/2}$. A decomposition of the magnetics using basis functions with $0 < m \leq 5$ and $0 < n \leq 3$ finds $\sqrt{B_r^{5,3}} = 8.7$ G$^{1/2}$. Although this field is comparable to 10 G$^{1/2}$, note that the condition in equation F.5 is already rather conservative in requiring that the 5/3 island width be only 50% larger than the 2/1. Further, the $q = 5/3$ surface is near the inner-side of the collapsed region, requiring this island to be radially asymmetric in a way opposite to the typical island asymmetries observed in DIII-D (e.g. see the 2/1 flattening in the TS profile in figure 4-3a).

Multiple, non-overlapping island interpretation

For this interpretation, we assume that more than one island chain is responsible for the profiles in figure 4-3a, and that the islands *do not overlap*, (as overlap would cause stochastic fields, resulting in an axisymmetric collapse). In this and the following subsection, the fast thermal conductivity and transport parallel to the magnetic field is used to challenge the interpretations.

Excluding large parallel T_e gradients, T_e should not change along the island separatrix. Therefore, the temperatures at the inner and outer boundaries of the O-point, and the X-point should be the same. That is to say that measuring T_e at the O-point separatrix provides an approximate measurement of the X-point temperature.

If multiple island X-point gradients do exist in the discharge shown in figure 4-3a, and are all not in view of the TS or ECE view chords, the O-points of neighboring

island chains should have different temperatures, producing a profile with a "stair-step" characteristic. The orange profile in figure 4-3a does not show this "stair-step" characteristic, but rather shows a steady weak gradient. We conclude that a *non-axisymmetric* collapse caused by multiple *non-overlapping* island chains, excluding large parallel T_e gradients, is not consistent with the measured profiles.

Non-resonant interpretation

A 3D *non-resonant* temperature collapse necessarily implies large parallel T_e gradients. By definition, the wave-vector of a non-resonant perturbation $\mathbf{k}$ is not perpendicular to the equilibrium field, which implies that a single field line traverses peaks and troughs of the wave, or in this case, traverses high and low temperature regions.

Bibliography

[1] http://csm.jmu.edu/physics/courses/163/older/bepn2.jpg, Feb. 2017.

[2] https://www.euro-fusion.org/2011/09/tokamak-principle-2/, Oct. 2016.

[3] E.J. Strait, E.D. Fredrickson, J.-M. Moret, and M. Takechi. *Fusion Sci. Technol.*, 53:304–334, 2008.

[4] K. Erik J. Olofsson, Per R. Brunsell, James R. Drake, and Lorenzo Frassinetti. *Plasma Phys. Contr. Fusion*, 54(9), 2012.

[5] K.E.J. Olofsson et al. *Plasma Phys. Contr. Fusion*, 58(045008), 2016.

[6] J. Ongena, R. Koch, R. Wolf, and H. Zohm. *Nature Physics*, 12:398–410, 2016.

[7] P.C. de Vries and M.F. Johnson. *Nucl. Fusion*, 51(053018), 2011.

[8] S.C. Prager. The reversed field pinch: on the path to fusion energy. Fusion Power Associates Symposium, 2006.

[9] R. Fridström, L. Frassinetti, and P.R. Brunsell. *Plasma Phys. Contr. Fusion*, 57(104008), 2015.

[10] E.J. Strait et al. *Nucl. Fusion*, 43:430–440, 2003.

[11] K.E.J. Olofsson, J.M. Hanson, D. Shiraki, F.A. Volpe, et al. *Plasma Phys. Contr. Fusion*, 56(095012), 2014.

[12] L.L. Lao, H. St. John, and R.D. Stambaugh. *Nucl. Fusion*, 25(10):1421–1436, 1985.

[13] R. Sweeney, W. Choi, R.J. La Haye, S. Mao, K.E.J. Olofsson, and F.A. Volpe. *Nucl. Fusion*, 57(016019), 2017.

[14] P.R. Brunsell et al. *Plasma Phys. Contr. Fusion*, 43(1457), 2001.

[15] L. Frassinetti et al. *Nucl. Fusion*, 50(035005), 2010.

[16] J. Freidberg. *Plasma Physics and Fusion Energy*. Cambridge University Press, 2007.

[17] M. Keilhacker et al. *Nucl. Fusion*, 39(2):209–234, 1999.

[18] M. Shimada, D.J. Campbell, V. Mukhovatov, M. Fujiwara, N. Kirneva, et al. *Nucl. Fusion*, 47(6), 2007.

[19] T.C. Hender, J.C. Wesley, et al. *Nucl. Fusion*, 47:S128–S202, 2007.

[20] John N. Bahcall. ^{7}Be solar neutrino line: A reflection of the central temperature distribution of the sun. *Phys. Rev. D*, 49:3923–3945, Apr 1994.

[21] F.A. Volpe. Plasma 1 notes. Columbia University, Fall 2012.

[22] F.F. Chen. *Introduction to Plasma Physics and Controlled Fusion*, volume 1. Plenum Press, 1984.

[23] J.D. Lawson. Some criteria for a useful thermonuclear reactor. Technical report, Atomic Energy Research Establishment, 1957.

[24] H.J. de Blank. Guiding center motion. *Fusion Sci. Technol.*, 61(2T):61–68, 2012.

[25] R. Prater. *Phys. Plasmas*, 11(5):2349–2376, 2004.

[26] T.C. Simonen, M. Matsuoka, et al. *Phys. Rev. Lett.*, 61(15):1720–1723, 1988.

[27] M. Brambilla. *Nucl. Fusion*, 16(1):47–54, 1976.

[28] S.I. Braginskii. Transport processes in a plasma. *Reviews of Plasma Physics*, 1, 1965.

[29] J.P. Freidberg. *Ideal Magnetohydrodynamics*. Plenum Press.

[30] J.L. Luxon. *Nucl. Fusion*, 42:614–633, 2002.

[31] E.J. Strait. *Rev. Sci. Instrum.*, 77(023502), 2006.

[32] J.D. King, E.J. Strait, R.L. Boivin, D. Taussig, M.G. Watkins, et al. *Rev. Sci. Instrum.*, 85(083503), 2014.

[33] E.J. Strait, J.D. King, J.M. Hanson, and N.C. Logan. *Rev. Sci. Instrum.*, 87(11D423), 2016.

[34] B.W. Rice, D.G. Nilson, and D. Wróblewski. *Rev. Sci. Instrum.*, 66(1):373–375, 1995.

[35] J.L. Luxon and B.B. Brown. *Nucl. Fusion*, 22(6):813–821, 1982.

[36] M.E. Austin and J. Lohr. *Rev. Sci. Instrum.*, 74(3), 2003.

[37] T.N. Carlstrom et al. *Rev. Sci. Instrum.*, 63(10):4901–4906, 1992.

[38] I.H. Hutchinson. *Principles of Plasma Diagnostics*. Cambridge University Press, second edition, 2002.

[39] L. Frassinetti, K.E.J. Olofsson, P.R. Brunsell, and J.R. Drake. *Nucl. Fusion*, 51(063018), 2011.

[40] E. Olofsson and P. Brunsell. *Fus. Eng. Design*, 84:1455–1459, 2009.

[41] P.H. Rutherford. *Phys. Fluids*, 16(11), 1973.

[42] A.H. Glasser, J.M. Greene, and J.L. Johnson. *Phys. Fluids*, 18(7):875–888, 1975.

[43] W.X. Qu and J.D. Callen. Technical report, University of Wisconsin Report No. UWPR 85-5, 1985.

[44] Z. Chang, J.D. Callen, E.D. Fredrickson, et al. *Phys. Rev. Lett.*, 74(23), 1995.

[45] A.M. Garofalo et al. *Fusion Eng. Des.*, 89:876–881, 2014.

[46] P.C. de Vries, M.F. Johnson, I. Segui, et al. *Nucl. Fusion*, 49(055011), 2009.

[47] S.P. Gerhardt et al. *Nucl. Fusion*, 53(043020), 2013.

[48] R.J. Buttery et al. *Nucl. Fusion*, 44:1027–1035, 2004.

[49] J.A. Wesson. *Nucl. Fusion*, 18(1):87–132, 1978.

[50] J. Wesson et al. *Tokamaks*. Oxford University Press, 3 edition, 2004.

[51] Z. Chang and J.D. Callen. *Nucl. Fusion*, 30(2), 1990.

[52] R.J. La Haye et al. *Phys. Plasmas*, 10(9), 2003.

[53] J.M. Finn, A.J. Cole, and D.P. Brennan. *Phys. Plasmas*, 22(120701), 2015.

[54] J.A. Snipes et al. *Nucl. Fusion*, 28(6), 1988.

[55] F.D. Halpern, A.H. Kritz, G. Bateman, A.Y. Pankin, R.V. Budny, and D. McCune. *Phys. Plasmas*, 15(062505), 2008.

[56] R.J. La Haye, A. Isayama, and M. Maraschek. *Nucl. Fusion*, 49(045005), 2009.

[57] R.J. La Haye. *Phys. Plasmas*, 13(055501), 2006.

[58] A.J. Cole. Plasma 2 notes. Columbia University, Spring 2013.

[59] H. R. Strauss. Nonlinear tokamak stability. *The Physics of Fluids*, 19(9):1411–1416, 1976.

[60] D.D. Schnack. *Lectures in Magnetohydrodynamics*. Springer-Verlag Berlin Heidelberg, 2009.

[61] H. R. Strauss. Dynamics of high β tokamaks. *The Physics of Fluids*, 20(8):1354–1360, 1977.

[62] R. Fitzpatrick. Driven reconnection in magnetic fusion experiments. Lecture given at summer school on "MHD Phenomena in Plasmas", August 1995.

[63] H.P. Furth, J. Killeen, and M. Rosenbluth. *Phys. Fluids*, 6(4):459–484, 1963.

[64] R. Fitzpatrick. *Nucl. Fusion*, 33(7), 1993.

[65] R.J. Goldston and P.H. Rutherford. *Introduction to Plasma Physics*. Taylor & Francis Group, 1995.

[66] Richard Fitzpatrick. *Phys. Plasmas*, 5(9), 1998.

[67] R.J. La Haye and O. Sauter. *Nucl. Fusion*, 38(7), 1998.

[68] R.J. Buttery et al. *Plasma Phys. Contr. Fusion*, 42:B61–B73, 2000.

[69] L. Urso, H. Zohm, et al. *Nucl. Fusion*, 50(025010), 2010.

[70] Kyungjin Kim, Yong-Su Na, Minhwa Kim, et al. *Curr. Appl. Phys.*, 15:547–554, 2015.

[71] J.A. Wesson, R.D. Gill, M. Hugon, F.C. Schüller, J.A. Snipes, D.J. Ward, et al. *Nucl. Fusion*, 29(4), 1989.

[72] J.T. Scoville, R.J. La Haye, et al. *Nucl. Fusion*, 31(5), 1991.

[73] R.J. La Haye, C. Paz-Soldan, and E.J. Strait. *Nucl. Fusion*, 55(023011), 2015.

[74] R. Yoshino et al. *J. Plasma Fusion Res.*, 70:1081–1101, 1994.

[75] M.J. Choi, H.K. Park, et al. *Nucl. Fusion*, 56(066013), 2016.

[76] T.H. Jensen and M.S. Chu. *Journal of Plasma Physics*, 30:57–63, 1983.

[77] C.G. Gimblett. *Nucl. Fusion*, 26(5):617–625, 1986.

[78] W. Choi, K.E.J. Olofsson, R. Sweeney, and F.A. Volpe. Feedback control of 2/1 locked mode phase: experiment on diii-d and modeling for iter. volume 61. APS Division of Plasma Physics, 2016.

[79] S.H. Strogatz. *Nonlinear Dynamics and Chaos*. Westview Press, 1994.

[80] F.A.G. Volpe et al. *Phys. Plasmas*, 16(102502), 2009.

[81] R.M. Sweeney, L. Frassinetti, P. Brunsell, R. Fridström, and F.A. Volpe. *Plasma Phys. Contr. Fusion*, 58(124001), 2016.

[82] R.M. Sweeney, L. Frassinetti, P. Brunsell, R. Fridström, and F.A. Volpe. *arXiv.org*, 1604.00294, 2016.

[83] R.J. Buttery et al. *Nucl. Fusion*, 39(11Y), 1999.

[84] H. Reimerdes et al. *Fusion Sci. Technol.*, 59:572–585, 2011.

[85] L. Frassinetti, S. Menmuir, K.E.J. Olofsson, et al. *Nucl. Fusion*, 52(103014), 2012.

[86] T.C. Hender, R. Fitzpatrick, A.W. Morris, et al. *Nucl. Fusion*, 32(12), 1992.

[87] R.J. La Haye and J.T. Scoville. *Rev. Sci. Instrum.*, 62(9), 1991.

[88] J.L. Luxon, M.J. Schaffer, et al. *Nucl. Fusion*, 43:1813–1828, 2003.

[89] J.R. Drake, P.R. Brunsell, et al. *Nucl. Fusion*, 45:557–564, 2005.

[90] F.A. Volpe et al. *Nucl. Fusion*, 53(043018), 2013.

[91] D. Shiraki, R.J. La Haye, N.C. Logan, E.J. Strait, and F.A. Volpe. *Nucl. Fusion*, 54(033006), 2014.

[92] D. Shiraki, N. Commaux, et al. *Nucl. Fusion*, 55(073029), 2015.

[93] A.C.C. Sips et al. *Plasma Phys. Contr. Fusion*, 44:B69–B83, 2002.

[94] T.C. Luce, M.R. Wade, et al. *Nucl. Fusion*, 43:321–329, 2003.

[95] A. Polsinelli. Set-up and validation of an electromagnetic model of EXTRAP T2R. Master's thesis, Università Degli Studi Di Cassino E Del Lazio Meridionale, Electrical Engineering, 2014-2015.

[96] L. Frassinetti, P.R. Brunsell, J.R. Drake, S. Menmuir, and M. Cecconello. *Phys. Plasmas*, 14(11), 2007.

[97] R.J. La Haye, C. Paz-Soldan, and E.J. Strait. *Nucl. Fusion*, 55(023011), 2015.

[98] J.M. Finn. *Phys. Plasmas*, 2:198–204, 1994.

[99] K.A. Werley, R.A. Nebel, and G.A. Wurden. *Phys. Fluids*, 28(5):1450–1453, 1985.

[100] P.R. Bevington and D. Keith Robinson. *Data reduction and error analysis for the physical sciences*. McGraw-Hill, 3 edition, 2003.

[101] S.C. Guo and M.S. Chu. *Phys. Plasmas*, 9:4685, 2002.

[102] R. Sweeney, W. Choi, R.J. La Haye, S. Mao, K.E.J. Olofsson, and F.A. Volpe. *arXiv.org*, 1606.04183, 2016.

[103] R.B. White, D.A. Monticello, and M.N. Rosenbluth. *Phys. Rev. Lett.*, 39(25), 1977.

[104] F.C. Schüller. *Plasma Phys. Contr. Fusion*, 37:A135–A162, 1995.

[105] P.C. de Vries, G. Pautasso, E. Nardon, et al. *Nucl. Fusion*, 56(026007), 2016.

[106] S.P. Gerhardt, D.S. Darrow, et al. *Nucl. Fusion*, 53(063021), 2013.

[107] V.A. Izzo. *Nucl. Fusion*, 46:541–547, 2006.

[108] A. Sykes and J.A. Wesson. *Phys. Rev. Lett.*, 44(18), 1980.

[109] H. Zohm, M. Maraschek, G. Pautasso, M. Schittenhelm, S. Sesnic, M. Sokoll, and W. Suttrop. *Plasma Phys. Contr. Fusion*, 37:A313–A324, 1995.

[110] V. Igochine, O. Dumbrajs, D. Constantinescu, H. Zohm, G. Zvejnieks, et al. *Nucl. Fusion*, 46:741–751, 2006.

[111] P.C. de Vries, G. Waidmann, A.J.H. Donné, and F.C. Schüller. *Plasma Phys. Contr. Fusion*, 38:467–476, 1996.

[112] R.J. Buttery, R.J. La Haye, et al. *Phys. Plasmas*, 15(056115), 2008.

[113] R. Fitzpatrick. *Phys. Plasmas*, 1(10):3308–3336, 1994.

[114] R. Fitzpatrick. *Phys. Plasmas*, 5(9), 1998.

[115] A. Bhattacharyya. *Indian J. Statistics*, 7(4), 1946.

[116] D. Comaniciu and V. Ramesh. *Comput. Vision Pattern Recog.*, 2:142–149, 2000.

[117] C.Z. Cheng, H.P. Furth, and A.H. Boozer. *Plasma Phys. Contr. Fusion*, 29(3):351–366, 1987.

[118] N.W. Eidietis et al. *Nucl. Fusion*, 55(063030), 2015.

[119] M.F. Turner and J.A. Wesson. *Nucl. Fusion*, 22(8):1069–1078, 1982.

[120] A. Bondeson. *Nucl. Fusion*, 26(7):929–940, 1986.

[121] R.B. White, D.A. Gates, and D.P. Brennan. *Phys. Plasmas*, 22(022514), 2015.

[122] M. Greenwald, J.L. Terry, and S.M. Wolfe. *Nucl. Fusion*, 28(12), 1988.

[123] D.A. Gates and L. Delgado-Aparicio. *Phys. Rev. Lett.*, 108(165004), 2012.

[124] P.H. Rebut and M. Hugon. *IAEA Proceedings*, pages 197–211, 1984.

[125] T.E. Evans, R.K.W. Roeder, J.A. Carter, B.I. Rapoport, M.E. Fenstermacher, and C.J. Lasnier. *J. Phys.*, Conference Series 7:174–190, 2005.

[126] T.E. Evans, R.A. Moyer, and P. Monat. *Phys. Plasmas*, 9(12), 2002.

[127] V.A. Izzo and I. Joseph. *Nucl. Fusion*, 48(115004), 2008.

[128] A.H. Glasser, C.R. Sovinec, et al. *Plasma Phys. Contr. Fusion*, 41:A747–A755, 1999.

[129] M.F.F. Nave and J.A. Wesson. *Nucl. Fusion*, 30(12):2575–2583, 1990.

[130] F.A. Volpe et al. *Phys. Rev. Lett.*, 115(175002), 2015.

[131] M. Okabayashi et al. *submitted to Nucl. Fusion*, 2016.

[132] A.W. Morris et al. *Phys. Fluids B*, 4(413), 1992.

[133] P.L. Taylor, A.G. Kellman, B.W. Rice, and D.A. Humphreys. *Phys. Rev. Lett.*, 76(6):916–919, 1996.

[134] M.J. Leyland et al. Effect of collisionality and effective charge on the h-mode pedestal structure in diii-d and jet. APS Division of Plasma Physics, 2014.

[135] A. Bondeson, R.D. Parker, M. Hugon, and P. Smeulders. *Nucl. Fusion*, 31(9):1695–1716, 1991.

[136] Equipe TFR. *Nucl. Fusion*, 17(6):1283–1296, 1977.

[137] A.W. Leonard, W.H. Meyer, B. Geer, D.M. Behne, and D.N. Hill. *Rev. Sci. Instrum.*, 66(2):1201–1204, 1995.

[138] B. Lipschultz, B. LaBombard, E.S. Marmar, M.M. Pickrell, J.L. Terry, R. Watterson, and S.M. Wolfe. *Nucl. Fusion*, 24(8):977–988, 1984.

[139] J.A. Wesson, D.J. Campbell, J.W. Connor, R.D. Gill, J. Hugill, C.N. Lashmore-Davies, G.M. McCracken, H.R. Wilson, et al. *Tokamaks*, page 320. Clarendon Press - Oxford, third edition, 2004.